Experimental Investigation of Influence of Crack Parallel Tension on Fracture Energy in Carbon Fiber Composites

Ashok Vemparala

A thesis

submitted in partial fulfillment of the

requirements for the degree of

Master of Science in Aeronautics & Astronautics

University of Washington

2025

Committee:

Marco Salviato

Ed Habtour

Program Authorized to Offer Degree:

Aeronautics & Astronautics

University of Washington

Abstract

Experimental Investigation of Influence of Crack Parallel Tension on Fracture Energy in Carbon Fiber Composites

Ashok Vemparala

Chair of the Supervisory Committee:

Marco Salviato

Department of Aeronautics & Astronautics

This work investigates the influence of crack-parallel tensile stress on the global Mode I interlaminar fracture behavior of carbon fiber polymeric matrix composites. Traditional Linear Elastic Fracture Mechanics (LEFM) assumes that stresses parallel to a crack have negligible impact on fracture toughness, an assumption challenged by recent studies such as the Gap Test. In quasibrittle materials like fiber-reinforced composites, the presence of crack-parallel stress can significantly modify crack propagation, fracture energy, and the associated fracture process zone (FPZ). The study's goal is to quantify these effects systematically through controlled experiments and to provide insights into fracture mechanics beyond conventional assumptions. By understanding how parallel stresses alter crack growth and energy dissipation, this work helps improve predictive models for composite structures, providing a valuable reference for academic research and practical applications. The findings aim to refine the characterization of composite fracture behavior, highlighting the need for methods that account for FPZ effects under complex stress states.

A novel experimental method, the Half-Open I test, was developed to investigate the effect of crack-parallel tension on Mode I fracture. Specimens consist of cross-ply IM7/977-3 carbon fiber laminates with a controlled initial crack introduced using a Teflon film. The key innovation involves inserting a GFRP tab into the crack seam, generating a bending moment at the crack front that induces tension along the crack propagation direction while simultaneously applying a crack-opening moment. By varying tab thickness, the magnitude of the induced bending moment and parallel tension is systematically controlled. Crack propagation is tracked using high-resolution imaging, with crack lengths measured at regular intervals. The negative geometry of the design promotes stable crack growth, providing an advantage over traditional DCB tests. However, the only limitation is the inapplicability of Bazant's size effect law, preventing direct estimation of fracture energy and FPZ size.

The experiments reveal that increasing the thickness of the inserted tab, and consequently the crack-parallel tension, enhances the fracture resistance of the composite. Measured crack propagation lengths are converted into energy release rates using Abaqus finite element simulations, and R-curves are reconstructed for each tab thickness and laminate. Despite data noise, trends indicate an rightward shift in fracture energy with increasing parallel stress, suggesting that low-to-moderate crack-parallel tension strengthens the laminate through mechanisms such as fiber bridging and extended FPZ development. Thicker tabs produce more stable crack propagation, while thinner tabs exhibit initial instability. These findings demonstrate that Mode I fracture energy in composites is not a fixed material property but is influenced by the local stress state, challenging traditional LEFM assumptions. Overall, the study provides a robust methodology for assessing crack-parallel effects and highlights the importance of incorporating FPZ considerations in modeling and designing composite structures.

Table of Contents

List of Figures

List of Tables

Glossary

CFRP Carbon Fiber Reinforced Polymer

GFRP Glass Fiber Reinforced Plastic

4PB 4 Point Bend

ASTM American Society for Testing and Materials

SIF Stress Intensity Factor

ERR Energy Release Rate

FEA Finite Element Analysis

FPZ Fracture Process Zone

LEFM Linear Elastic Fracture Mechanics

QBFM Quasi-Brittle Fracture Mechanics

SEL Size Effect Law

DCB Double Cantilever Beam

U.S. United States

Acknowledgements

Accomplishments like completing a graduate degree such as Masters, are rarely accomplished alone. They are made possible through the unwavering support of family, friends, and mentors. My own journey has been no exception, and I am deeply grateful to the many individuals who have guided, encouraged, and supported me throughout my time in graduate school.

Foremost, I extend my sincere gratitude to my advisor and committee chair, Professor Marco Salviato. His guidance and encouragement have been invaluable, consistently challenging me to meet high standards while also fostering my growth as both a researcher and an engineer. Entering graduate school, I sought to explore my capabilities in a new field of aerospace research, and under his mentorship, I came to realize that the only real limitations are the ones we impose on ourselves. His expertise in composites and fracture mechanics, paired with his patient and generous mentorship, both academically and personally, made every discussion a learning opportunity. For these reasons, I consider myself fortunate to have had him as an advisor and role model.

I am also deeply grateful to Professor Ed Habtour, who served as my second committee member. His expertise in composite materials, shared through both coursework and engaging discussions, greatly enriched my understanding of the field. In particular, his instruction on classical laminate theory not only strengthened my grasp of laminate behavior but also enhanced the quality of my modeling work in Abaqus as well as my approach to experimental specimen preparation. His guidance and support throughout my graduate studies were instrumental in helping me reach this milestone, and I am sincerely thankful for his mentorship.

I would also like to extend my gratitude to my fellow MAMs lab members, whose willingness to help and share knowledge made my graduate experience far more rewarding. In particular, I am especially thankful to Genki Matsubara, whose patience, support, and guidance were invaluable throughout this work. His assistance in both theoretical discussions and experimental efforts provided me with clarity and direction at many critical stages of my research.

Finally, I am deeply grateful to my father for his unwavering support and encouragement throughout my life, and especially for his steadfast presence during the past two years of my graduate studies.

Dedication

This work is dedicated to my late mother, Lakshmi Vemparala. You are missed dearly.

Chapter – 1 Introduction

1.1. Composite Materials

A composite material is made by combining two or more distinct materials in such a way that the resulting material has properties superior to those of the individual components. These constituents typically include reinforcement, such as fibers or particles, which provide strength and stiffness and a matrix, which is a binding material that holds the reinforcement in place and helps transfer loads between them. The components retain their individual physical and chemical identities but work together to create a material with enhanced mechanical, thermal, or chemical performance. Common examples include fiberglass, where glass fibers are embedded in a polymer matrix, and carbon fiber composites, used in aerospace and sports equipment for their high strength-to-weight ratio. In everyday life, composites can be seen in concrete, a combination of cement with sand and gravel, plywood, which is made of layers of wood veneer, and reinforced tires, that is, rubber with steel wires, all designed to perform better than their base materials alone [1].

In this paper, the term composite specifically refers to carbon fiber reinforced polymer composites, where it is important to note that the results and conclusions presented herein are based solely on the behavior of unidirectional CFRP materials. As such, any direct extension of these findings to other classes of composites such as metal matrix composites or ceramic matrix composites would be inappropriate due to fundamental differences in constituent materials, bonding mechanisms, failure modes, and fracture behavior. Throughout this paper, the term *"composite"* may occasionally be used as a stand-alone reference. In all such cases, it should be understood to exclusively denote unidirectional carbon fiber reinforced polymer composites, unless explicitly stated otherwise.

1.2. Carbon Fiber Composites and Applications

In recent years, the use of composite materials, particularly carbon fiber composites has grown rapidly across various industries due to their exceptional mechanical properties. These materials offer a high strength-to-weight ratio, fatigue resistance, and corrosion resistance, making them ideal for structural applications. As a result, they are now widely used in aerospace, automotive, energy, recreational, and civil engineering sectors[2], [3], [4], [5], often replacing traditional metals

like aluminum and titanium. The aerospace industry, in particular, has seen significant advances in material selection, with carbon fiber composites becoming a critical part of modern aircraft structures [6].

Carbon Fiber Reinforced Polymer is a composite made of carbon fibers embedded in a polymer matrix. The carbon fibers act as the primary load-bearing component, while the polymer binds the fibers and facilitates load transfer. To optimize stiffness and strength, fibers are typically aligned in specific directions, giving CFRP its anisotropic mechanical behavior. Its key advantages are its high specific modulus and strength, far exceeding those of conventional metals. Due to these benefits, CFRP is now heavily used in aerospace. For example, as shown in Fig 1.1, both the Boeing 787 and Airbus A350 are made of approximately 50% composites by weight and about 80% by volume [7], much higher than previous generations of aircraft.

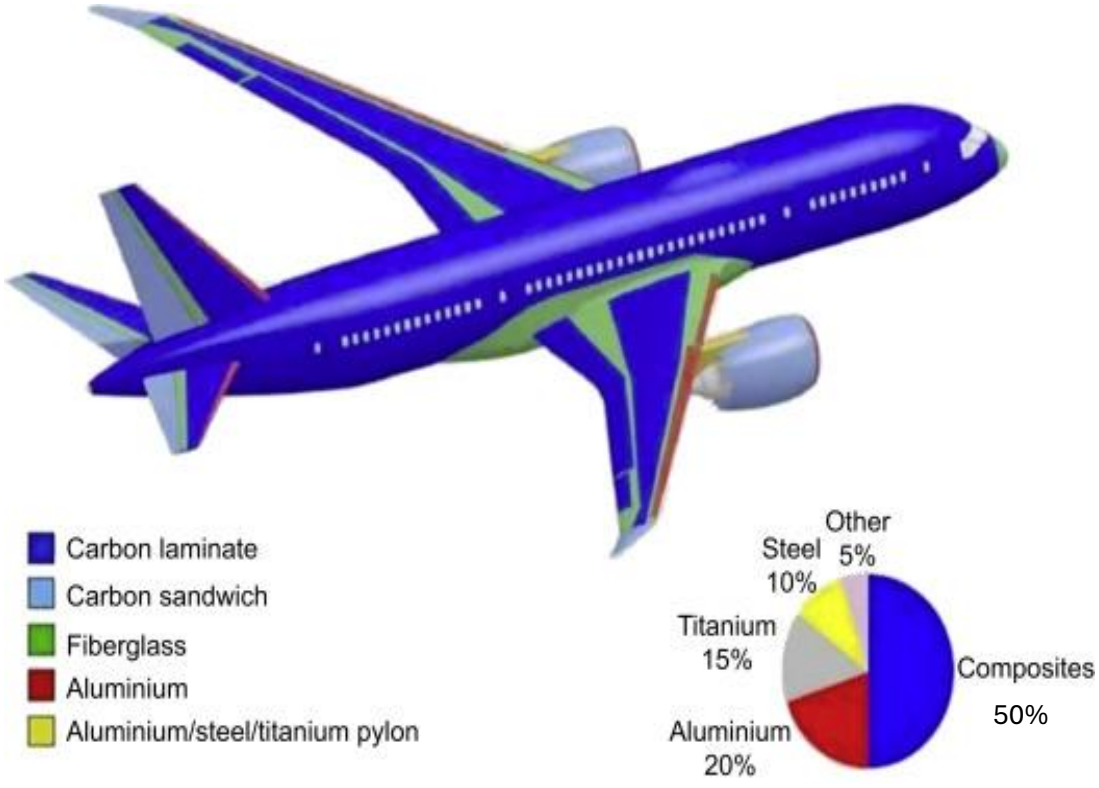

Figure 1.1 Materials used in a Boeing Dreamliner 787 [7].

This upward trend in composite usage is expected to continue across adjacent sectors such as automotive, energy, and infrastructure, with potential for entirely new applications yet to be

discovered. The present study contributes toward a deeper understanding of composite behavior, particularly CFRPs, enabling engineers to harness these materials more effectively in addressing future technological and societal needs.

1.3. Supporting Theory

Fracture has been a persistent challenge for society since the advent of man-made structures, and it has been a subject of engineering study for over a century. One of the earliest and most influential contributions came from Alan Griffith in 1921, whose Griffith energy balance established a quantitative relationship between fracture stress and flaw size, a concept still fundamental in fracture mechanics today, including in this study [8]. Unfortunately, many advances in the field have been driven by lessons learned from catastrophic failures, such as airline crashes [9], civil infrastructure collapses, and pressure vessel explosions [10]. Fracture mechanics became a mainstream engineering discipline largely due to the failures of the Liberty ships during World War II, where at least 400 ships suffered significant fractures, with some breaking completely in two. The economic impact of fracture is equally striking, a 1978 study estimated the annual cost in the U.S. at $119 billion and projected that $63 billion could be saved annually through existing fracture-resistant technologies and continued research [11], [12]. This underscores the enduring importance of fracture mechanics in ensuring safety, reliability, and economic efficiency in engineering design and materials development.

1.3.1. Linear Elastic Fracture Mechanics

The Liberty ship failures marked a pivotal moment that spurred intensive research into fracture mechanics, ultimately leading to the development of Linear Elastic Fracture Mechanics (LEFM). LEFM was formulated to describe fracture behavior in materials that act in an ideally brittle manner. A key assumption is that any plastic deformation or damage at the crack tip is negligible compared to the overall structure size, and that the structural response remains linear elastic, following Hooke's law [13]. Building on these principles, Westergaard developed an analytical solution to describe the stress field near a crack tip. For Mode I loading, the y-direction stress σ_{yy} under a far-field stress σ_{∞} is given by [14]:

$$\sigma_{yy} = \frac{\sigma_\infty \sqrt{\pi a}}{\sqrt{2\pi r}} \left[cos\frac{\theta}{2}(1 + sin\frac{\theta}{2} sin\frac{3\theta}{2})\right] \quad (1.1)$$

where r and θ are polar coordinates from the crack tip. This equation predicts that as r approaches zero, the stress tends toward infinity. To overcome the issue of infinite stress at the crack tip, a parameter called the Stress Intensity Factor (SIF) was developed to characterize the near-tip stress field. For Mode I loading, the SIF is defined as:

$$K_{Ic} = \lim_{r\to\infty} \sigma_{yy}\sqrt{2\pi r} = Y\sigma_\infty\sqrt{\pi a} \quad (1.2)$$

where Y is the geometric correction factor. LEFM uses a single-parameter fracture description, most commonly the critical stress intensity factor (K_c) or the critical fracture energy (G_c), both treated as constant material properties. These are specific to the fracture mode (see Section 1.4.) and denoted as K_{Ic}, K_{IIc}, K_{IIIc} or G_{Ic}, G_{IIc}, G_{IIIc}. A major limitation of LEFM is its prediction of stress singularity, which applies only to ideally brittle materials. In ductile materials, yielding occurs near the crack tip, forming a Plastic Zone (PZ) where stress is limited to the yield strength σ_{yy}. In quasibrittle materials, the stress decreases near the tip due to the Fracture Process Zone (see Section 1.3.2.), a finite region of microcracking and damage.

1.3.2. Quasibrittle Fracture Mechanics

The assumptions underlying LEFM are often too restrictive for many modern engineering materials, particularly when the material does not behave in an ideally brittle manner. This limitation was first recognized in materials such as concrete, and later in fiber composites, rocks, ceramics, wood, and others that display quasi-brittle behavior. Quasi-brittle materials occupy an intermediate category between brittle and ductile materials. Because LEFM's assumption of negligible damage and a singular stress field does not hold for such materials, a more suitable framework, Quasi-Brittle Fracture Mechanics (QBFM) was developed which accounts for the finite size of the FPZ and non-linear fracture behavior. This work focuses on QBFM, as its assumptions align most appropriately with the fracture characteristics of carbon fiber reinforced composites [15], [16], [17], [18], [19], [20], [21], [22], [23].

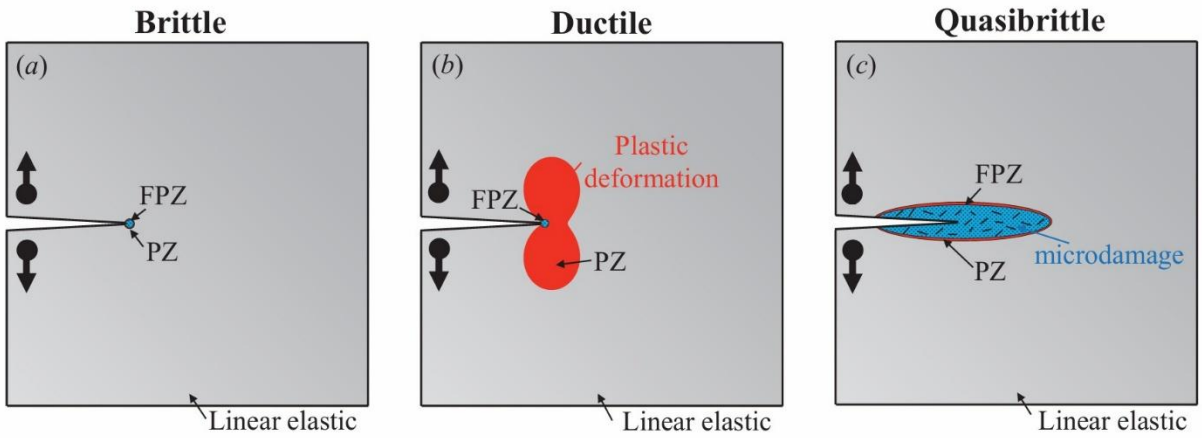

Figure 1.2 Fracture behavior in (a) Brittle, (b) Ductile and (c) Quasi-brittle material [23].

Quasi-brittle materials do not fail instantly upon crack initiation. Instead, a region of progressive damage develops near the crack tip, characterized by microcracks, frictional micro-slips, and grain interlocking, which collectively soften the material in that zone. This extended, non-linear damage region is known as the finite Fracture Process Zone (FPZ), as shown in Figure 1.2. Unlike the PZ in ductile materials whose size depends on the applied loading, the FPZ size is an intrinsic material property.

To characterize the influence of the FPZ on quasi-brittle materials of varying sizes, the size effect is a critical concept. Size effect refers to the dependence of a material's structural strength on the overall structure size, a clear departure from classical predictions, such as plastic-limit analysis or strength-of-materials theory, which assume no size dependence. At very small scales, quasi-brittle materials exhibit pseudo-plastic behavior; at intermediate scales, they display true quasi-brittleness; and at large scales, their behavior approaches ideal brittleness. Traditional LEFM does not incorporate the effects of the FPZ or capture the transitional fracture behavior of quasi-brittle materials.

To describe the size effect in quasi-brittle materials, Bažant's Type II Size Effect Law (SEL) is commonly used. It quantifies how nominal strength decreases with increasing structural size due to the influence of the Fracture Process Zone. The SEL [15] is expressed as:

$$\sigma_N = \frac{Bf'_t}{\sqrt{1+\frac{D}{D_0}}} \tag{1.3}$$

Where, σ_N is the nominal strength, D is the characteristic structure size, D_0 is the reference size marking the transition from quasi-brittle to brittle behavior, f_t' is the material's tensile strength, and B is a dimensionless parameter. By applying Irwin's relation between fracture energy and stress intensity factor, and using a first-order Taylor expansion, Bažant's SEL can also be reformulated in terms of more familiar fracture mechanics parameters:

$$\sigma_N = \sqrt{\frac{EG_f}{D\, g(\alpha_0) + c_f\, g'(\alpha_0)}} \tag{1.4}$$

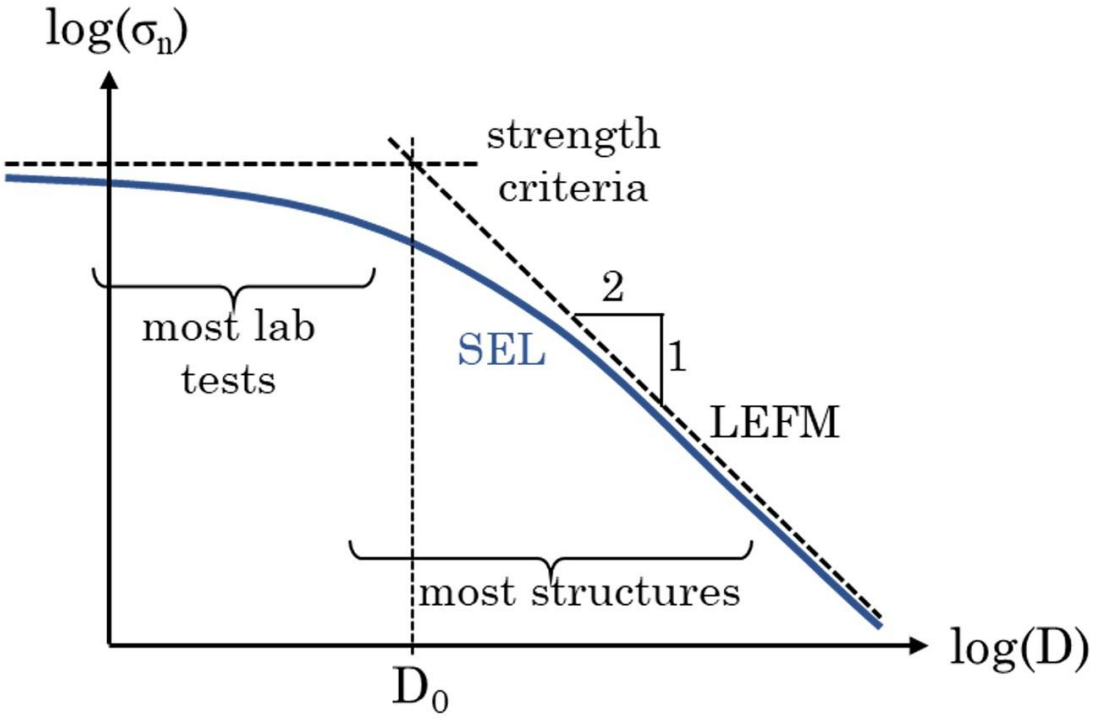

Figure 1.3 Log-Log plot of Bažant's Type II Size Effect Law and comparison with LEFM and strength of materials criteria [24].

Where, E is the modulus of elasticity, G_f is the fracture energy, c_f is a measure of the fracture process zone, $g(\alpha_0)$ is the dimensionless energy release rate evaluated at α_0, $g'(\alpha_0)$ is the derivative of g with respect to α evaluated at α_0, and α is the crack length normalized by D. Figure 1.3 shows

the size effect predictions of LEFM and strength criteria analysis superimposed, it can be observed that LEFM predicts a constant negative size effect with a slope of -1/2 while strength of materials analysis is a constant, both of which are inadequate to describe quasi-brittle materials at varying size scales [24].

1.3.3. Modes of Fracture

Fracture can occur in three distinct modes, either individually or in combination, depending on the stress state at the crack tip. These fracture modes represent the decomposition of crack-tip stresses into separate components. Mode I (opening mode) occurs when tensile stress acts normal to the crack plane, causing the crack faces to open. Mode II (sliding or in-plane shear mode) arises from shear stress acting parallel to the crack plane and in the direction of crack propagation, causing the crack faces to slide relative to each other. Mode III (tearing or out-of-plane shear mode) results from shear stress acting parallel to the crack front but perpendicular to the crack plane, producing tearing deformation along the crack front, as shown in Figure 1.4 [25].

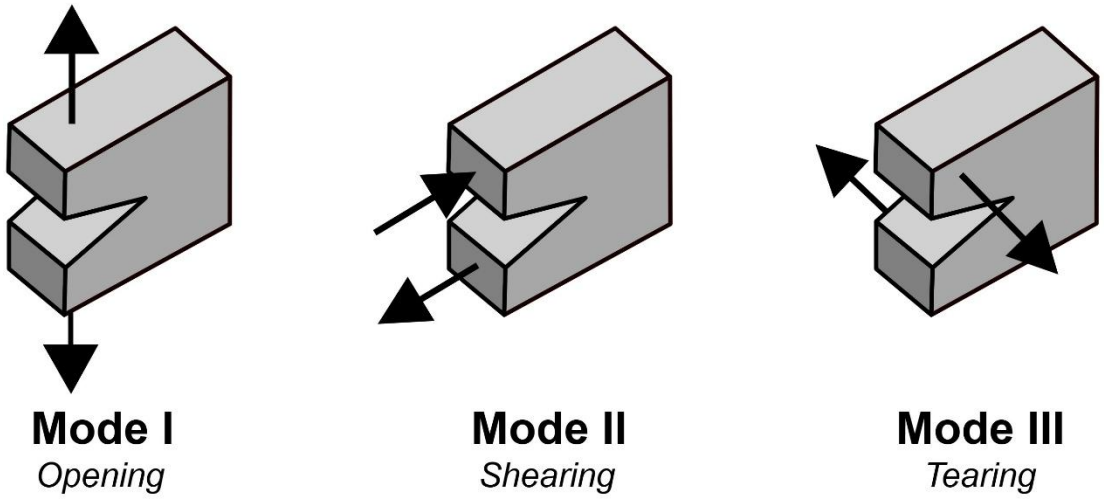

Figure 1.4 The three modes of Fracture [25].

These three fracture modes influence the stress distribution around a crack differently, and a material's resistance to each mode of crack propagation can vary significantly. In real-world engineering applications, Mode I loading is the most common, as tensile stresses normal to the crack plane are often the primary cause of crack growth. Consequently, most fracture mechanics

research has focused on understanding and characterizing Mode I behavior in engineering materials. In contrast, Modes II and III, in-plane and out-of-plane shear, are less frequently studied and remain less understood. This work concentrates primarily on investigating Mode I fracture, with minimal consideration given to Modes II or III.

1.3.4. Energy Release Rate and J-Integral

The propagation of a crack can be understood from an energy balance perspective. For a crack to grow, the energy available defined as the difference between the external work done on the material and the strain energy stored within it must equal the energy required to create new crack surfaces. In fracture mechanics, this available energy is quantified as the energy release rate (ERR) G^*, which represents the energy available per unit area of crack growth.

Mathematically,

$$G^* = \frac{\delta W - \delta U}{b\delta a} \tag{1.5}$$

Where b is the material thickness, a is the crack length, W is the external work, and U is the stored strain energy. Crack propagation occurs when G^* reaches the critical fracture energy G_c, a material-specific property representing the resistance to crack growth. G_c is a key objective of this study, as it governs the fracture behavior and structural integrity of the material under investigation.

There are several methods to evaluate the energy release rate G^*, with the J-integral being one of the most widely used and the method applied in this study. Developed by Jim Rice in 1968, the J-integral provides a robust failure criterion applicable to brittle, quasi-brittle, and ductile materials, even when significant plastic energy dissipation occurs near the crack tip [26]. The J-integral is a path-independent line integral that quantifies the energy flow into the crack tip region, effectively capturing the complex stress and strain fields. It is particularly convenient for numerical evaluation when the detailed stress and strain distributions around the crack tip can be determined, which is commonly achieved through finite element analysis (FEA). This makes the J-integral a powerful tool for fracture analysis across a wide range of materials and loading conditions.

Mathematically,

$$J = \int_{\Gamma} \left(\overline{u} dx_2 - \vec{t} \cdot \frac{\partial \vec{u}}{dx_1} ds\right) \tag{1.6}$$

where Γ is an arbitrary counterclockwise path around the crack, $\overline{u}$ is the strain energy density, $\vec{t}$ is the 2D traction vector, and $\vec{u}$ is the 2D displacement vector.

1.3.5. **R-Curves and Fracture Stability**

In quasi-brittle materials, when the FPZ is large relative to the structure size, the material exhibits pronounced non-linear behavior. However, if the FPZ is negligible, the structure's response can be approximated as linear using a far-field equivalence approach. In this method, an equivalent elastic crack is introduced, with its tip positioned within the FPZ, such that the far-field stress, displacement, and strain match those of the actual case. A powerful generalization of this concept is the resistance curve or R-curve, which fully describes the crack growth process. The R-curve characterizes how the material's resistance to crack extension increases with crack growth, capturing the transition from initiation to stable growth and, ultimately, to fracture.

The R-curve concept retains the basic framework of LEFM but replaces the constant fracture criterion $G = G_f$ with a variable resistance criterion $G = R$, where R represents the material's crack growth resistance. Unlike G_f, R is not constant but generally increases with the equivalent crack extension Δae. This approach captures the rising resistance typical of quasi-brittle materials due to mechanisms like microcracking and bridging. R-curves are particularly effective for structures containing a single crack, but they are not well-suited for analyzing structures with interacting cracks, where resistance effects become more complex.

The shape of the R-curve is strongly influenced by the geometry of the specimen or structure. Factors such as crack-front shape, loading configuration, and boundary conditions can alter the measured resistance curve. Because of this sensitivity, the R-curve can be considered unique only within a narrow range of specimen geometries and sizes where these influencing factors remain consistent. Outside this range, variations in geometry or size may change the slope, shape, or plateau of the R-curve, making direct comparisons between different structures or tests unreliable without careful normalization.

The plots illustrated in Figure 1.5 are typical shapes of R-curves and in In Figure 1.5a, the crack

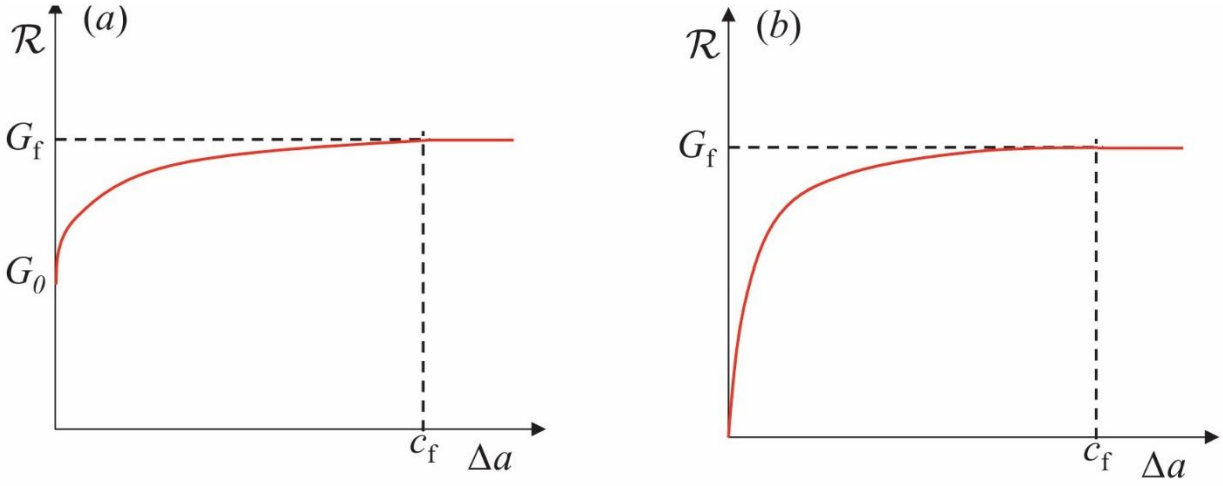

Figure 1.5 R-curves (a) with threshold, (b) without threshold [23].

driving force $\boldsymbol{\mathcal{G}}$ must reach a threshold value G_0 before crack growth begins, indicating an initiation threshold. In contrast, in Figure 1.5b, the crack starts to grow immediately, with no apparent threshold. In both scenarios, the fracture resistance increases with crack extension until it reaches a plateau. This plateau occurs when the FPZ is fully developed and propagates in a self-similar manner. If $\boldsymbol{c_f}$ is the crack extension at plateau and $\boldsymbol{G_f}$ is the plateau resistance, then

Mathematically,

$$\mathcal{R} = G_f\left(\frac{\Delta a}{c_f}\right) \tag{1.7}$$

Where $\boldsymbol{c_f}$ and $\boldsymbol{G_f}$ are material properties and ($\Delta a/\boldsymbol{c_f}$) is a dimensionless function.

Based on the behavior of the crack driving force $\boldsymbol{\mathcal{G}}$, geometric models can be categorized into two types: positive geometry and negative geometry. In positive geometry, $\boldsymbol{\mathcal{G}}$ increases with crack length a at constant load. This is the most common case in many standardized fracture tests, where crack growth becomes unstable once a critical length is reached. In contrast, negative geometry exhibits the opposite trend $\boldsymbol{\mathcal{G}}$ decreases with a under constant load, requiring progressively higher loads to sustain crack growth. In a special limiting case of negative geometry, such as an unbounded specimen, the required load for propagation increases indefinitely. In real

panels of finite width, geometry is often negative when the crack is small but transitions to positive as the crack tip approaches the boundaries, due to increasing stress concentration and reduced remaining ligament.

Positive geometries typically exhibit a peak load during testing, occurring when the R-curve and the energy release rate curve become tangential with equal slope, as shown in Figure 1.6a [15], [23]. At this point, both the fracture energy G_f, and the fracture process zone length can be determined using size-effect laws, such as Bažant's Type II Size Effect Law (SEL), that is using equations (1.3) and (1.4). In practical structures, once crack growth passes this critical point, failure becomes unstable under load-controlled conditions, leading to catastrophic fracture. This peak load thus defines the effective structural strength.

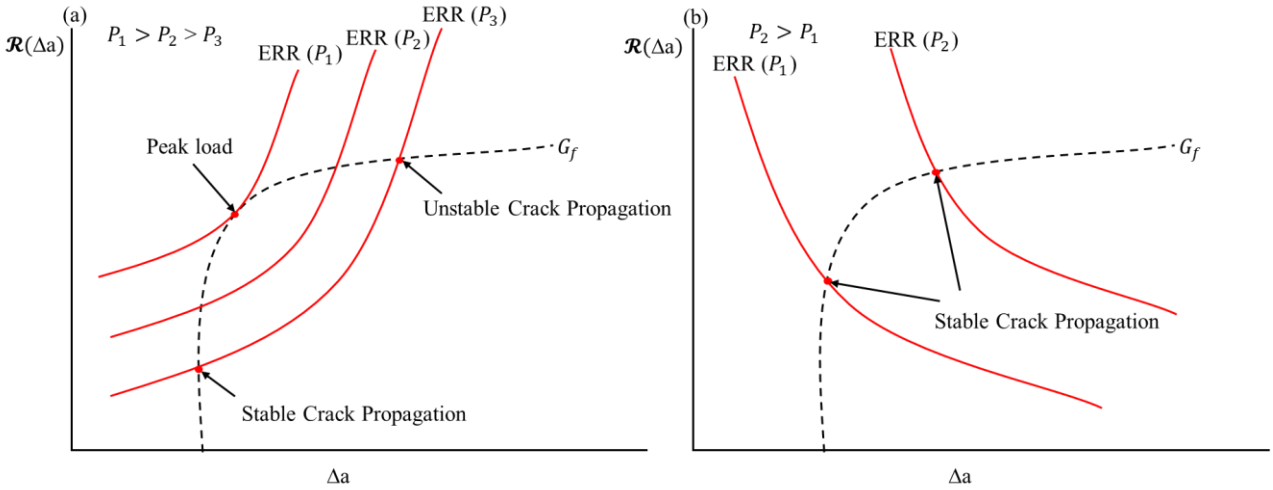

Figure 1.6 R-curves of (a) Positive, (b) Negative Geometry with ERR curves.

In contrast, negative geometries show a decrease in ERR with crack extension, so fracture resistance increases relative to the available driving force. Consequently, there is no well-defined upper bound on fracture strength from a fracture mechanics standpoint, that is, the ERR curve does not tangentially intersect the R-curve, as shown in Figure 1.6b. Such cases require steadily increasing load for crack propagation, and in certain limiting cases, such as previously mentioned unbounded specimen cases, propagation may require ever-increasing load.

This work will primarily focus on negative geometries, as the development of the specimen geometry aims to fulfill the criterion of generating tensile stresses along the crack direction during crack propagation. Achieving this condition inherently results in a negative geometry configuration. To address the fracture behavior of the composite under crack-parallel tension, R-curves will serve as a primary analytical tool. One of the key challenges with negative geometries is the absence of a distinct peak load, which makes it impossible to directly apply SEL for estimating the FPZ size and G_f.

To investigate the influence of constant crack-parallel tension along the crack direction, R-curves will be constructed for different levels of constant crack parallel tension. These curves will be derived from experimental test data, enabling the assessment of how sustained parallel tensile stresses influence crack growth resistance. This approach allows for a systematic evaluation of fracture behavior in conditions where conventional peak-load-based methods are inapplicable. The resulting analysis will provide insights into fracture mechanisms under negative geometry loading and support the development of more accurate characterization methods for materials subjected to crack-parallel tension.

1.4. Thesis Motivation and Objectives

Modern fracture mechanics has long been grounded in the traditional assumption that a material possesses a constant critical fracture energy, G_c, a fixed value representing its inherent resistance to crack growth. This simplification, often termed the single-parameter approach, lays the foundation for LEFM. Engineers calculate the energy release rate (G^*) for a component using analytical formulas or numerical simulations and compare it directly to the known G_c of the material. If the calculated value exceeds the material's threshold, crack propagation is expected; if it remains below, the crack is predicted to remain dormant [13].

One reason this constant-value assumption holds within LEFM is the idealization of cracks as mathematical lines with zero tip radius, neglecting significant near-tip plastic deformation or damage processes. Within this line-crack model, fracture occurs solely via the three classical modes, shown in Figure 1.4. For instance, in a planar biaxial stress state where one stress component acts normal to the crack plane and another acts parallel and in the direction of

propagation, the parallel component does not contribute to crack opening. In effect, the biaxial condition reduces to a uniaxial fracture problem, as shown in Figure 1.7.

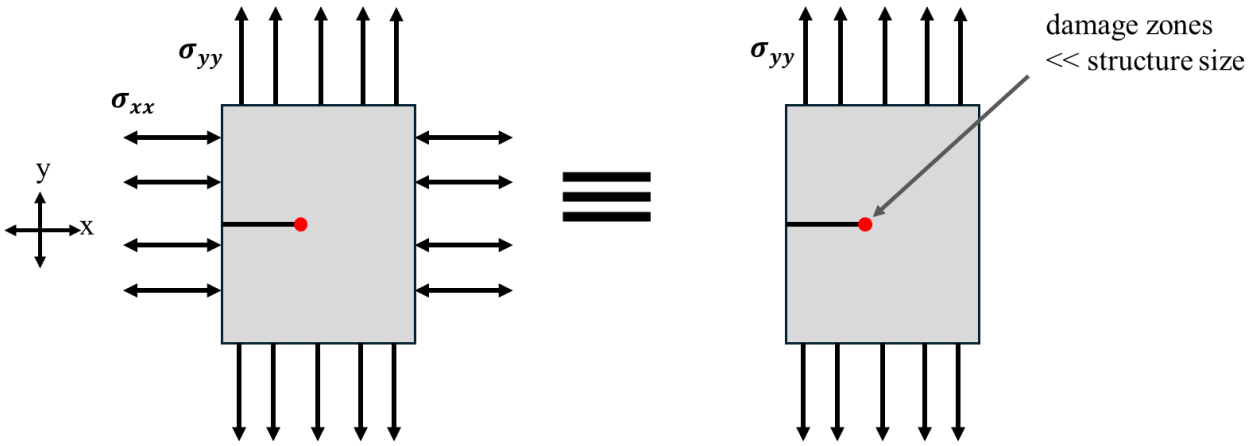

Figure 1.7 Equivalence of a biaxial and uniaxial stress, based on the assumption of LEFM.

Consequently, when nonlinear near-tip phenomena are excluded, the material's apparent fracture resistance remains invariant to such loading variation, like the parallel stress, σ_{xx}. This reinforces the perspective within LEFM that G_c is a material property, constant under different stress states as long as the model's core assumptions hold.

In quasi-brittle materials, the FPZ often has a finite width that is significant relative to the structure size, making the classical line-crack assumption of LEFM invalid. When the FPZ extends appreciably in the crack-parallel (x) direction, the stress component, σ_{xx}, parallel to the crack propagation direction can directly affect the crack opening behavior. Consequently, the local stress state deviates from a simple uniaxial condition, indicating that crack growth may occur through mechanisms that do not confine to the classical fracture modes and the material's G_c changes due to influence of σ_{xx}, as shown in Figure 1.8. This phenomenon was investigated using the Gap test on composites, which demonstrated that crack-parallel compression can reduce fracture energy, confirming that LEFM's constant fracture energy assumption does not hold under such conditions [27].

Building on the current research and the motivation to investigate fracture behavior under crack-parallel tension, a comprehensive experimental program was undertaken. Chapter 2 details

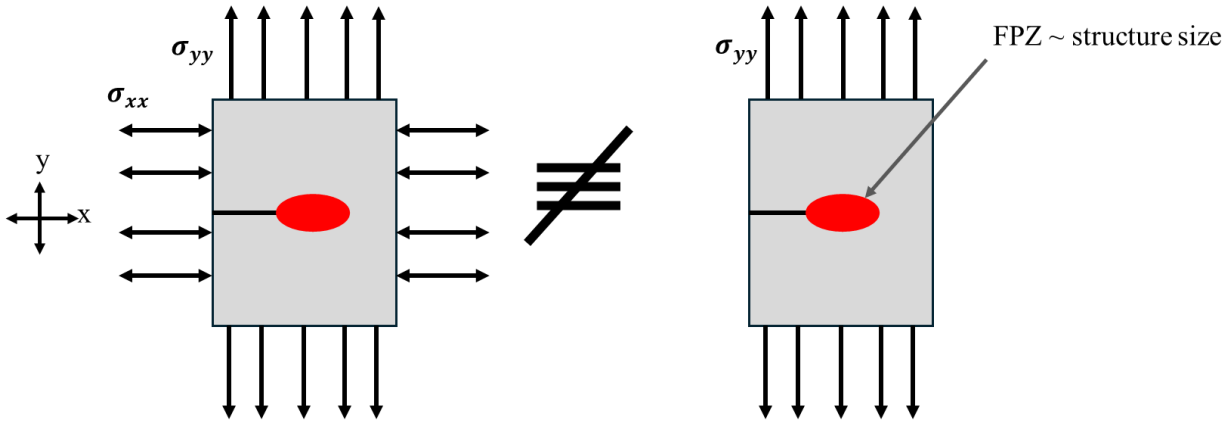

Figure 1.8 Effect of finite FPZ size invalidates the LEFM assumption.

the novel specimen geometry and its design for composite materials. Since this experiment is new for composites and not covered by existing ASTM standards, three iterations of design modifications were carried out to achieve a configuration that meets the requirements and yields reliable data. The full design iteration process and lessons learned are presented. Chapter 3 describes the manufacturing techniques used to produce the test coupons. Chapter 4 evaluates the efficacy of the proposed test method, presenting and analyzing the experimental data using R-curves. The observations from these experiments are further interpreted through J-Integral evaluations at multiple crack propagation points using Abaqus FEA. Finally, Chapter 5 summarizes the key conclusions of the study and discusses their implications for composite structures in industry.

1.5. Literature Review

1.5.1. Effects of Crack Parallel Compression in Concrete

Researchers at Northwestern University explored a stress state in which a crack parallel to compression is subjected to a bending moment whose normal stresses open the crack via Mode I fracture. This was achieved through a simple modification of the standard three-point bending

(3PB) test. A polymer pad with a perfectly plastic yield plateau was placed beneath the specimen to generate crack-parallel compression, as shown in Figure 1.9. The pads were designed to yield fully before rigid rollers engaged to induce the bending moment. This ensured a controlled transition from compression to bending. The team termed this setup "The Gap Test," referring to the gap introduced between the specimen and rollers, enabling them to draw novel and impactful conclusions from a well-established test method [28].

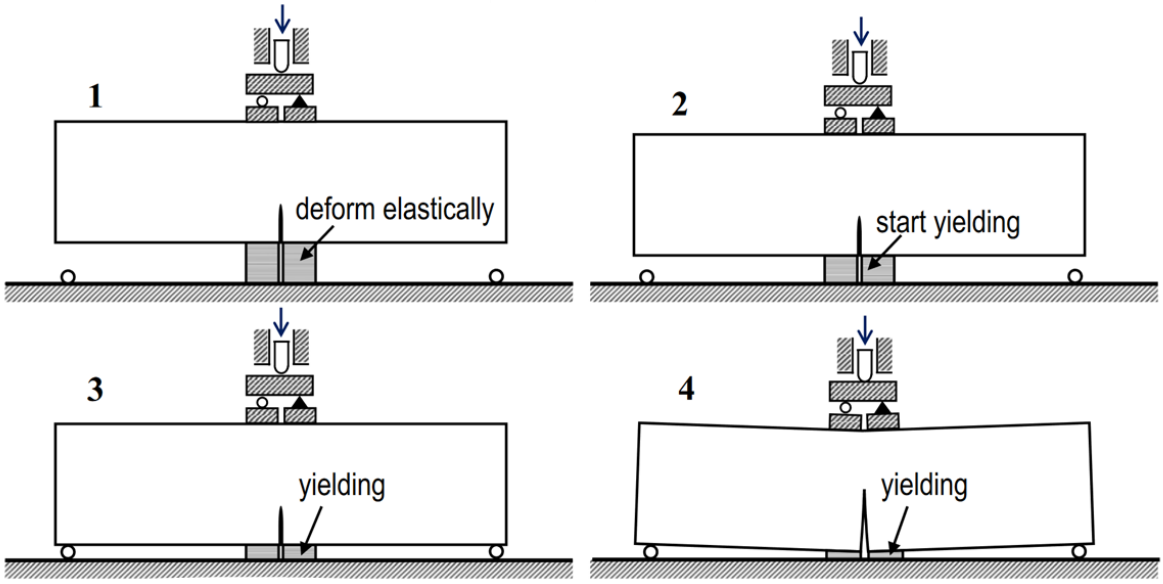

Figure 1.9 Schematic of Gap test on concrete [28].

Northwestern's results indicate that concrete's fracture energy is not constant under crack-parallel compression. Depending on the compression level, fracture energy may rise to about 1.8 times the nominal Mode I value or drop near zero as compression approaches the material's compressive strength. A similar pattern is seen for the c_x value, representing FPZ size. The results are shown graphically in Figure 1.10. In the initial rising phase of Figure 1.10, crack-parallel stress increases resistance to slip along inclined microcracks and enhances grain interlock from surface roughness, producing a strengthening effect. In the later decreasing phase, high crack-parallel

stresses surpass the friction and slip resistance, leading instead to lateral expansion and axial splitting of microcracks. These microstructural mechanisms explain the observed variation in fracture energy [28].

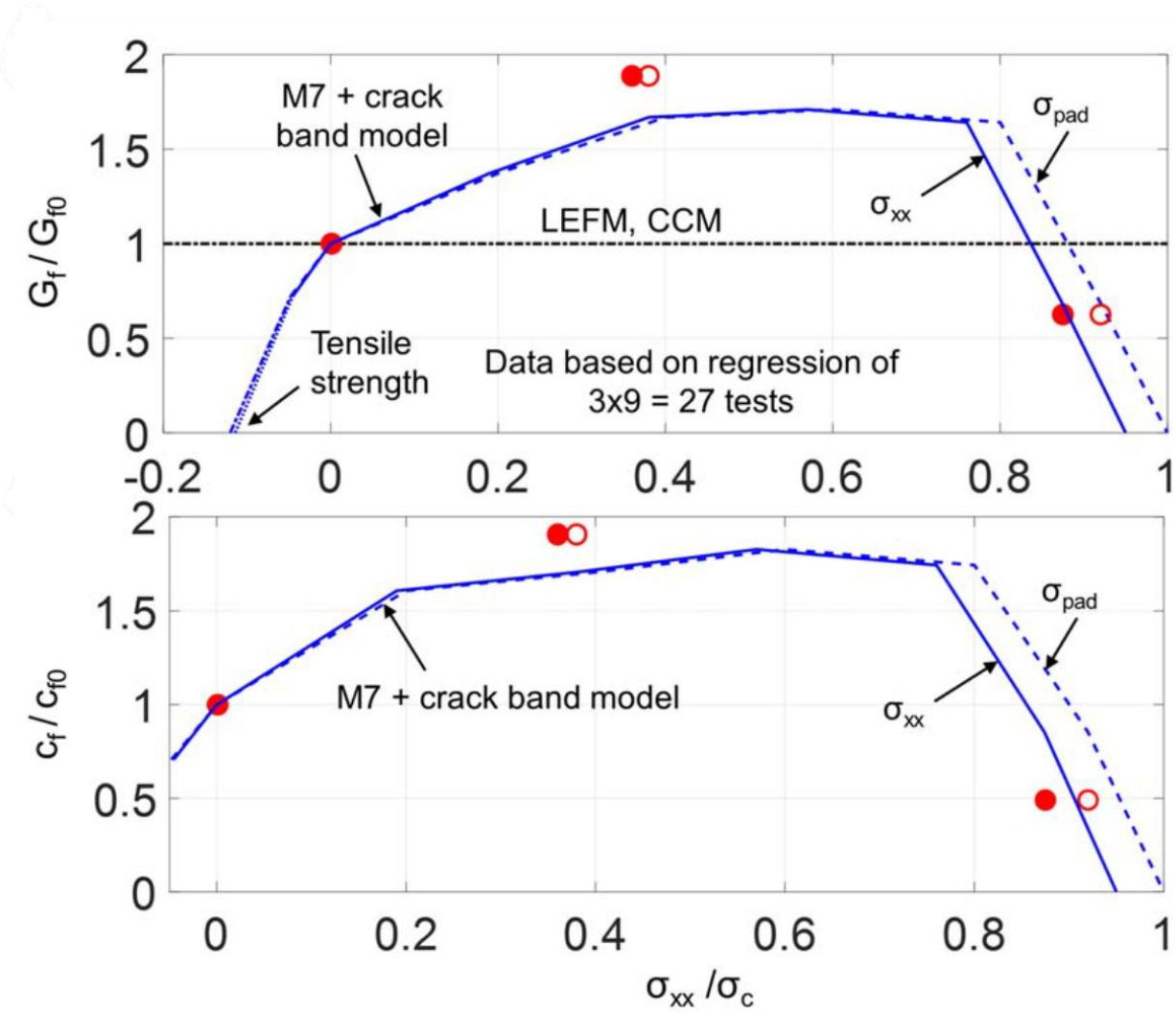

Figure 1.10 Gap Test results from concrete specimens [28]. The red dots indicate experimental data whereas the blue curves are FEA results. G_f denotes fracture energy, G_{fo} is the fracture energy with no crack parallel compression, c_f a measure of the FPZ size, c_{fo} is the FPZ with no crack parallel compression, σ_{xx} is the crack parallel stress level, and σ_c is the compressive strength of the material.

1.5.2. Effect of Crack Parallel Compression in Carbon fiber Composites

Building upon the work at Northwestern University, researchers at the University of Washington investigated the same stress state, where a crack parallel to compression is subjected to a bending moment that opens the crack via Mode I fracture, but in carbon fiber composites, specifically Toray T800H/3900-2. The experimental setup was adapted to accommodate the reduced thickness of the composite specimens while preserving the essential loading conditions of the original configuration, as shown in Figure 1.11. In recognition of the original work by the Northwestern team, the modified method was termed the "Gap Test." This adaptation enabled researchers to examine how fiber-reinforced composites respond under combined crack-parallel compression and crack-opening due to bending, extending the applicability of the earlier findings from concrete to high-performance composite materials [27].

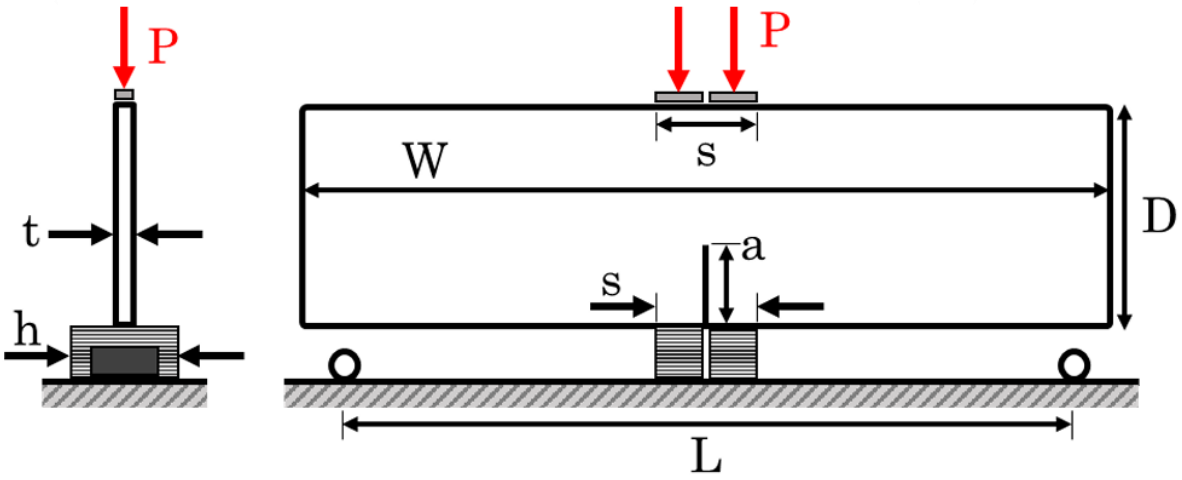

Figure 1.11 Schematic of Gap test on carbon fiber composites [27].

The results, analyzed using the linear regression of SEL equation (1.3), shown in Figure 1.12 that as the crack-parallel compression ratio ξ, relative to ultimate tensile strength, increases, the slope of the regression also increases, indicating a reduction in fracture energy. Additionally, the intercepts for ξ = 0.29 and 0.44 are higher than for ξ = 0, reflecting an increase in the fracture process zone (FPZ) size, represented by the cf value, due to crack-parallel stress. These trends

suggest evolving damage mechanisms at the crack tip and confirm that crack-parallel compression weakens the composite by reducing fracture energy and enlarging the FPZ.

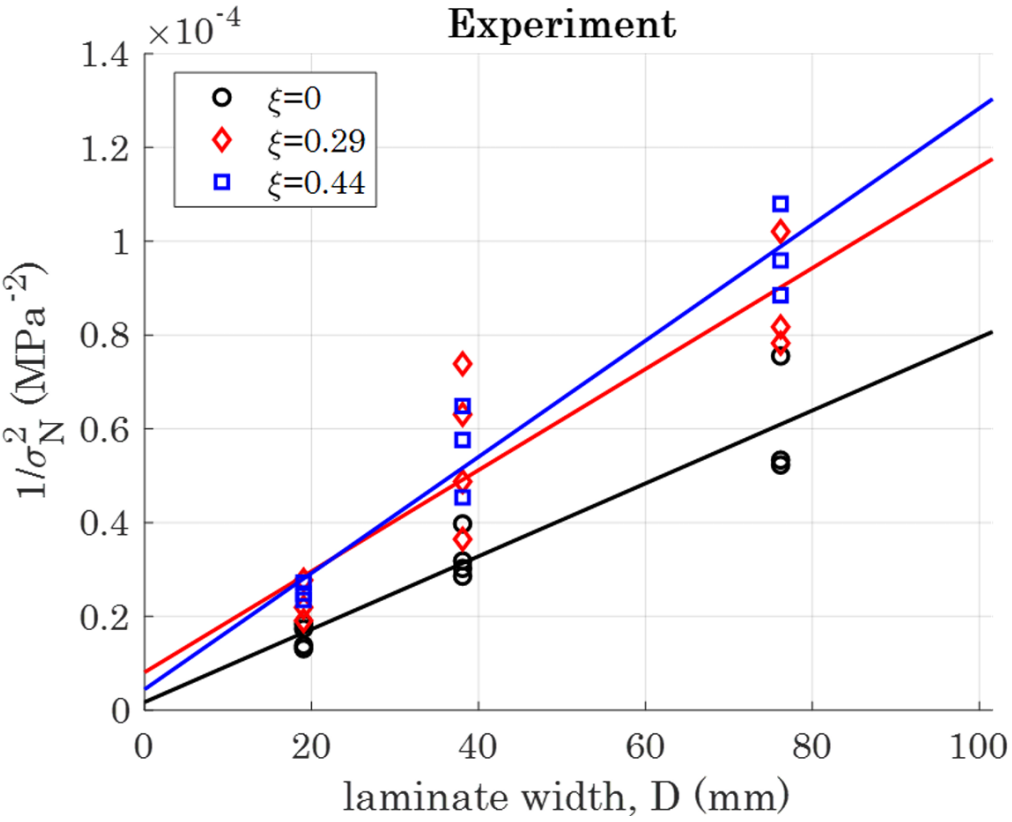

Figure 1.12 Linear regression plot of SEL for different ξ values [27].

Chapter – 2 Design and Evaluation of Specimen Geometry

2.1. First Design: Curved Bent Beam

2.1.1. Geometry and Test Method

The curved bent beam geometry follows ASTM D6415 [29], designed to determine the curved beam strength of continuous fiber-reinforced composite materials using a 90° curved beam specimen. The specimen consists of two straight legs connected by a 90° bend with an inner radius of 6.4 mm. The test applies loading such that the inner radius experiences tensile stresses, allowing evaluation of interlaminar tensile strength and delamination resistance in curved composite sections. This geometry is widely used for assessing structural elements in aerospace and other high-performance applications where curved laminate sections are common. The schematic of geometry of Curved bent beam is represented in Figure 2.1.

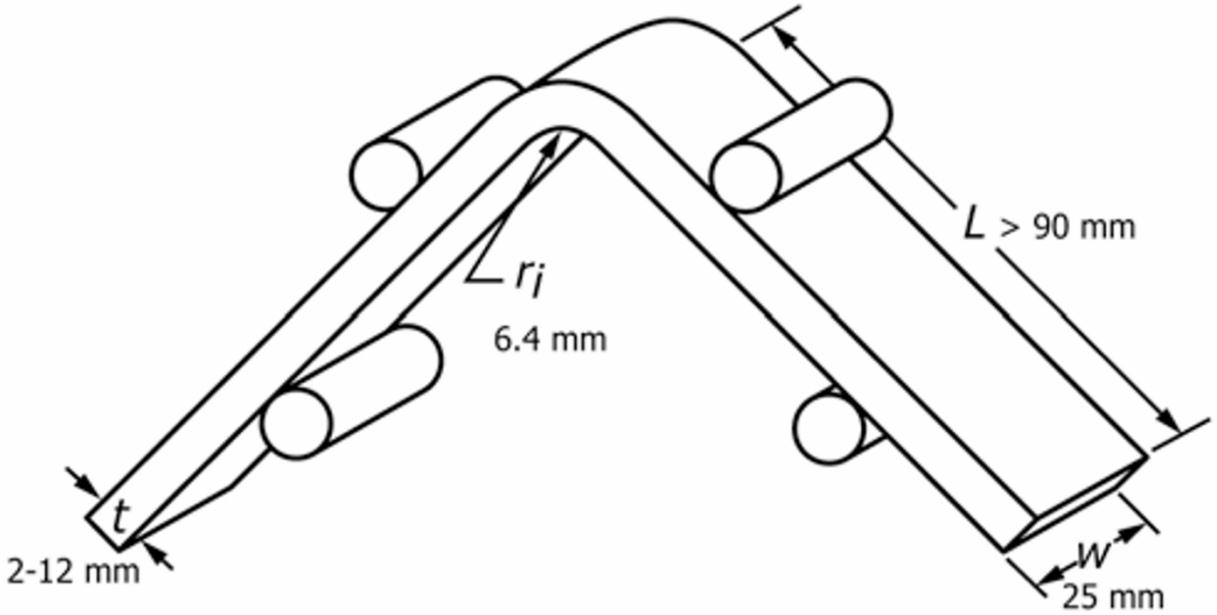

Figure 2.1 Curved bent beam specimen geometry for ASTM D6415 [29].

For this work, the ASTM D6415 curved beam geometry was adapted to generate crack-parallel tension during crack propagation. The standard D6415 test involves loading a 90° curved beam, consisting of two straight legs connected by a 6.4 mm (0.25 in.) inner radius bend, and for

this test a thickness of 4.2 mm is assumed, under four-point bending to produce a constant bending moment across the curved section. In its typical form, the test induces an out-of-plane tensile stress

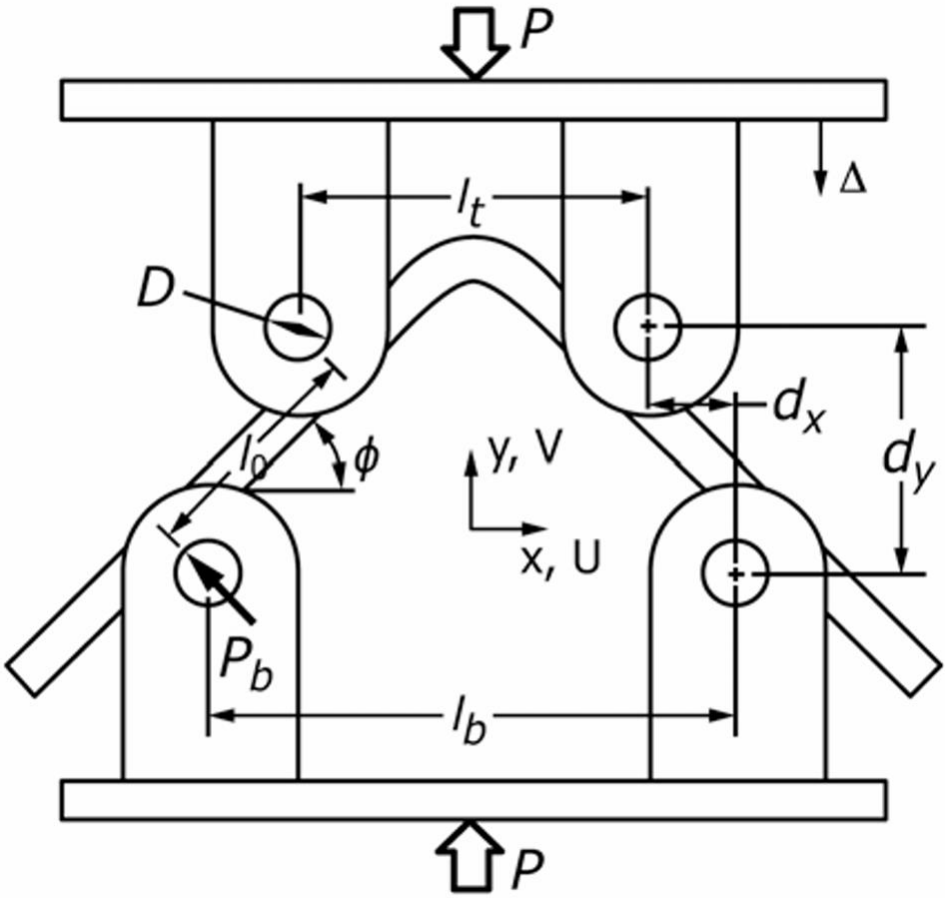

Figure 2.2 ASTM D6415 test setup [29].

in the curved region, leading to failure.

However, for this present study, a through-thickness crack seam was to be introduced along the length of the curved section, positioned at the neutral axis. Under four-point bending, the applied bending moment not only propagates the crack but also produces a crack-parallel tensile stress component aligned with the propagation direction. This crack-parallel tension varies with the applied load, making it non-constant throughout the test. The evaluation of this tensile stress focuses on the crack-tip region, as the curved geometry creates non-uniform stress distribution in

the mid-section—where the upper surface experiences compression. The crack's position within the curved section significantly affects the magnitude and distribution of crack-parallel tension, making careful placement critical for achieving the desired loading condition during propagation. The schematic of the ASTM D6415 test setup is illustrated in Figure 2.2.

2.1.2. Fracture Mode Analysis

To investigate the behavior of type of fracture happening in this test, the test was simulated in Abaqus, with the loading conditions as shown in Figure 2.3. To determine the type of fracture, the SIF of the fracture was to be determined, specifically K_I and K_{II} were to be determined, as this type of test can lead to both Mode I and Mode II fracture while Mode is II extremely rare and is not regarded in this. The SIF were to be determined using the equation (1.2):

$$K_{Ic} = \lim_{r\to\infty} \sigma_{yy}\sqrt{2\pi r} = Y\sigma_{\infty}\sqrt{\pi a}$$

Upon simplification for this test, we get:

$$K_{Ic} = \sigma_r\sqrt{2\pi r} \tag{2.1}$$

$$K_{IIc} = \tau_{r\theta}\sqrt{2\pi r} \tag{2.2}$$

Where, σ_r is the crack opening stress at the crack tip, $\tau_{r\theta}$ is the shear stress near the crack tip. The above equations (2.1) and (2.2) represented in logarithmic form can be used to determine the SIF.

$$\log K_{Ic} = \log \sigma_r\sqrt{2\pi r}$$

Which upon simplification, gives:

$$\log \frac{K_{Ic}}{\sqrt{2\pi}} - \frac{1}{2}\log r = \log \sigma_r \tag{2.3}$$

Which is in the form of Y = mX + C where X is log(r) and Y is log(σ_r). The data of the radial stress along the distance r in the crack propagation direction from crack tip was obtained and plotted and from the intercept of the log-log plot, the SIF of Mode I fracture was obtained. Similarly, the shear stress data obtained and using the same procedure, the SIF of Mode II fracture obtained. This procedure was done on multiple crack seam positions and lengths in the Abaqus model.

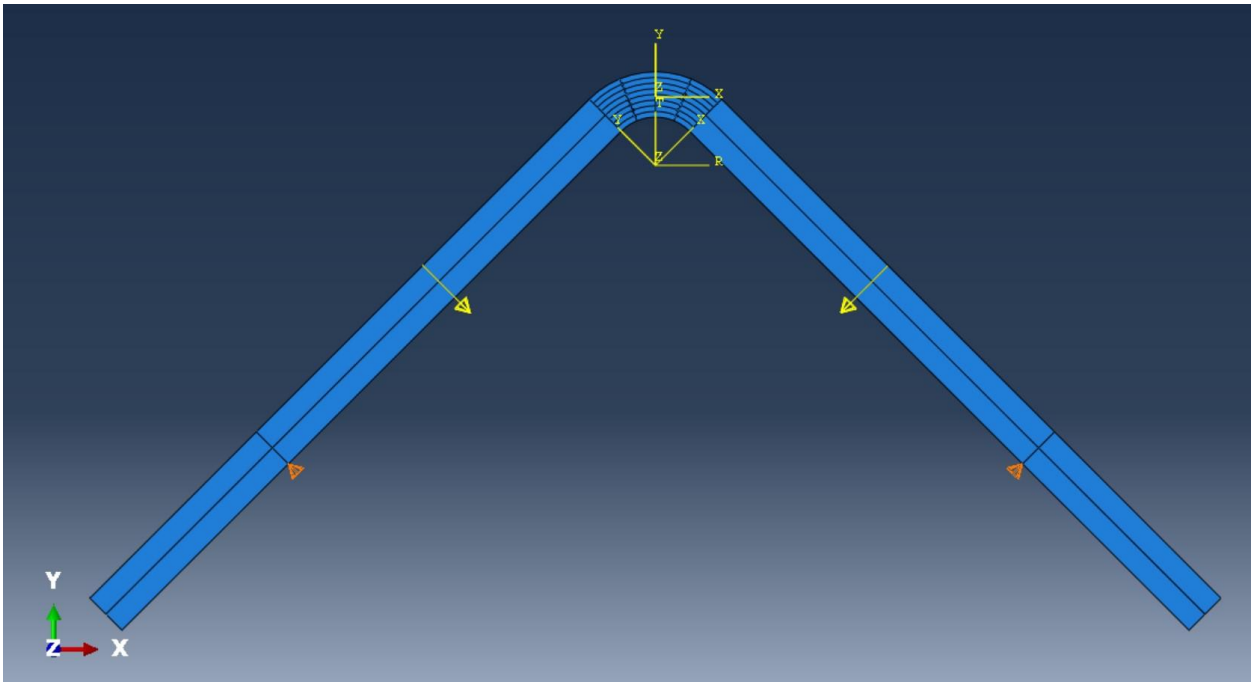

Figure 2.3 Curved bent beam test loading and boundary conditions [29].

2.1.3. Limitations

The fracture mode analysis was conducted on geometry with seam located at multiple position and with different seam lengths. The details of the crack seam position are given in Table 2.1.

Seam ID	Seam Position (mm)
Above	+1.5
Central	0
Below	-1.5

Table 2.1 Crack seam positions with respect to the Neutral axis of the curved bent beam.

The +/- sign indicate the direction from the neutral (central) axis, the + sign indicates in the upward direction while – sign indicates in the downward direction. The above crack positions have been

analyzed in combination with 0°, 45° and 90° crack seam angles which alter the length of initial crack. Figure 2.4 illustrates the SIF, K_I and K_{II} at different combinations of initial seam length and

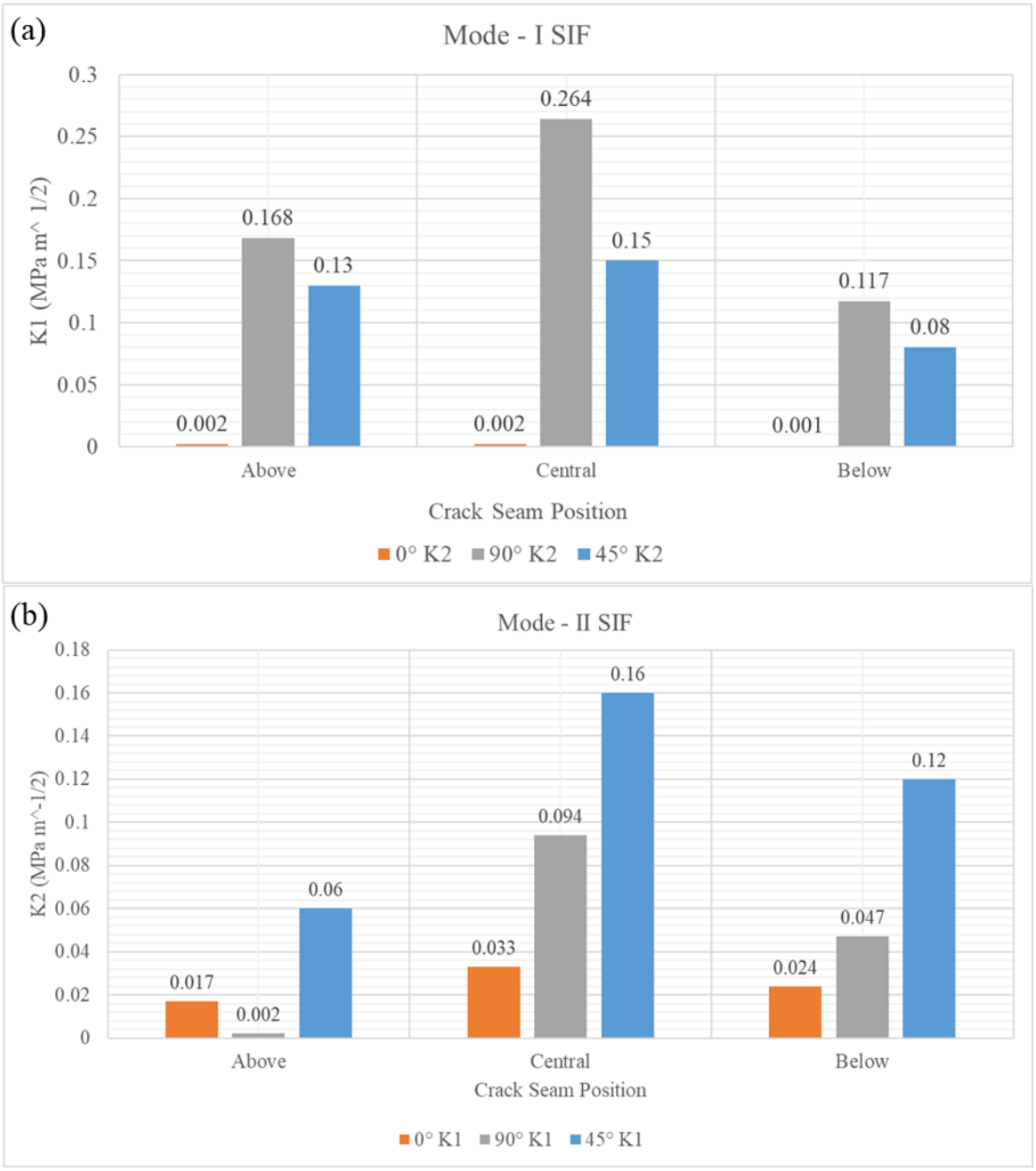

Figure 2.4 Stress Intensity Factors of (a) Mode I, (b) and Mode II in curved bent beam.

position and Figure 2.5 illustrates the K_I/K_{II} across all combinations showing the mixed mode behavior change. The ratio analysis shows that increasing the initial crack angle results in greater K_{II} dominance, indicating a stronger shear component in fracture behavior. Conversely, positioning the crack further inside the section, below the neutral axis, increases K_I dominance, highlighting a higher opening mode contribution. Regardless of these variations in fracture mode dominance, the crack parallel stress remains tensile in all cases. This consistent tensile nature is attributed to the bending-induced stress distribution in the curved beam, where the local stress state at the crack tip promotes crack opening along its length, independent of angle or location.

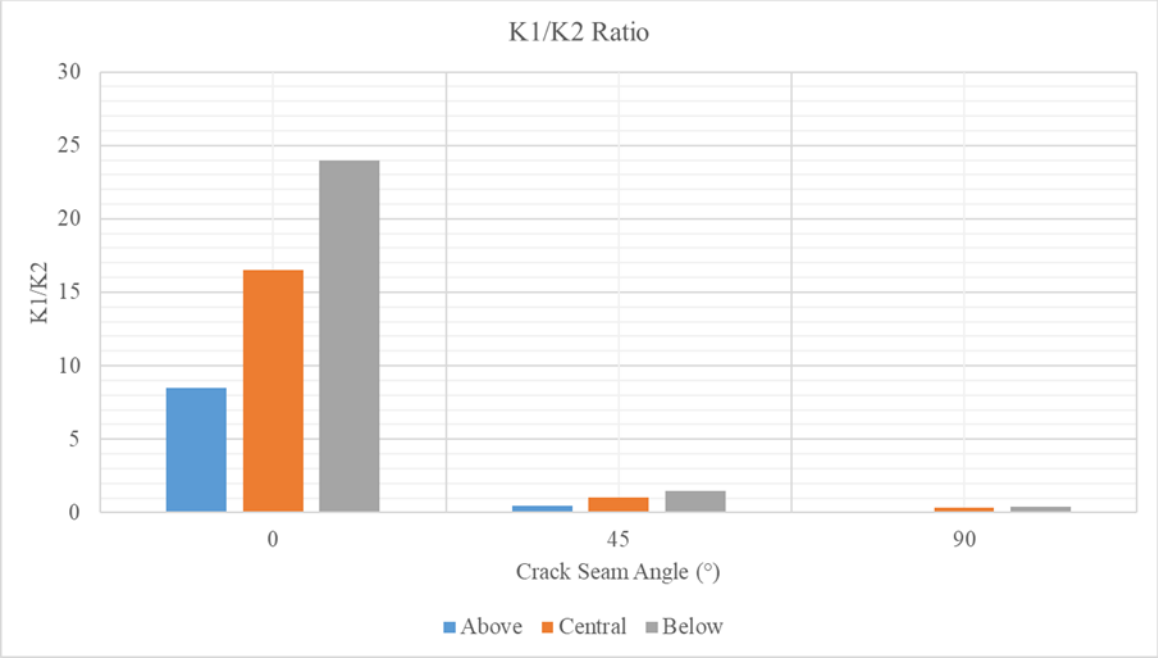

Figure 2.5 Stress Intensity Factors ratio of Mode I and Mode II.

The analysis indicates that achieving complete Mode I dominance requires an extremely small initial crack seam, around 0°, which corresponds to less than 5 mm—below the practical limit for experimental manufacturing, where at least 5 mm is feasible. Even at 0° and neutral axis position, Mode II components persist, preventing pure Mode I conditions. To maximize Mode I, the crack would need to be positioned near the bottom surface with a very short length, a configuration that is challenging and unrealistic for experiments. Therefore, the curved bent beam

geometry is unsuitable for studying Mode I crack parallel tension due to these practical and experimental limitations.

2.2. Second Design: Open-I

2.2.1. Motivation and Geometry Description

Since the curved bent beam was found unsuitable, the need arose for a new design. Inspiration came from the single lap shear test geometry, also referred to as the thin lap shear test, as shown in Figure 2.6. This is one of the most widely used methods for generating data on adhesively bonded joints. However, the standard single-lap configuration does not truly measure pure shear strength. Peel stresses often induce a Mode I opening at the edges of the bonded area, even though the test is intended to primarily evaluate shear. This occurs because the lap joint's geometry introduces bending moments and eccentric loading, leading to a combination of shear and peel stresses at the interface [30]. The bending moment and resulting bond rotation create a non-uniform stress distribution, with failure often occurring due to peel stresses at the interface edges. The observation that geometric eccentricity inherently generates bending and thus Mode I opening motivated the development of a new geometry, later termed Open-I.

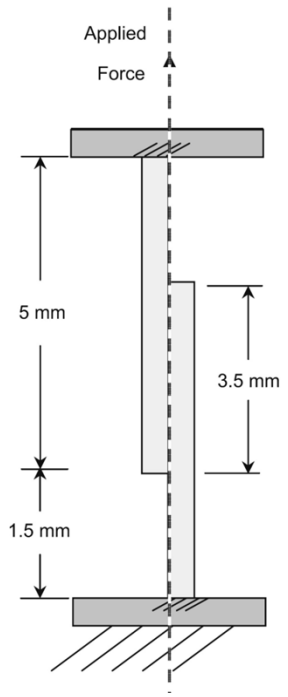

Figure 2.6 Traditional single lap shear geometry and loading [30].

Using the concept of bending moment generation due to non-uniform stress distribution as the focal point, a new geometry was developed. This geometry also induces bending moments, but through planned changes in cross-section that cause uneven tensile stress distribution when subjected to tensile loading. It is similar in appearance to a dog-bone specimen used in standard tensile testing, such as ASTM D3039 [31], consisting of a thinner middle section and wider ends.

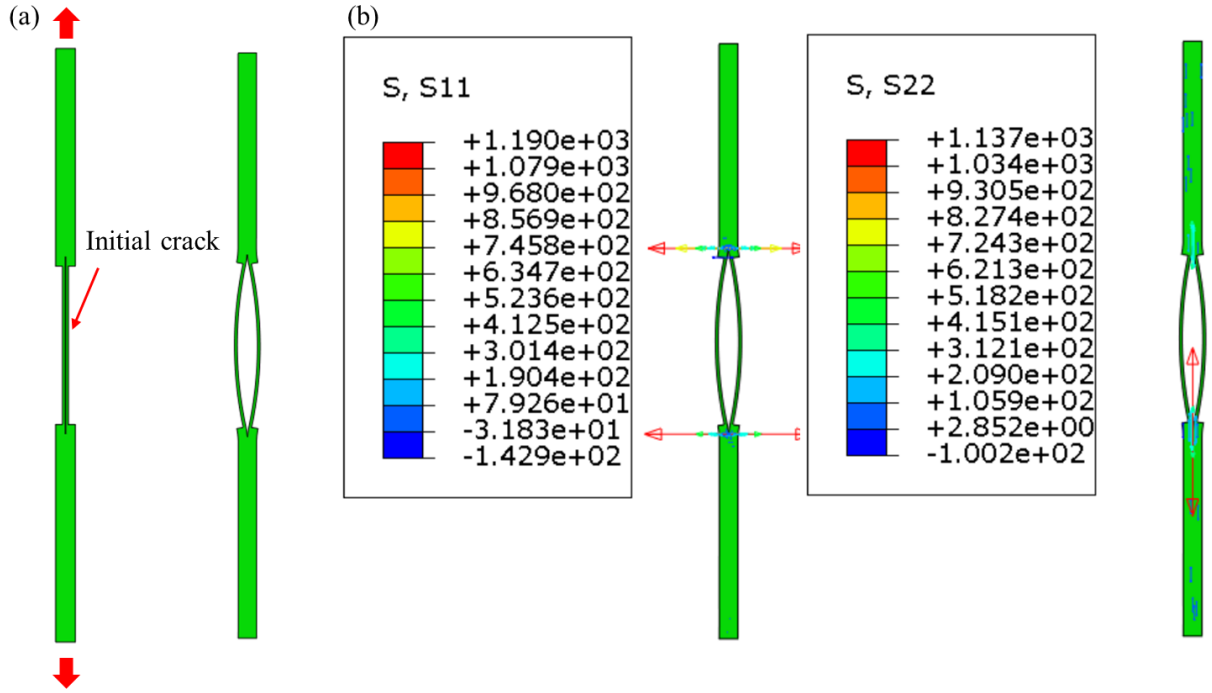

Figure 2.7 (a) New geometry based on single lap shear and mechanism under tensile loading, (b) presence of both crack opening tensile stresses (S11) and crack parallel tensile stresses (S22) (MPa).

The crack seam is positioned along the neutral axis, running through the entire thin section and extending into the wider section, as shown in Figure 2.7. This extension is crucial: the crack effectively divides the transition region between the thin and wide sections into two distinct regions. Under tensile loading, the width change in the geometry causes non-uniform stress distribution in each separated region, resulting in bending moments that promote crack opening.

If the crack does not extend far enough into the wider section, the two separated regions effectively merge into a single continuous section. In that case, even though the geometry still produces non-uniform stresses, the symmetry ensures that bending moments cancel out, and the test reverts to behaving like a standard tensile test. Thus, precise crack positioning and extension are essential for achieving the intended bending-induced crack opening in this design.

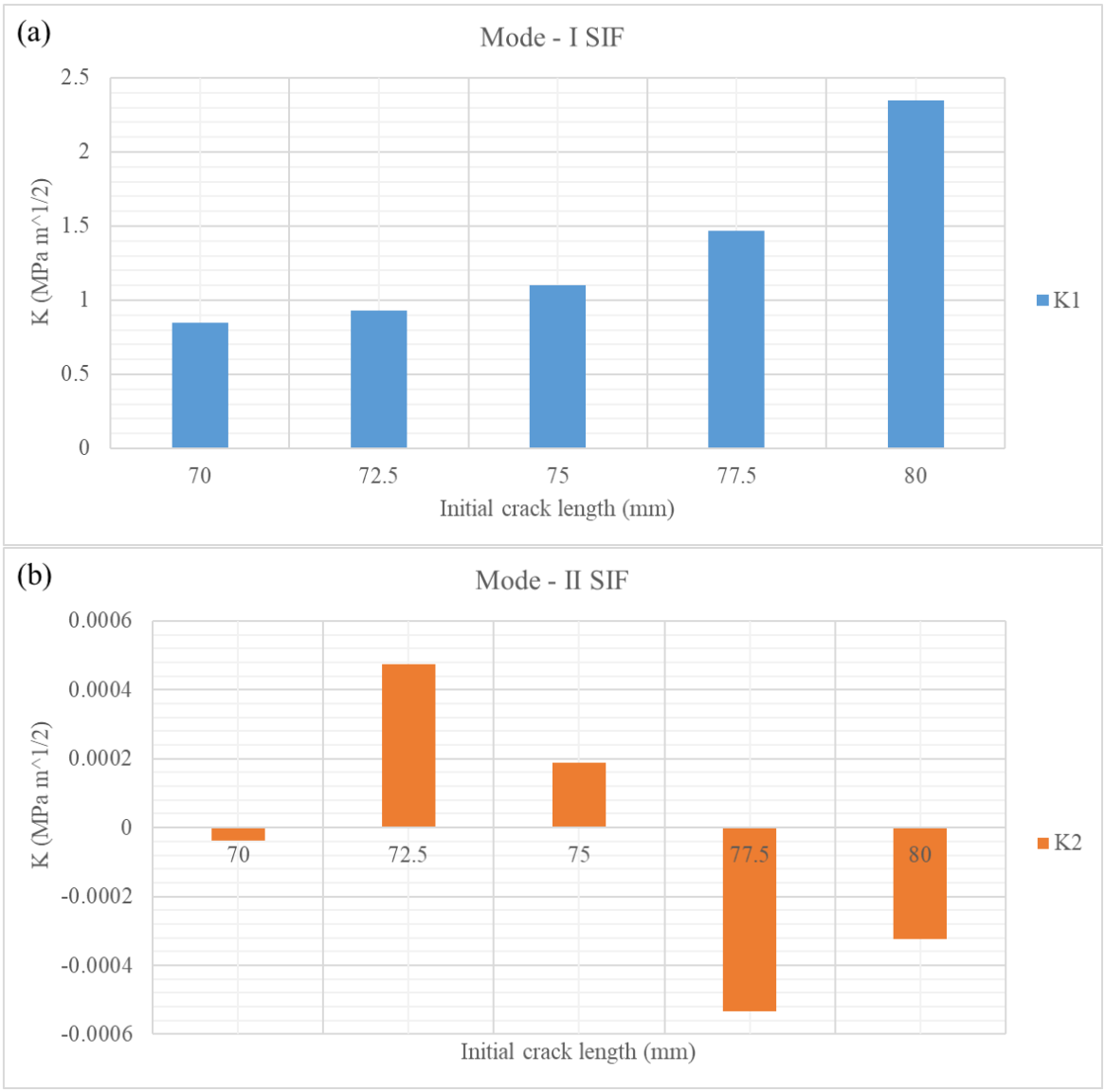

Figure 2.8 Stress Intensity Factors of (a) Mode I, (b) and Mode II in new geometry.

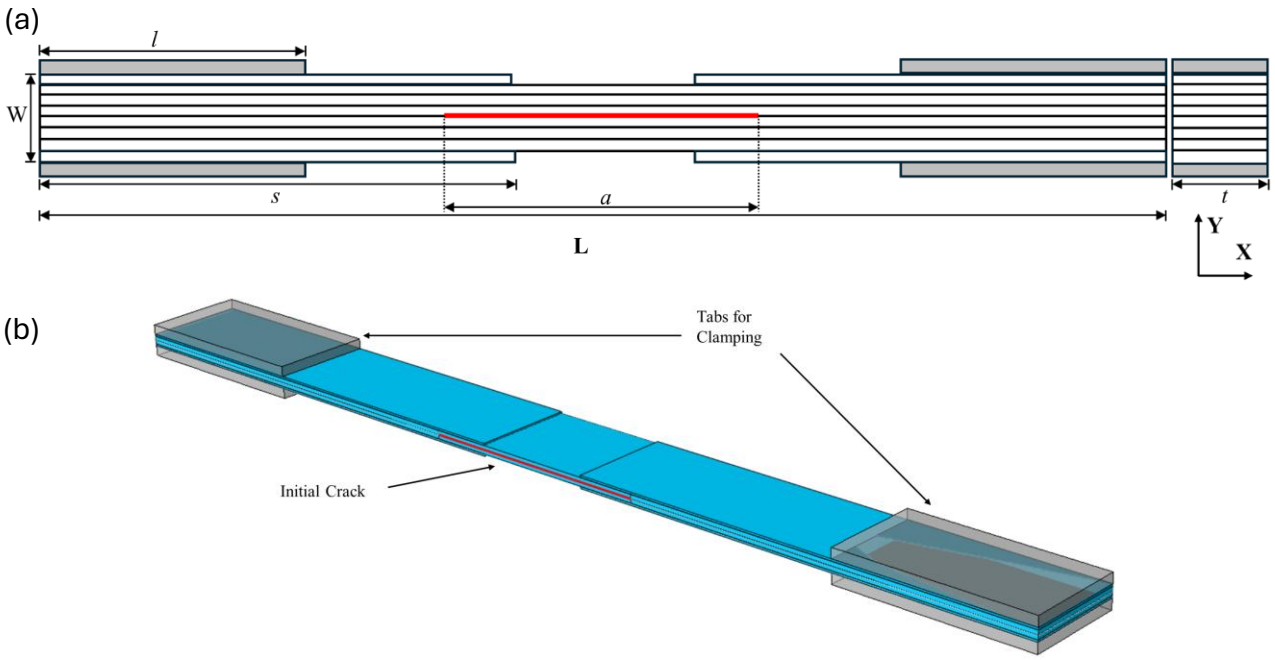

Figure 2.9 (a) Open I specimen schematic (b) Open I geometry.

L (mm)	W (mm)	*t* (mm)	*s* (mm)	*a* (mm)	*l* (mm)	Tab thickness (mm)	Ply thickness (mm)
300	1.04	25	120	70	50	2.55	0.13

Table 2.2 Open I specimen dimensions.

2.2.2. Fracture Mode Analysis

Fracture mode analysis for the new geometry was conducted using the same procedure applied to the curved bent beam (see Section 2.1.2). Multiple initial crack lengths were examined, ranging from 70 mm to 80 mm in increments of 2.5 mm. The Mode I and Mode II stress intensity factors (SIFs) are presented in Figure 2.8. As shown in Figure 2.8a, increasing the initial crack length results in a steady increase in Mode I SIF, K_I, while Mode II SIF, K_{II} fluctuates between compressive and tensile values. Furthermore, K_I is approximately 10^3-10^4 times greater than K_{II}, clearly indicating that Mode I fracture completely dominates in this geometry. This dominance is

maintained across all crack lengths investigated, confirming the design's suitability for generating near pure Mode I fracture.

2.2.3. Final Specifications and Limitations

Further analysis of the geometry showed that shifting the crack seam away from the neutral axis increases Mode II SIF, suggesting the possibility of mixed-mode fracture accompanied by crack-parallel tension. Although this crack-parallel tension is not constant during loading, it can be controlled and maintained within a desired range throughout the test by adjusting the relative lengths of the wider and thinner sections. As the crack propagates, the magnitude of the crack-parallel tension changes; however, the initial and final values during propagation can be reasonably approximated. This allows the design to be tuned for consistent crack-parallel tension conditions, enabling more controlled studies of mixed-mode fracture behavior in this geometry. This novel

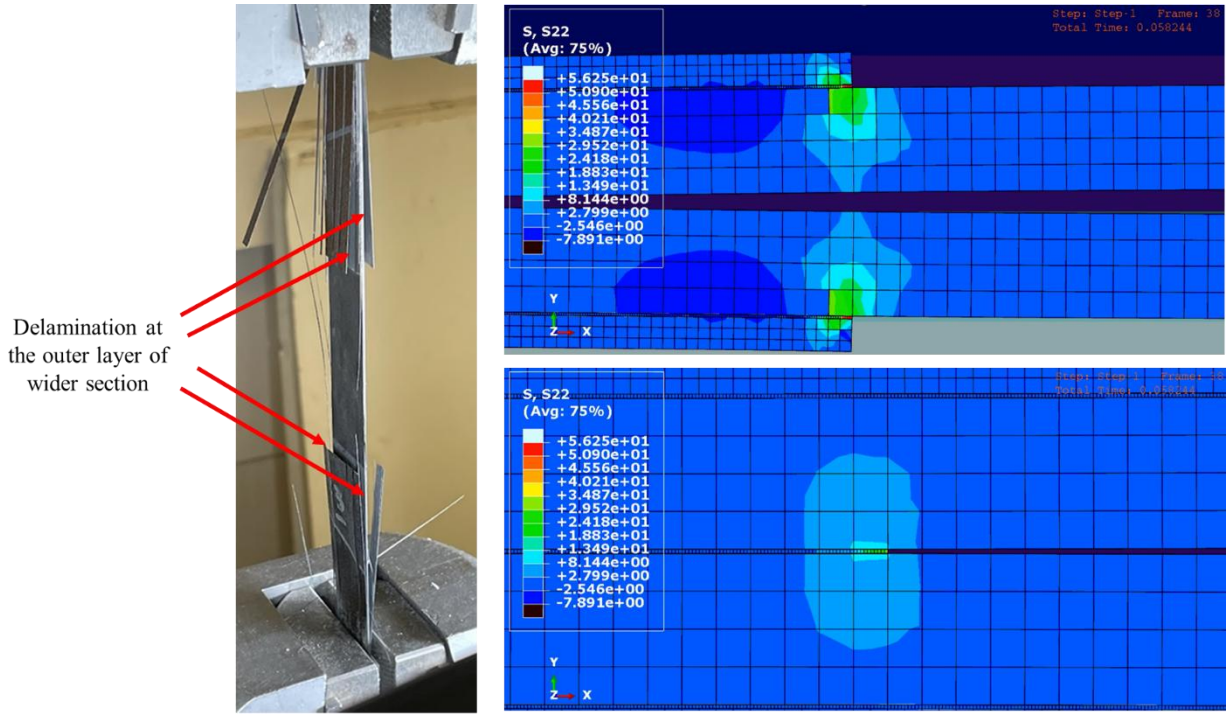

(a) (b)

Figure 2.10 (a) Delamination Failure (b) FEA damage analysis, the outer layer (top) is experiencing more opening stress (S22) compared to the crack tip (bottom).

test has been coined the “Open I Test” due to the shape of geometry being like the letter “I” and the mechanism of the test being like the opening of eye.

For this thesis, the geometry was finalized to produce a crack-parallel tension within 22–38% of the material’s UTS, with all 8 composite layers oriented unidirectionally (0°). The geometry specifications of the Open I test specimen are shown in Figure 2.9 and Table 2.2. During physical testing, minor crack propagation was observed in the initial loading stage; however, the remainder of the test consistently resulted in delamination of layers in the wider section of the specimen. This failure occurred in all manufactured samples, with failure loads averaging around 28 kN.

The test was also simulated in Abaqus using damage analysis approach to examine the fracture behavior. The Abaqus deformation showed that, as shown in Figure 2.10b, as the applied load increased, the crack propagated slightly in the early stages. With further loading, the bending moment increased, and its influence shifted toward the outer composite layers in the wider section. This stress redistribution led to progressive delamination of all four outer layers, as shown in Figure 2.10. Eventually, complete failure occurred once the delamination extended sufficiently through the section. The simulated behavior closely matched the experimental observations, confirming that the geometry effectively generated both the intended crack-parallel tension and bending-induced stresses, and that the resulting failure mechanism was dominated by delamination in the thicker section.

2.3. Final Design: Half-Open I

2.3.1. Open I Modifications and Final Geometry

To explore an alternative crack propagation path that avoids delamination, attention was given to the non-tapered corner at the section transition area, which acted as a stress concentration region where most of the bending moment was concentrated. To eliminate this section transition, a modified test configuration with no change in specimen width was considered.

One of the semi-delaminated specimens was selected for modification. The partially detached outer layer was carefully removed without disturbing the intact layers, resulting in

uniform width geometry. To induce a non-uniform stress distribution and promote crack propagation under crack-parallel tension, the specimen was cut in half along its mid-section, producing halves of the specimen. The crack front faces were then opened, without further crack growth by inserting Glass Fiber Reinforced Polymer (GFRP) tabs, the same material used for the clamping tabs. The inserted tab thickness was the amount of displacement of crack front edges, creating an opening similar to the deformed shape of an Open I specimen, but without any prior crack extension.

This modified specimen was then subjected to tensile loading. The presence of the inserted tab introduced a slight change in geometry at the section where it was placed, generating an initial bending moment. Upon axial tensile loading, this bending moment increased, facilitating crack propagation from the pre-opened front. This approach produced a modified version of the Open I configuration, half the original specimen, with uniform width, and initial bending induced by the inserted tab. This new geometry was termed the “Half-Open I” (HOI).

The newly developed Half-Open I geometry met all the required criteria. Crack propagation occurred under the presence of crack-parallel tensile stresses, and the removal of section transitions eliminated stress concentration regions that could have caused deviations from the intended fracture mechanism. Furthermore, the geometry ensured a controlled stress distribution, enabling the desired crack growth behavior. Analysis revealed that the Half-Open I configuration corresponded to a negative geometry (see Section 1.3.5), meaning that the applied loading conditions produced stable crack growth. This allowed for detailed observation of the fracture process under sustained crack-parallel tension, although it came at the cost of losing the ability to apply Bažant-type size effect law for the estimation of FPZ and G_f.

The finalized geometry closely resembled the double cantilever beam (DCB) configuration described in ASTM D5528/D5528M-21 [32], which is typically used to evaluate Mode I interlaminar fracture toughness. Compared to the Open I, a new feature was introduced, the tab insertion, which created the desired crack-parallel tensile stresses and the magnitude of these tensile stresses, relative to the UTS, depended on the thickness of the inserted tab. To maintain consistency and comparability, the specimen dimensions were kept as close as possible to those

specified in the ASTM standard for the DCB geometry. The schematic representation and detailed dimensions of the final Half-Open I geometry are presented in Figure 2.11 and Table 2.3.

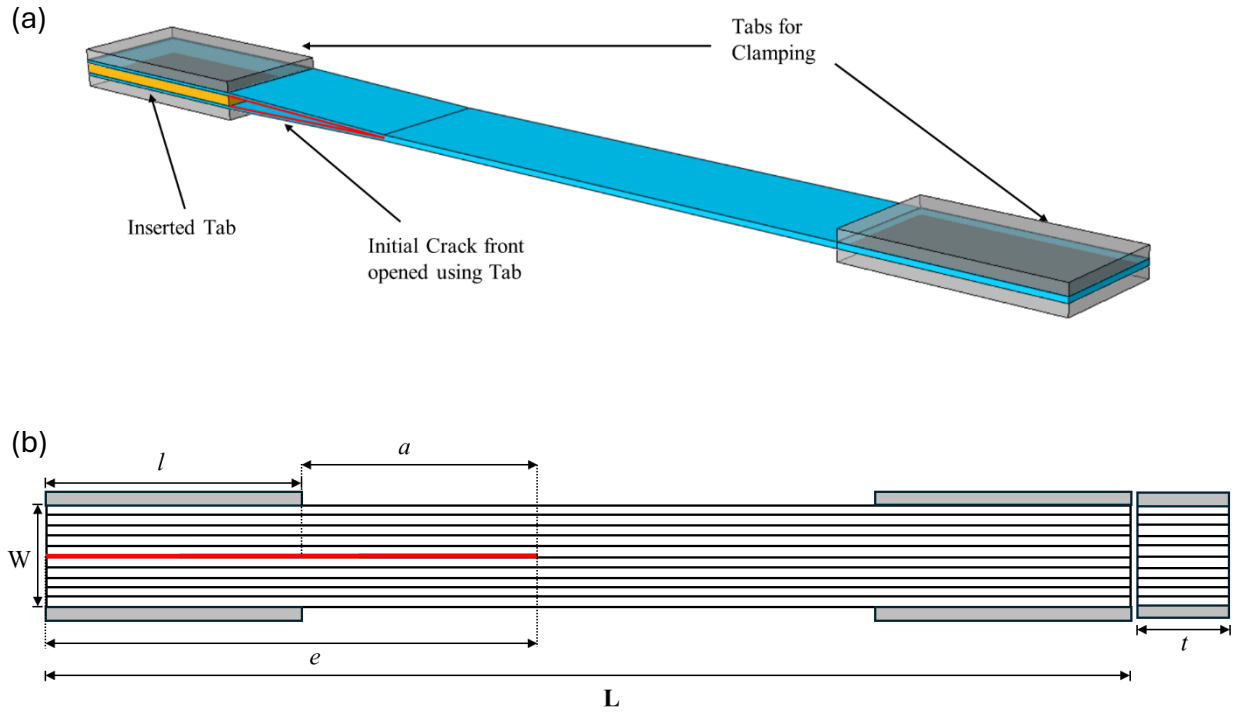

Figure 2.11 (a) Half-Open I specimen geometry (b) Half-Open I geometry schematics.

L (mm)	W (mm)	t (mm)	l (mm)	e (mm)	$e - l = a$ (mm)	Clamping Tab thickness	Ply thickness
270	1.3	25	50	100	50	2.55	0.13

Table 2.3 Half-Open I specimen dimensions.

For this test, multiple thicknesses of GFRP tabs were selected for insertion into the crack to facilitate controlled crack-front opening. With each increase in tab thickness, the initial bending moment also increases, causing crack propagation to initiate and terminate at different load levels. This variation enables the generation of experimental data from which the required R-curves can be plotted for a constant level of crack-parallel tension, by extracting and processing the results

from these tests. The complete procedure for obtaining and analyzing this data will be discussed later in in Section 1.1. The specific thicknesses of the GFRP tabs used for insertion in the specimens are provided in Table 2.4.

Tab ID	Thickness (mm)
2p1	2.1
2p4	2.8
2p8	2.8
3p2	3.2
3p6	3.6
4p15	4.15
4p55	4.55
4p8	4.8
5p2	5.2

Table 2.4 Half-Open I insert-tab thicknesses.

2.3.2. **Initial Crack Seam Length**

From the preliminary results and initial crack propagation observations in the Half-open I geometry tests, the initial crack seam length was reduced from 50 mm to 5 mm. This change was intended to increase the available crack propagation length, enabling the plotting of more detailed R-curves without altering any other specimen dimensions.

However, with the shorter crack seam, tab insertion resulted in the formation of pre-cracks, non-loaded crack propagation prior to the start of testing. As a result, the measured fracture energy at the beginning of loading appeared higher than zero. This effect is attributed to a potential increase in the FPZ length, likely caused by fiber bridging initiated during tab insertion.

The presence of pre-cracks prevented accurate extraction of constant crack-parallel tension R-curve data. To obtain the required data, the initial crack seam length must be sufficiently long to prevent any pre-loading crack propagation when the tab is inserted, ensuring that the crack begins propagating only under applied load.

Chapter – 3 Specimen Manufacturing and Experimental Testing

This work investigates the fracture behavior of composite materials under a biaxial stress state, where one stress component is parallel to the crack and tensile in nature. Based on the reasoning outlined in Section 1.4, it is anticipated that fracture energy will vary with the level of biaxiality. Prior studies suggest that when the crack-parallel stress is compressive, a measurable effect on fracture behavior is observed, typically a decrease in fracture resistance for composites and an increase for concrete upto a crack parallel compression stress value.

Given the novelty of the Half-Open I test and the aim of examining the influence of crack-parallel tension, a straightforward tensile loading method is selected to generate the required parallel stress. This approach mirrors the method used for compression generation along crack front in the Gap Test but is adapted for tension. The experimental configuration is derived from the standard Double Cantilever Beam test described in ASTM D5528/D5528M-21 for Mode I interlaminar fracture toughness evaluation.

The key distinction between the Gap Test on composites and the Half-Open I test lies not only in the nature of the crack-parallel stress but also in the fracture geometry. The Gap test employs a positive geometry, whereas the HOI test utilizes a negative geometry. In the HOI configuration, it is possible to observe both stable crack propagation and regions of instability, depending on the crack growth stage. In contrast, the Gap test is dominated by unstable crack propagation, making such observations challenging. While the Gap test enables estimation of fracture energy and FPZ size using the size effect law, this capability is not feasible in the HOI test. However, the HOI test offers the advantage of extracting multiple crack-parallel tensile loading R-curves, providing unique insights into fracture behavior.

Also, a critical requirement for successful HOI testing is the use of GFRP tabs that remain undeformed throughout the experiment. GFRP is inexpensive, readily available, and can typically be sourced within a few days. As described in Section 2.3.1, the HOI test specimen geometry closely resembles that of the Double Cantilever Beam (DCB) specimen. A predetermined crack length is introduced, and tensile loading is applied. Since the fracture mode under investigation is Mode I interlaminar, the crack seam is produced by inserting a Teflon film between prepreg layers

prior to curing. The detailed specimen manufacturing procedures and experimental considerations are presented in the following sections.

3.1. Material Properties: *IM7/977 – 3*

The CFRP examined in this study is composed of IM7 fiber and 977-3 thermoset epoxy. IM7 is a continuous, high-performance, intermediate-modulus PAN-based carbon fiber, while 977-3 is a thermoset epoxy resin designed for autoclave and press molding cure cycles. Clay et al. [33] have reported the fundamental mechanical properties of a representative IM7/977-3 composite, which closely matches the material used here. These properties, summarized in Table 3.1, are adopted for the present work. Under the assumption of transverse isotropy, the elastic moduli are taken as $E_{3T} = E_{2T}$, and the Poisson's ratios satisfy $\nu_{13} = \nu_{12}$.

Property	Symbol	Value
Longitudinal tensile modulus (GPa)	E_{1T}	164 ± 4.12
Transverse tensile modulus (GPa)	E_{2T}	8.98 ± 0.284
In-plane shear modulus (GPa)	G_{12}	5.01 ± 0.249
Major Poisson's ratio	ν_{12}	0.32 ± 0.0266

Table 3.1 Mechanical Properties of Unidirectional IM7/977-3 laminate [33].

3.2. Composite Laminate Manufacturing

The composite manufacturing process employed in this study mirrors that used in industry for producing aerospace-grade components, ensuring the experimental results are relevant and transferable to real-world applications. As noted previously, the material system for the Half-Open I testing is unidirectional IM7/977-3. A concise overview of the manufacturing procedure is provided below; however, it should be noted that composite fabrication involves numerous subtleties that are beyond the scope of this work. Readers seeking an in-depth treatment of these intricacies are referred to the Composite Materials Handbook, Volume 3 [34], which offers comprehensive guidance on advanced composite manufacturing practices.

The composite material utilized in this study is a pre-impregnated system, commonly referred to as “pre-preg,” in which high-strength carbon fibers are already infused with the polymeric matrix. The matrix in this state is partially cured, typically in a B-staged condition, which allows the material to remain workable while preventing full curing before fabrication. To maintain this condition and avoid premature polymerization, the pre-preg material is stored under frozen conditions, generally at approximately 0°F. The material is rolled around a cylindrical core, often cardboard, to ensure the fibers remain straight and undamaged, preventing warping or breakage during storage. Moreover, the pre-preg is kept in airtight packaging to prevent moisture ingress, which can lead to voids, porosity, or incomplete curing during the final consolidation process.

Prior to use, the composite must be carefully thawed to restore sufficient pliability for handling and layup. The required thawing period varies with the roll size and material type; for IM7/977-3, a window of approximately 1-3 hours is recommended. A practical method for assessing readiness involves examining the bag surface for condensation: visible condensation indicates that the material is still too cold, while a condensation-free surface suggests adequate thawing. This careful handling procedure ensures that the pre-preg maintains its optimal workability and minimizes defects during layup, ultimately contributing to the integrity and mechanical performance of the cured composite components used in the Half-Open I testing.

Once the pre-preg material has adequately thawed, it is laid out on the Zünd G3 L-2500 Digital Cutter System [35] at the University of Washington Advanced Composites Center (ACC) [36]. The Zünd G3, shown in Figure 3.1, is a high-precision CNC cutter equipped with a powered rotary tool that accurately cuts the pre-preg plies to the exact dimensions required for the specimen layup. During cutting, the system applies a vacuum to hold the material securely in place, ensuring clean, precise edges without fiber distortion. Once all required plies are cut, they are organized and stored placed on a steel tool plate for further procedure, while any remaining pre-preg is carefully re-bagged and returned to the freezer for future use.

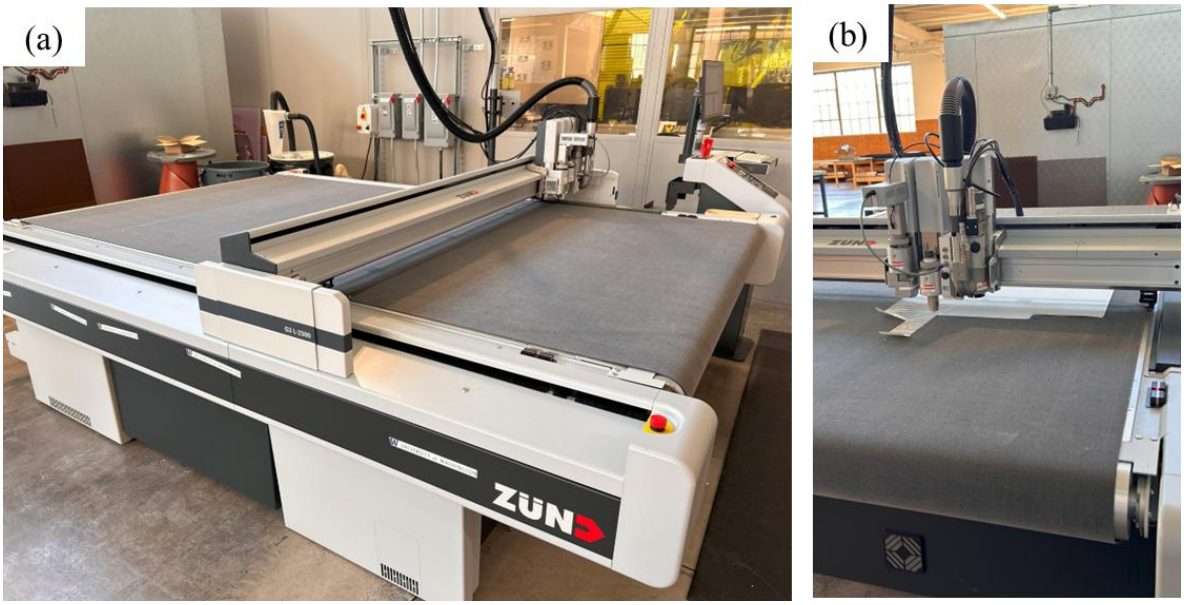

Figure 3.1 Zund G3 L-2500 Digital Cutter System at University of Washington Advanced Composites Canter (ACC) (a) overview (b) cutting module [35].

The next step involves manually stacking the pre-cut composite plies atop the flat steel plate to achieve the desired shape, dimensions, and stacking sequence, a process referred to as layup. To mitigate the risk of fiber splitting under the high biaxial stresses applied at the crack tip, a cross-ply laminate was chosen with the stacking sequence [0/90/0/90/0], mirrored on the opposite side of the crack seam, resulting in a total of 10 plies. The complete layup process typically takes 30–40 minutes. During layup, a debulking step is performed on the first ply, after five plies, and on the final ply, applying a minimum vacuum pressure of 26 inHg for at least 10 minutes and for about 7-12 hours for the final ply, to remove trapped air and ensure proper consolidation. After the first five plies, a 0.0005" DuPont™ Type A optically clear FEP film, made from Teflon™ fluoroplastic, is inserted at the mid-plane to create the initial crack for Mode I fracture propagation [37].

Debulking involves placing a vacuum bag over the in-process layup and applying vacuum pressure to remove trapped air between the plies while increasing compaction between adjacent layers. The debulk vacuum bag is specially constructed with a layered anatomy that maximizes

airflow, ensuring the production of a high-quality composite part. Both the layup and vacuum bagging procedures were performed following established vacuum bagging basics [38], [39] to achieve optimal consolidation and minimize void content. The bagging procedure is demonstrated in Figure 3.2.

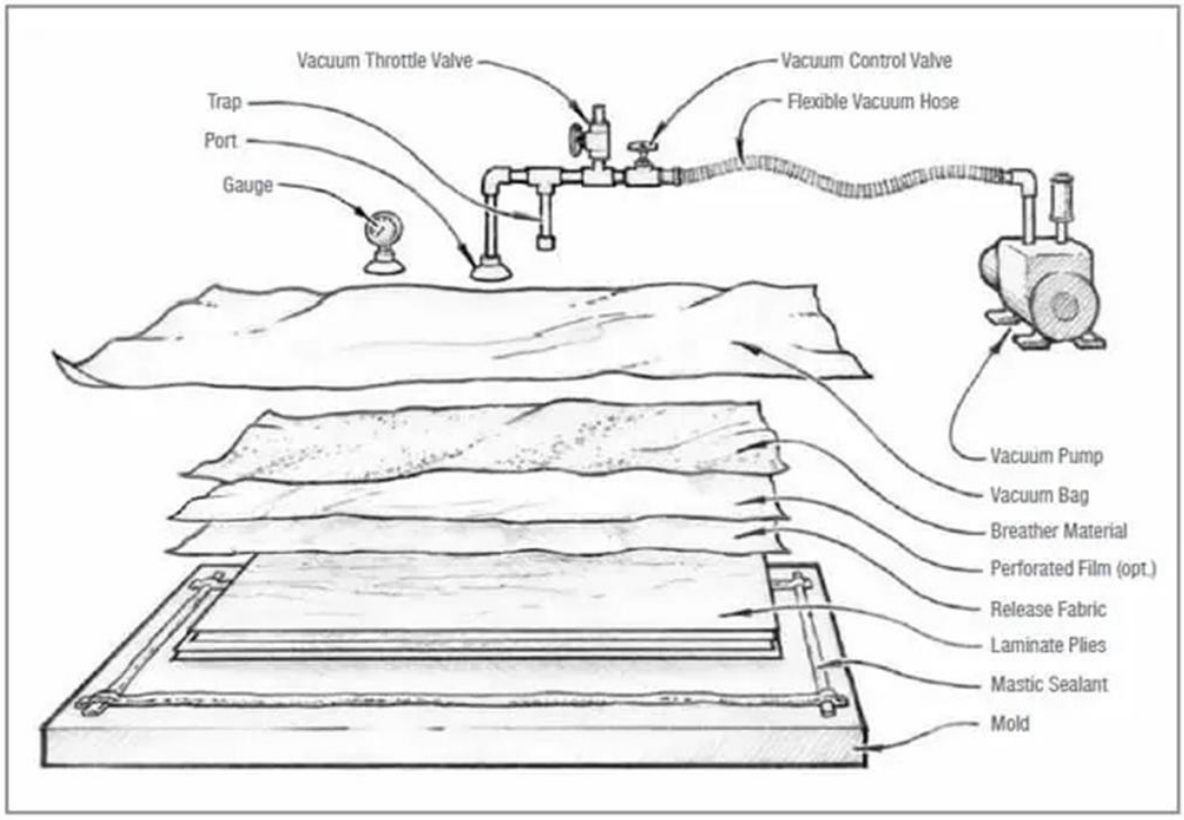

Figure 3.2 Schematics of a sandwich layup for vacuum bagging [38].

After the layup is complete, the composite part is prepared for curing. A series of images regarding the layup and bagging procedure are shown in Figure 3.3. The stacked prepregs are placed in an American Autoclave Co. autoclave and cured following the manufacturer's recommended temperature and pressure profile, as shown in Figure 3.4 [40], [41]. In practice, the cooling stage deviates slightly from the preset curve, descending exponentially in accordance with heat transfer principles.

Once the cure cycle is complete, the laminates are removed from the tooling plate using industrial hot gloves and allowed to cool to room temperature, often occurring inside the autoclave itself. The cure bag is then removed, and a visual quality inspection of the cured composite is performed. Potential defects observed at this stage may include foreign object debris, porosity, discoloration, or fiber separation, which can indicate improper cure procedures. Although visual inspection is typically done after the final curing step, it is considered good practice to inspect after each stage of processing to ensure higher specimen quality. No visual defects were observed in any of the laminates used for the Half-Open I test.

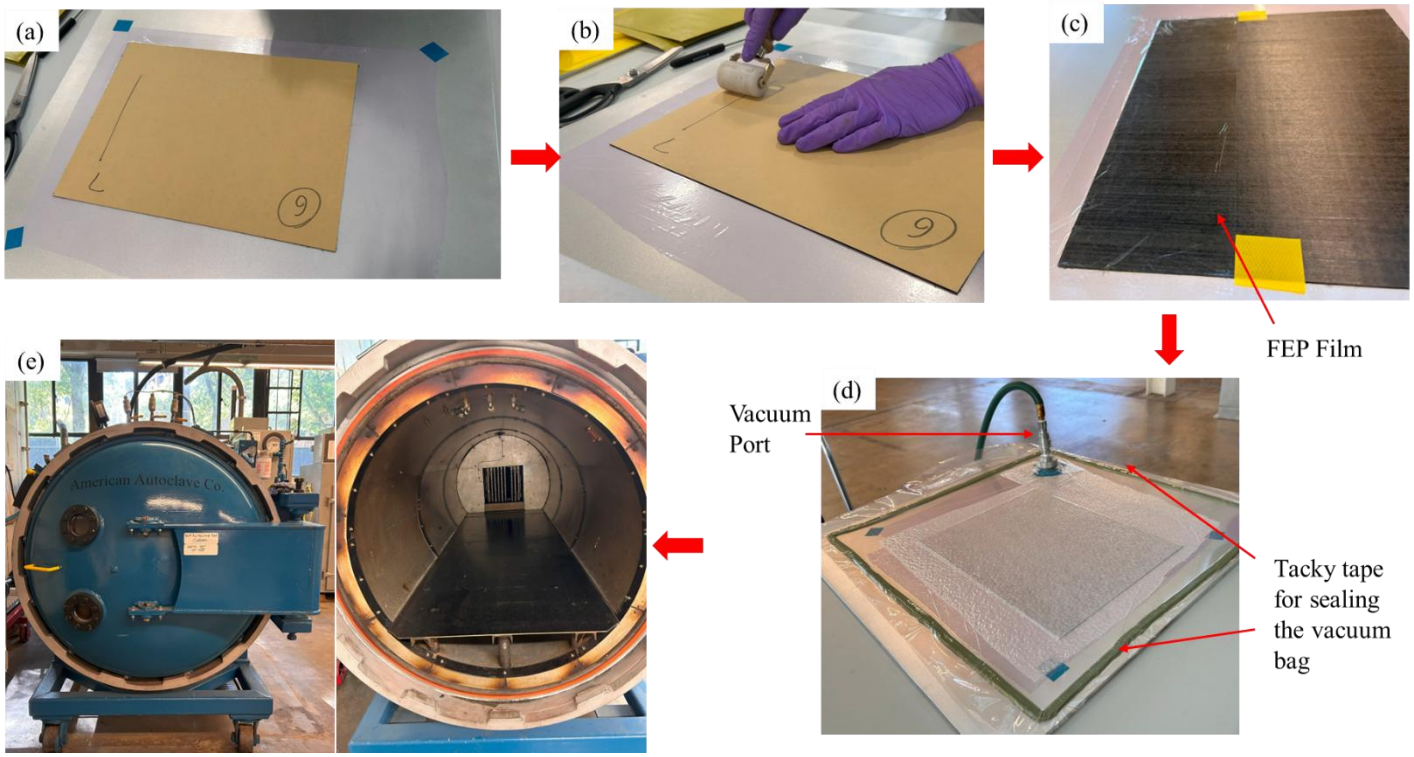

Figure 3.3 IM7/977-3 laminate manufacturing procedure. (a) Pre-preg sheet laid on a non-porous release film covered steel plate. (b) Hand lay-up process, using roller to remove any air pockets between the layers. (c) Insertion of FEP film for creating the crack. (d) Vacuum bagging of the laid-up pre-preg laminate. (e) American Autoclave used for curing of the debulked laminate.

As a safety note, cured composite parts often exhibit a knife-edge condition due to ply terminations at slightly different locations along the part boundaries. Because hand layup can cause

slight ply misalignments, maintaining this misalignment within a 3–5° margin is recommended. These sharp edges can easily cause lacerations and moreover after cutting of the laminates or after the testing process, the fiber sometime come apart and may penetrate the skin, causing harm; therefore, cut-resistant gloves should always be worn when handling cured composites.

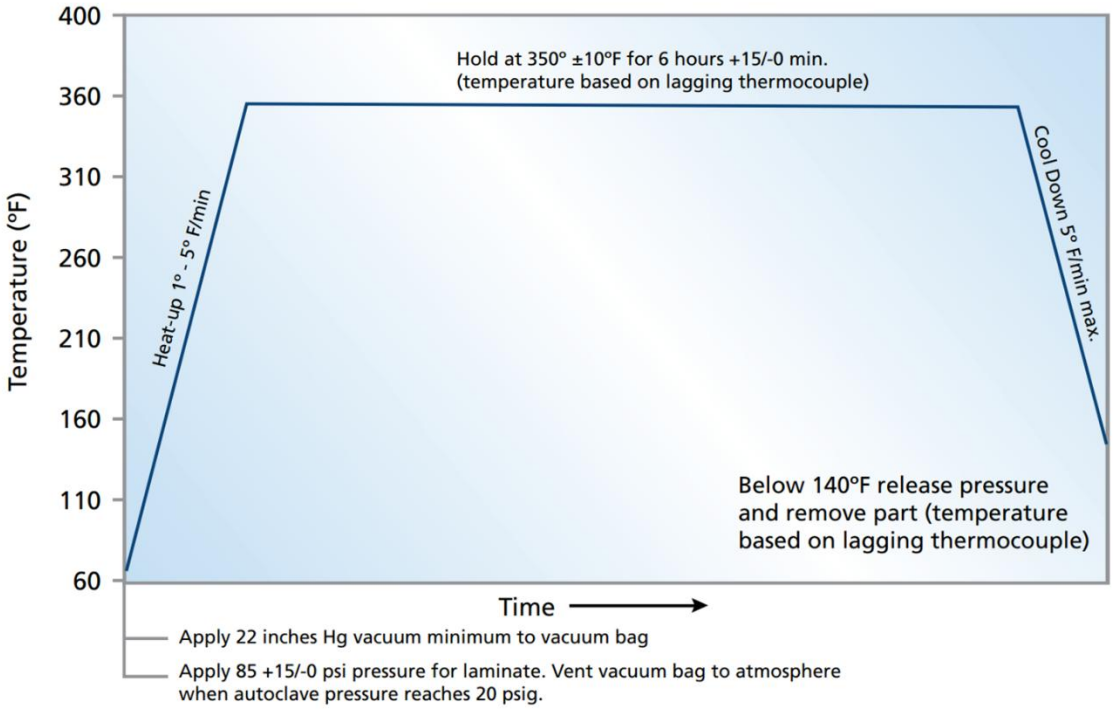

Figure 3.4 Cure schedule used to fabricate composite laminates for Half-Open I test [41].

3.3. Specimen Manufacturing

The final stage of specimen manufacturing involves cutting the cured laminates into individual test pieces. An MK Diamond Products MK-101 wet tile saw is used to achieve precise cuts. Prior to cutting, Garolite G-10 fiberglass (GFRP) sheets are attached to the top and bottom edges on both sides of each laminate, as shown in Figure 3.5a. These GFRP tabs are bonded to the laminate using JB Weld two-part epoxy, which requires approximately 12–15 hours to cure. Each test specimen is prepared to the dimensions specified in Table 2.3—270 mm × 25 mm × 1.3 mm—with GFRP tabs measuring 45 ± 5 mm in length attached at both ends. This preparation ensures that all

specimens are uniform and suitable for Half-Open I fracture testing. The test specimen is displayed in Figure 3.6.

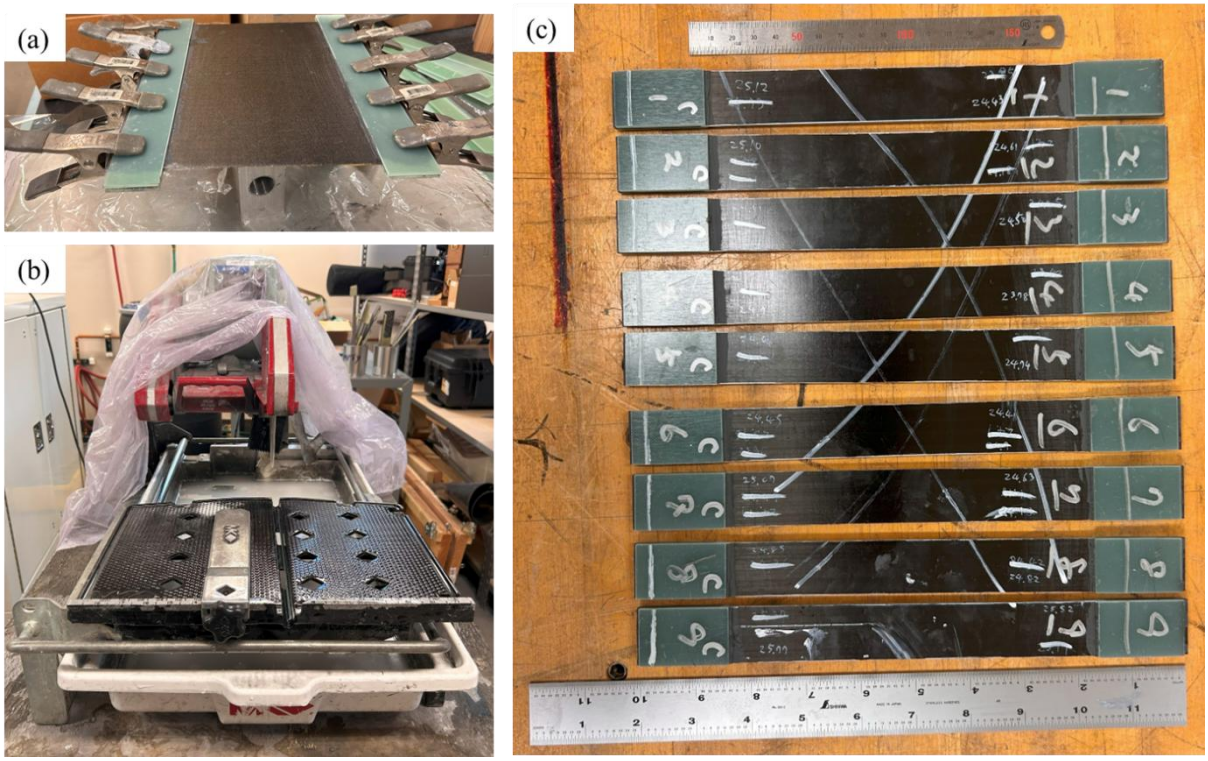

Figure 3.5 (a) GFRP attached on cured composite laminate. (b) Saw used to cut the laminates into required specimens. (c) Test specimens.

3.4. Insert Tabs

For the tabs listed in Table 2.4, all were fabricated from the same GFRP material used for the clamping tabs. The tab dimensions were identical to those of the clamping tabs, 45 ± 5 mm × 25 mm, while the thickness varied according to the required specification. The basic tab, designated 2p4, had a thickness of 2.4 mm and served as the base for manufacturing all other tab types. The 3p2 tabs, 3.2 mm thick, were fabricated by combining a 2p4 tab with a 0.8 mm thick GFRP tab. The 4p15 tabs were produced by combining a 2p4 tab with a 1.75 mm tab, while the 4p8 tabs were made by bonding two 2p4 tabs together. These four tabs are shown in Figure 3.7. Similarly, the

2p8, 4p55, 3p6, and 5p2 tabs were fabricated by adding an additional 0.4 mm thickness to the required base tab configuration.

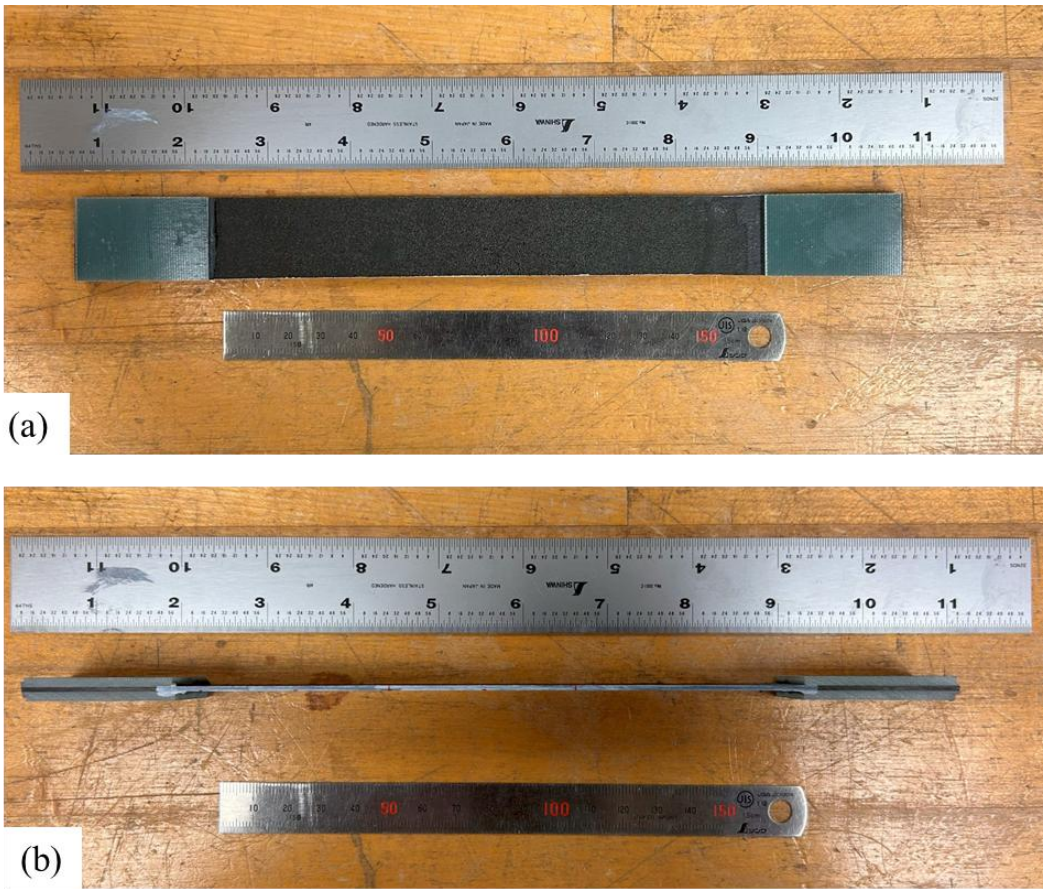

Figure 3.6 Test Specimen (a) Top View. (b) Side View.

All combining tabs were produced by cutting and machining GFRP sheets to the required dimensions, then bonding them using Gorilla® Super Glue. Prior to bonding, the surfaces of all tabs were sanded on all sides to promote strong adhesion, ensuring that the tabs did not slide or separate during any testing.

3.5. Mechanical Test Fixtures

The Half-Open I specimen is relatively straightforward in design, requiring only standard tensile testing equipment. The specimen is fabricated and directly mounted into a tensile loading system

for testing; therefore, no special fixtures needed to be manufactured, nor were any modifications to the existing load frame grips required. Testing was conducted using an Instron 5585H load frame equipped with a 250 kN capacity load cell, which can capture the ultimate tensile strength of IM7/977-3 composite material , that is, ~2909 MPa, as reported by Clay et al. This ensured that the testing system could accommodate the full load without risk of overloading the machine or compromising data quality. The fixtures used for clamping and loading the specimens are shown in Figure 3.8.

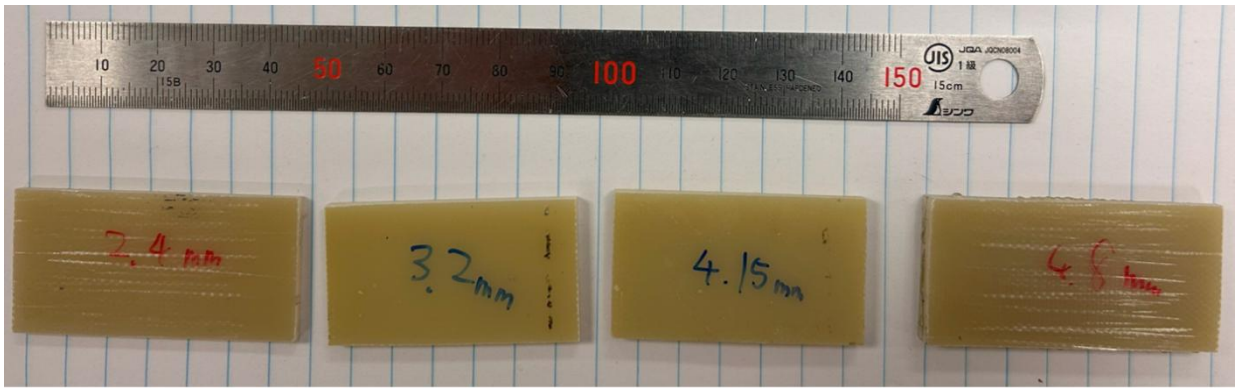

(a) (b) (c) (d)

Figure 3.7 Insert Tabs with thickness, (a) 2.4 mm (b) 3.2 mm, (c) 4.15 mm and (d) 4.8 mm.

3.6. Experimental Testing

A total of six laminates were fabricated, of which the first two served as trial specimens for the Half-Open I test. These trial runs were conducted to evaluate the supporting setup, verify the testing procedure, and ensure that the test progressed as intended. The remaining four laminates

Figure 3.8 Load frame fixtures, (left) and specimen inserted inside fixture (right).

were used for obtaining the actual Half-Open I results presented in Chapter 4. These four laminates are designated as Laminate A, Laminate B, Laminate C, and Laminate D. A total of 36 test specimens are manufactured from the four laminates, 9 from each laminate, out of which 32 were tested, leaving 4 as safety specimens. Laminates A and B were laid up and cured together, while Laminates C and D were laid up and cured together in a separate batch. The same insert tabs, as described earlier, were used for all specimens. Laminate A and Laminate D used insert tabs 2p4, 3p2, 4p15, and 4p8, while Laminate C and Laminate D used insert tabs 2p8, 3p6, 4p55, and 5p2.

For Laminate C, tab 2p1, which has thickness 2.1 mm, was used instead of 5p2. In each laminate, two specimens were tested for each of the four respective tab inserts.

3.6.1. Initial Testing

The design presented in Chapter 2 represents the first and entirely novel attempt to capture the combined effects of crack propagation and crack-parallel tension in a composite material. As anticipated, these initial trials proved challenging to interpret and can be considered unsuccessful. To achieve a successful Half-Open I test and obtain usable experimental data, two key modifications to both the testing procedure and specimen design, based on the initial configuration shown in Figure 2.11, were necessary. The following section details these procedural updates and the specific failure modes that prompted their implementation.

The initial test procedure was carried out in a straightforward manner under tensile loading. The specimen was mounted such that the end without a crack seam was clamped in the lower fixture, while the end containing the crack seam had a tab manually inserted into it. This tab was then gripped by the upper, moving fixture of the load frame, which applied an upward displacement. The loading configuration generated a global tensile load in the specimen. Additionally, due to the bending moment induced at the crack seam by the tab insertion, crack propagation was initiated.

To monitor and document the strain localization, crack initiation, and crack growth, a speckle-patterned paper was affixed to the specimen surface facing the camera for Digital Image Correlation (DIC) analysis. This was done to obtain the full-field strain mapping throughout the test. Tabs with thicknesses of 0.8 mm, 1.6 mm, and 2.4 mm were used during the initial trials to evaluate the influence of tab geometry on the bending moment, crack initiation behavior, and overall fracture progression.

From the results, it was observed that the speckle-patterned paper either failed to remain attached to the specimen surface or did not imprint effectively. In multiple samples, crack propagation was confirmed in the specimen; however, the associated deformation was not

transferred to the speckle-patterned paper. As a result, the camera was unable to capture the required fracture mechanism and propagation behavior.

Furthermore, due to the small specimen thickness of 1.3 mm, even in cases where the paper remained intact, Digital Image Correlation analysis proved challenging. The very small speckle features were difficult to resolve, as the camera had to be positioned and focused to capture the entire specimen length. This broader field of view compromised the resolution, making it difficult to clearly capture the speckle pattern. To overcome this, the camera would have needed to be focused on a specific region of interest rather than the full length, which was not feasible for this test configuration. Manual application of the speckle pattern, through painting or spraying, was also challenging due to the thin geometry, further reducing pattern quality. In addition, because the

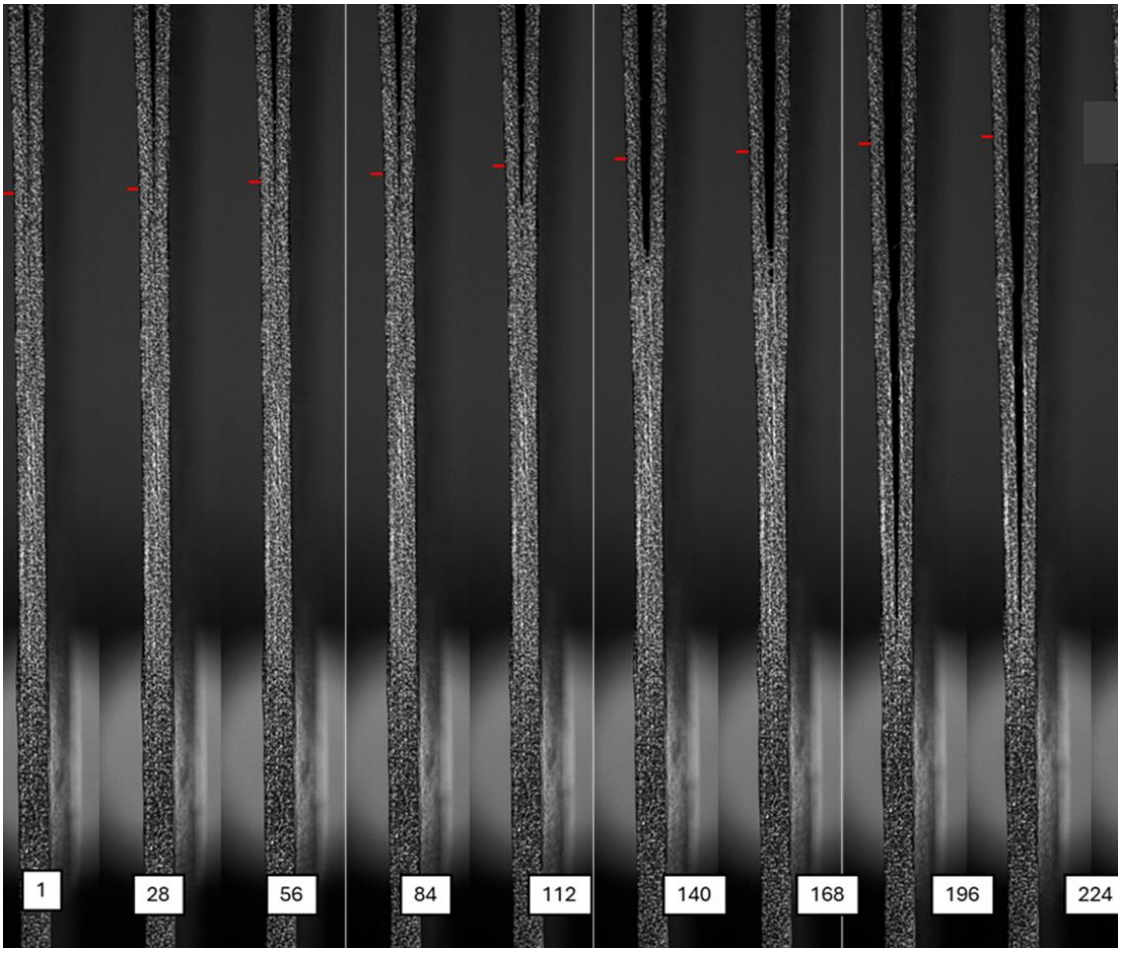

Figure 3.9 Initial test crack propagation capture. The red mark indicates the initial crack length, and the displayed number indicates the test time in (s).

camera needed to focus across the entire length of the specimen, even well-applied speckle patterns appeared poorly contrasted, making the surface appear dark, even when illuminated. The crack propagation captured under these conditions is shown in Figure 3.9.

The inserted tabs did not generate sufficient bending moment to initiate crack propagation, except for the 2.4 mm thick tab, where crack propagation occurred after a certain load was reached. Tabs with thicknesses of 0.8 mm and 1.6 mm were inadequate, as no crack propagation was observed; the specimens behaved essentially under pure tensile loading, similar to the behavior observed in the Open-I test. This highlighted that a minimum tab thickness is required to produce the initial bending moment necessary for crack opening and subsequent propagation in the Half-Open I configuration.

In the second set of tests, the initial crack seam length was significantly reduced, placing it very close to the clamping region. This adjustment was done so that the 1.6 mm thick tab can generate sufficient bending moment for crack initiation. Instead of using speckle pattern paper, the specimen surface was painted white, with markings placed at one-inch intervals to facilitate accurate crack length measurements regardless of magnification during observation. The results showed that the white surface improved the visual tracking of crack propagation, and the markers enabled precise measurement of the crack length.

However, as discussed in Section 2.3.2 of Chapter 2, the reduced initial crack length also caused pre-cracks to form during tab insertion, leading to non-loaded crack propagation before the test began. Consequently, the measured fracture energy at the start of loading appeared higher than zero. This early fracture behavior is attributed to a potential increase in the fracture process zone length, likely caused by fiber bridging initiated during tab insertion. Despite these pre-cracks, the methodology provided better visualization and measurement of crack propagation for the Half-Open I test.

3.6.2. Test Procedure

The Half-Open I test generally follows the guidelines of ASTM D3039 for composite tensile testing, ensuring consistency with standard procedures commonly used in the academic and

research community. However, as discussed in Chapter 2 regarding the specimen design, the unique and novel nature of the Half-Open I geometry introduces several scenarios where standard test specifications do not provide sufficient guidance. These deviations arise from the need to generate crack parallel tension and control crack propagation in a negative geometry, conditions not typically addressed by conventional tensile testing standards. Consequently, certain aspects of the test procedure, specimen preparation, and measurement methods had to be adapted to capture the intended fracture behavior accurately while maintaining consistency with ASTM-based methodologies.

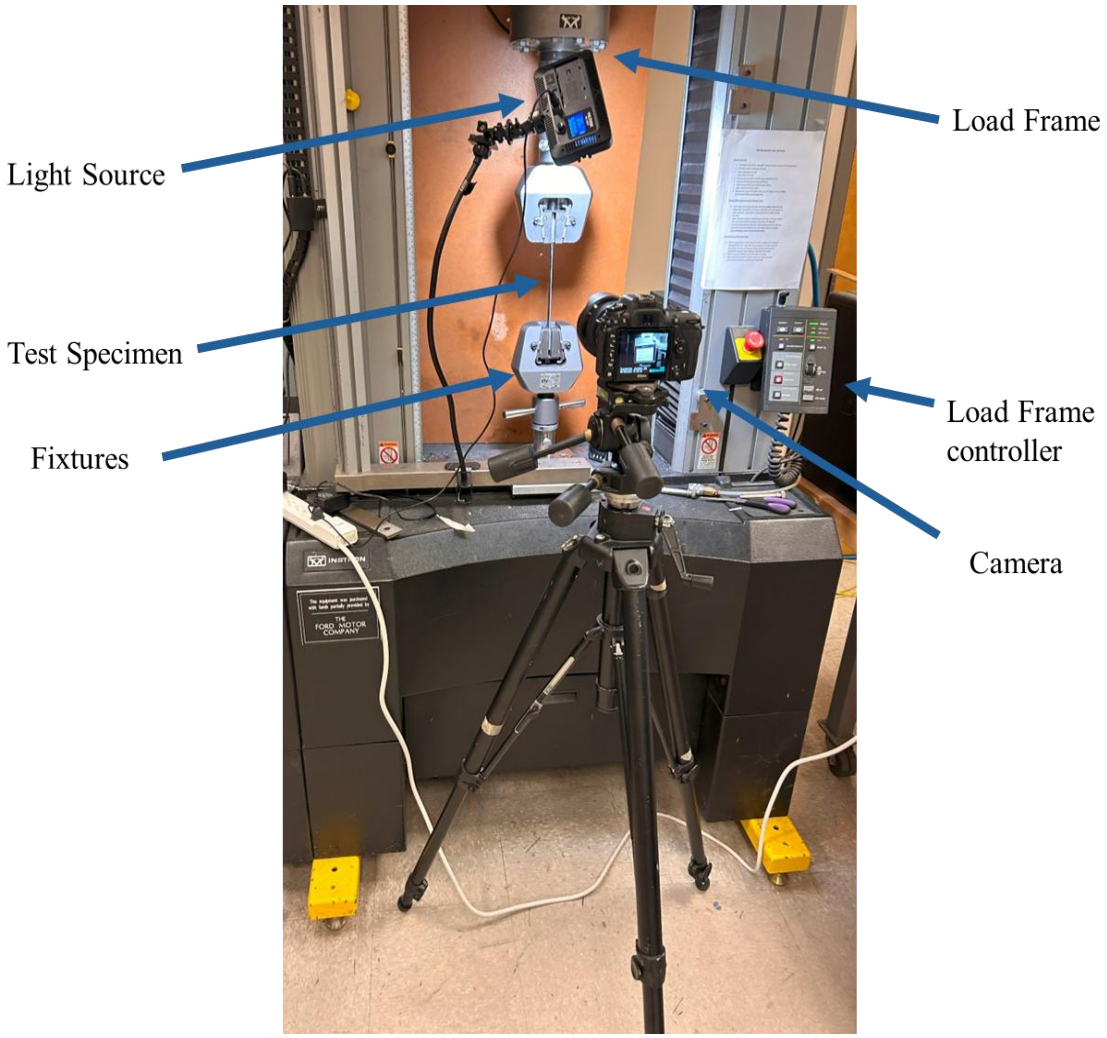

Figure 3.10 Experimental setup used to acquire the Half-Open I test data.

Following the trial testing discussed in Section 3.6.1, the standard procedure for the Half-Open I test is as follows:

1. Manufacture and obtain the test specimen from Table 2.3, record its actual dimensions, and assign a unique identifier. For example, Laminate-A_Sample-1_2p4, indicating Laminate A, specimen 1, tab ID 2p4.
2. Manually insert the tab appropriate tab in the crack seam without any crack propagation and install the specimen into the fixture as shown in Figure 3.8, checking all dimensions with calipers and a digital level. Position the specimen at the center of the fixture clamps and adjust as needed.
3. Illuminate the specimen surface with a bright external light source to ensure high-quality crack propagation imaging.
4. Focus a high-resolution camera on the crack tip, capturing the full specimen surface length. Set the camera to record at 1 frame per second
5. Zero the top fixture extension and ensure the load is near zero before load-zeroing in the workstation.
6. Start the camera capture and begin a constant displacement test at 1.5 mm/min. Start the test after the first click of the camera so as to capture accurate synchronized data with load frame.
7. Observe for 1 minute. If no crack propagation occurs, check the setup; otherwise, allow the test to continue until failure or just before the measured peak load to preserve the specimen.
8. After the testing, label all resulting pieces with their unique identifiers and store for future surface examination.
9. Download and save the force-displacement data with the corresponding specimen identifier.
10. End the test.

Chapter – 4 Results and Analysis

4.1. Results

The output from the load frame for the Half-Open I test consists of a three-column matrix containing time, displacement, and force values, recorded every 0.1 seconds by a transducer. Although fracture energy is often calculated from the area under the stress–displacement curve using Equation 4.1 [42]. Technically, this approach is applicable in the present case but not suitable for two main reasons. First, the apparent load reduction due to the less stiffness induced by the crack propagation is required. Second, due to the presence of a non-negligible FPZ, the relatively small specimen size can lead to pronounced non-linear behavior. Furthermore, as previously discussed, Bažant's size effect law cannot be reliably applied here, since it is formulated for positive geometries and does not adequately account for the specific fracture behavior observed in negative geometries. Thus, other methods are required, such as the Finite Element Analysis (FEA) or analytical solution relating the load to ERR.

$$G_f = \int_{\delta=0}^{\delta=total\ failure} \sigma(\delta) d\delta \tag{4.1}$$

Following the previously defined test procedure, the Half-Open I test was performed on four laminates: A, B, C, and D, using a total of nine tab inserts, as listed in Table 2.4. As described in Section 3.6, each tab type was used in two specimens for the respective four tabs assigned to each laminate. Of these two, one specimen was loaded to complete failure, while the other was stopped near the failure load, just before full fracture, to preserve it for fracture surface examination. Each test lasted between 4-5 minutes.

A combined force–displacement plot for Laminate A with all four of its tab inserts is shown in Figure 4.1. Notably, there is no distinct peak load; the maximum load corresponds directly to the failure point, reflecting the behavior characteristic of negative geometry. Specimens exhibiting a purely linear response without subsequent failure were those intentionally stopped just before the maximum load, determined from the previous specimen's failure load.

It can be observed that as the inserted tab thickness increases, the displacement at failure decreases. This trend is attributed to the greater initial bending moment introduced by thicker tabs,

leading to earlier failure at lower strain levels. Furthermore, the apparent stress at final failure is lower than the tensile strength of the unidirectional IM7/977-3 laminate. This reduction arises because the total stress includes contributions from both axial loading and bending stresses generated by the inserted tab, with the bending effect increasing alongside tab thickness.

In contrast to the load–displacement curves typical of positive geometries, the curves here show no noticeable intermediate load drops; failure occurs abruptly at the end, driven primarily by fiber breakage. This highlights the distinct fracture mechanics of negative geometries, where gradual load reduction stages are absent, and instability manifests only at the point of catastrophic failure.

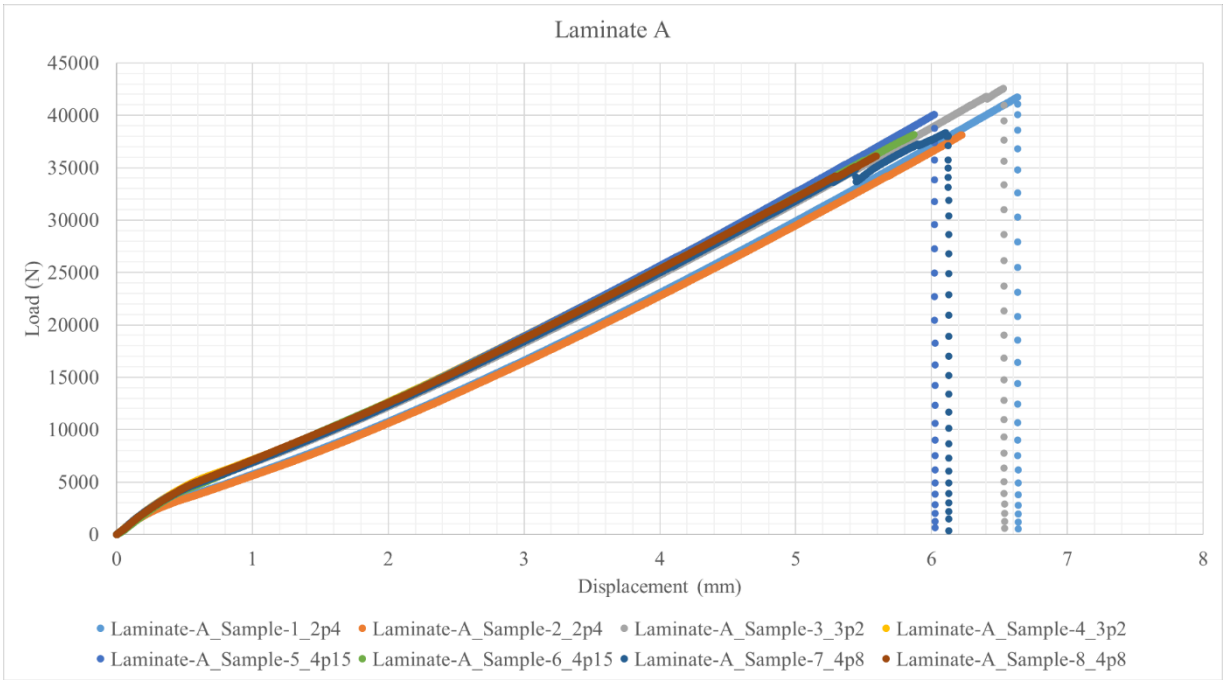

Figure 4.1 Laminate-A load-displacement plot.

Insert Tab ID	2p4	3p2	4p15	4p8
Maximum Load (N)	41739.8	42559.1	40082.07	38327.88
Slope (at 20 kN) kN/mm	6.72445	6.06122	6.76186	7.19677

Table 4.1 Laminate-A Maximum load and plot slopes at each failure achieved insert tab specimens.

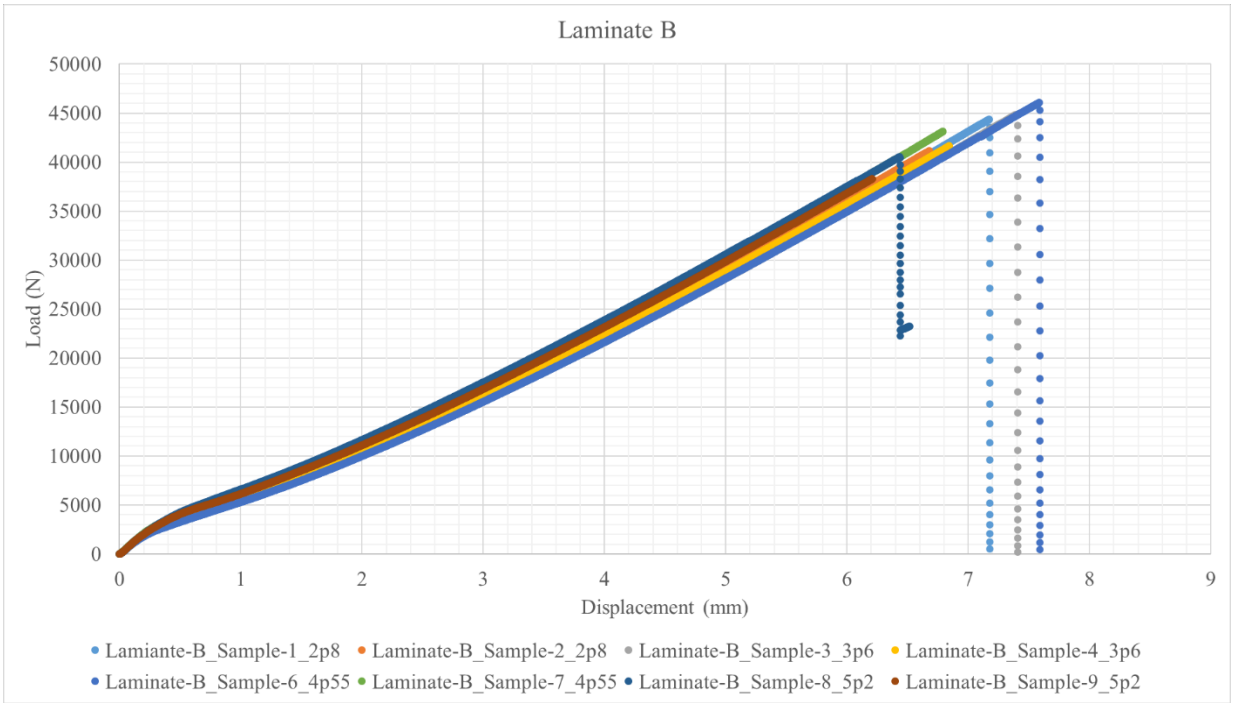

Figure 4.2 Laminate-B load-displacement plot.

Insert Tab ID	2p8	3p6	4p55	5p2
Maximum Load (N)	44359.4	44848.25	46062.32	40538.04
Slope (at 20 kN) kN/mm	6.15353	5.61455	4.63539	5.52511

Table 4.2 Laminate-B Maximum load and plot slopes at each failure achieved insert tab specimens.

The force–displacement curves for Laminates B, C, and D are presented in Figure 4.2, Figure 4.3, and Figure 4.4, respectively. Similar to Laminate A, the plots show that increasing tab thickness results in reduced displacement at failure. It is also observed that the maximum failure loads for all cases are very close to each other, as summarized in Table 4.1, Table 4.2, Table 4.3 and Table 4.4. The combined average maximum load for all tab inserts across all laminates is provided in Table 4.5.

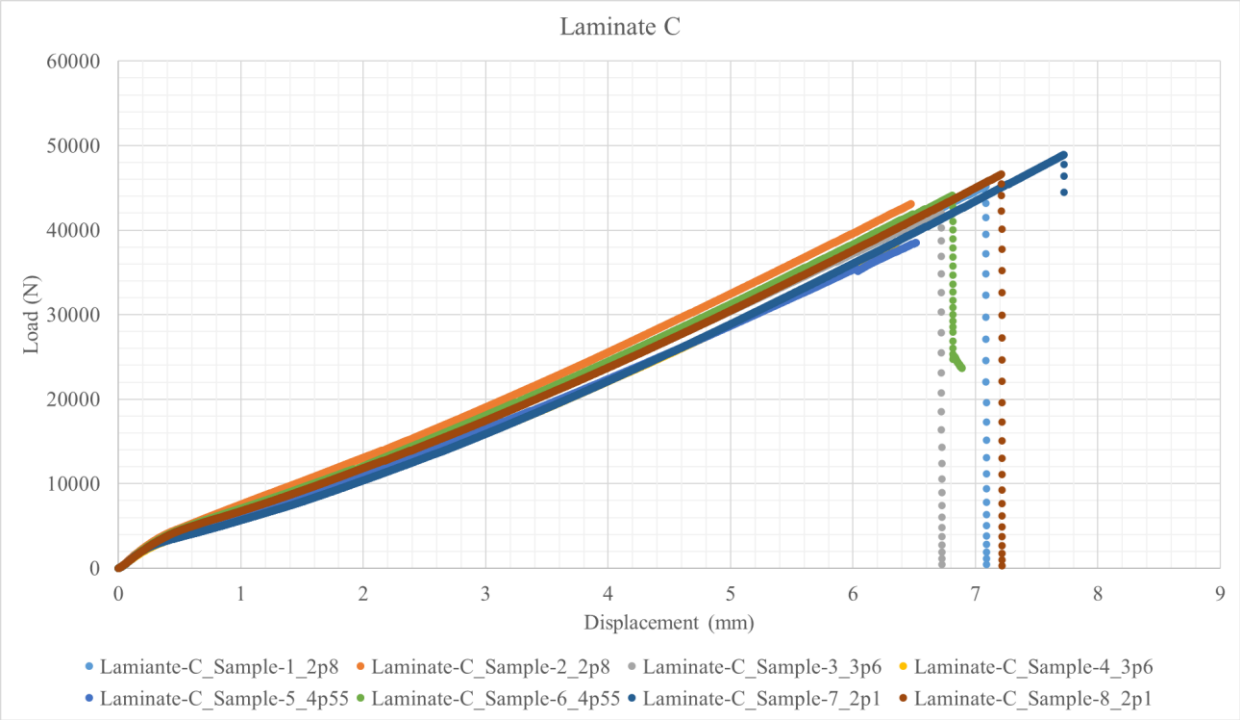

Figure 4.3 Laminate-C load-displacement plot.

Insert Tab ID	2p8	3p6	4p55	2p1
Maximum Load (N)	45220.42	42001.5	38528.96	48930.62
Slope (at 20 kN) kN/mm	5.18417	6.14497	6.01134	6.28851

Table 4.3 Laminate-C Maximum load and plot slopes at each failure achieved insert tab specimens.

The crack propagation behavior was found to vary with the thickness of the inserted tab. For lower-thickness tabs, 2p1, 2p4, and 2p8, an initial stage with no visible crack growth was observed, during which the applied load continued to increase. Measurements during this period indicated only minimal crack extension, ranging from 0.1 to 1 mm. This stage persisted until a certain load threshold was reached, after which propagation began. In these thinner-tab specimens, this second stage often initiated with an unstable crack jump, although in some cases stable crack growth occurred. Following this onset, a period of stable crack propagation dominated the response. Near the maximum load, this stable growth frequently transitioned to an unstable mode

for a brief period before complete failure occurred. This sequence delayed initiation, sudden unstable growth, and final instability was particularly characteristic of the lower-thickness tab configurations. The stable crack propagation observed in the 2p1 tab was significantly smaller compared to that in the 2p4 and 2p8 tabs, resulting in considerably less usable data. For this reason, the data from the 2p1 tab was excluded from the analysis.

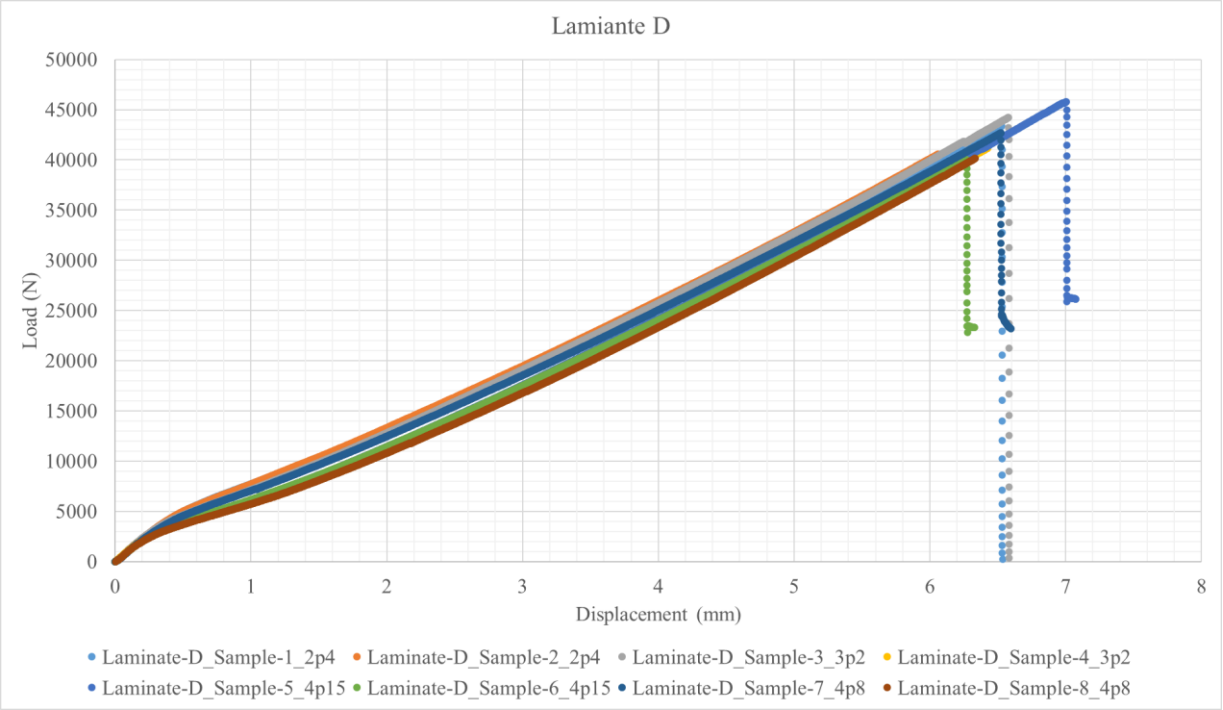

Figure 4.4 Laminate-D load-displacement plot.

Insert Tab ID	2p4	3p2	4p15	4p8
Maximum Load (N)	41739.8	42559.1	40082.07	38327.88
Slope (at 20 kN) kN/mm	6.72445	6.06122	6.76186	7.19677

Table 4.4 Laminate-D Maximum load and plot slopes at each failure achieved insert tab specimens.

In the 3p2 and 3p6 tabs, crack propagation followed a similar pattern to that of the smaller-thickness tabs, but the initial unstable phase was much shorter, and the final period of instability

was rarely observed. The total extent of crack propagation also increased with tab thickness. With thicker tabs, such as 4p15 and 4p55, the initial unstable jump was seldom observed, and cracks propagated in a stable manner within a few seconds. At the final stage, there was often no unstable period before failure. For the thickest tabs, 4p8 and 5p2, neither an initial nor a final unstable phase was present; from the start of testing, the crack propagated stably until failure. The 5p2 tab appeared to be at or near the critical thickness for a 50 mm crack seam, requiring careful insertion to avoid pre-load crack propagation. In all tests, cracks did not extend into the clamped section. In specimens where cracks propagated close to the clamp, failure occurred. Slippage between the inserted tabs and the composite surface, as well as between the clamping tabs and the fixtures, was not observed in any of the test cases. The crack propagation sequence for Laminate-A and case of 4.8 mm thickness insert tab is shown in Figure 4.5.

Tab thickness (mm)	**Quantity**	**Mean of Max. Load (N)**	**Coefficient of Variation**
2.1	1	48930.61	0
2.4	2	42562.09	0.01931
2.8	2	44789.90	0.00961
3.2	2	43392.98	0.03920
3.6	2	43424.87	0.03277
4.15	2	42945.21	0.02418
4.55	2	42295.63	0.08905
4.8	2	38141.79	0.05387
5.2	1	40538.03	0
Coefficient of Variation (Max. Load)		0.06441	

Table 4.5 Combined Laminates average of maximum load for each insert tab.

4.2. Analysis

To analyze the influence of crack-parallel tension on fracture energy, an R-curve was constructed for each insert tab configuration. The analysis focused on specimens tested until complete failure. An R-curve requires the energy release rate at various crack propagation lengths, Δa. As discussed previously, the fracture energy in this test is not recommended to be calculated using conventional methods; instead, it is evaluated using Abaqus FEA. In Abaqus, the J-integral was computed for a set of increasing crack lengths, each associated with its respective load. From these results, ERR–Δa curves were generated for each insert tab specimen in each laminate type. For comparison across specimens, points corresponding to common values of crack-parallel tensile stress, normalized by the UTS, denoted by ξ, were identified. Using these points, the required R-curves were plotted to assess the influence of crack-parallel tension on fracture energy, as shown in Figure 4.6. The levels of crack-parallel tension analyzed in this study were ξ = 10%, 20%, and 30% .

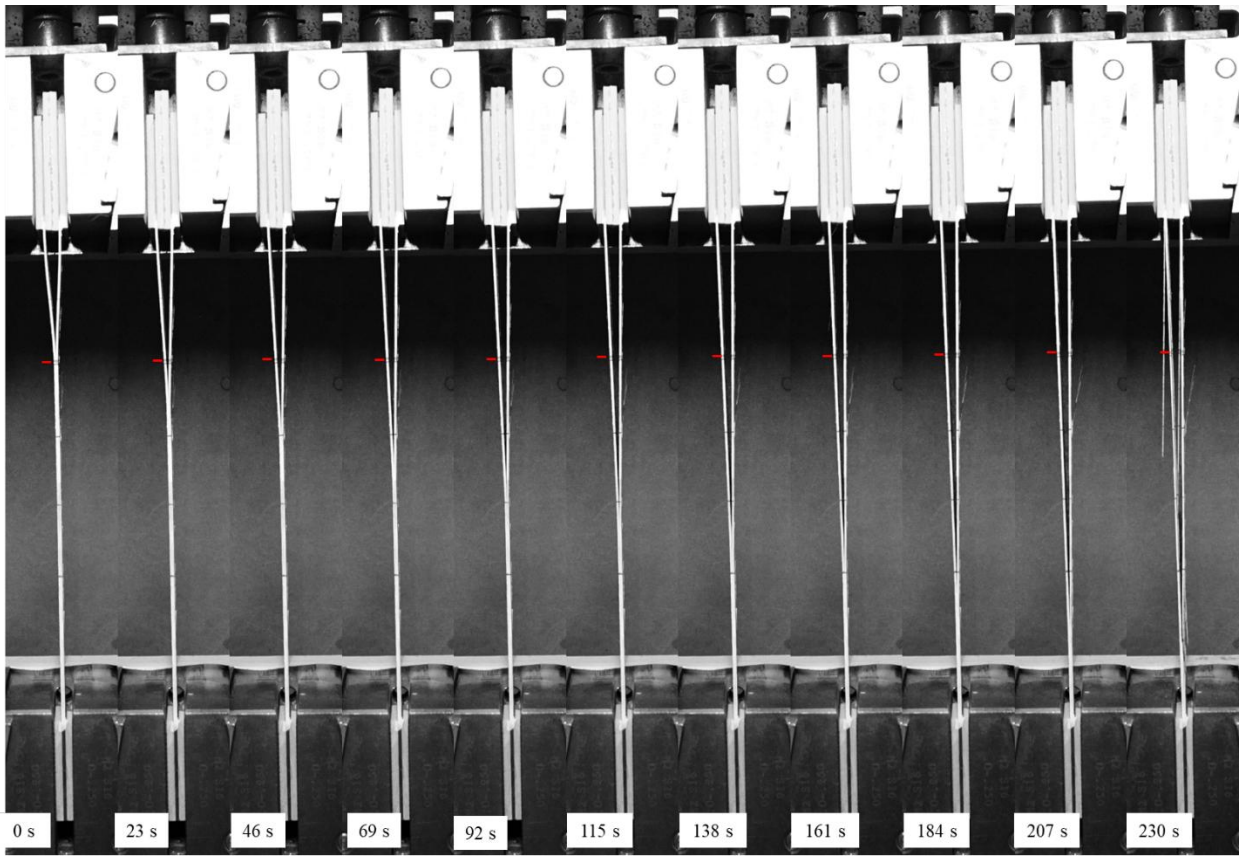

Figure 4.5 *Laminate- A_Sample-7_4p8* specimen crack propagation with snaps at every 23s. The red mark indicates the initial crack length.

The crack length was measured using ImageJ software on the one-second intervals images captured for each test. For scaling and calibration in the software, an initial crack length of 50 mm was used. For each test, a set of 10 images was selected for analysis, excluding the initial capture (0 s). The selection interval was determined based on the total number of captured images. Specifically, the total image count excluding the initial frame was divided by 10, and the greatest integer value of the result was used as the interval. For example, if 240 images were captured in total, subtracting the initial frame, 240 - 1 = 239 images. Dividing 239 by 10 yields, 239/10 = 23.9, so an interval of 23 images was chosen. This approach ensured evenly timed crack-length measurements over the duration of each test.

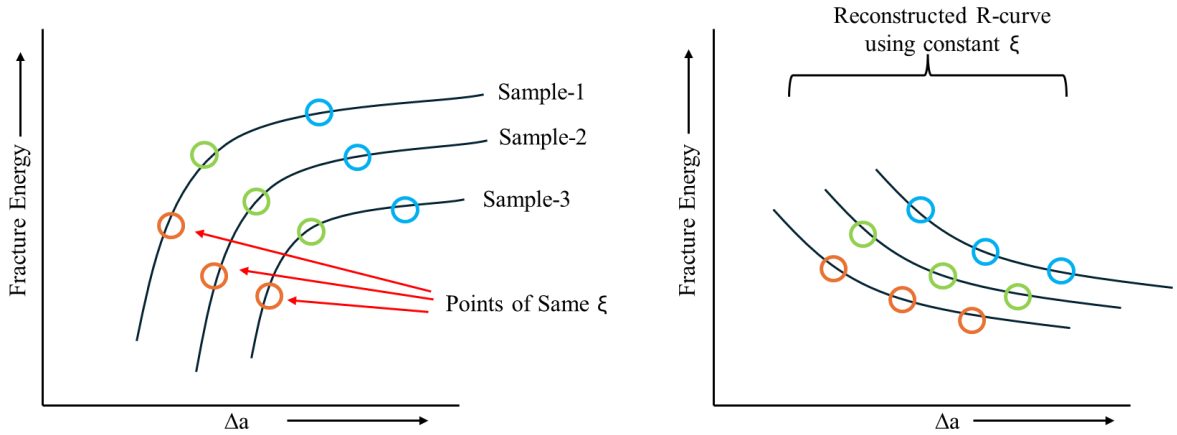

Figure 4.6 Reconstruction of (right) R-curve with constant using the through common points obtained from R-curve from Abaqus J-Integral (left).

Upon visual inspection of the fracture surfaces, regions or lines of contrast were observed, corresponding to zones of unstable and stable crack propagation. Figure 4.7 illustrates the fracture surfaces of Laminate C specimens with 2.4 mm and 4.55 mm tab inserts. The specimen with the 4.55 mm tab exhibits a longer fracture surface due to the larger bending moment, which induces higher bending stresses at the same applied load. This observation supports the influence of different crack-parallel stresses on propagation.

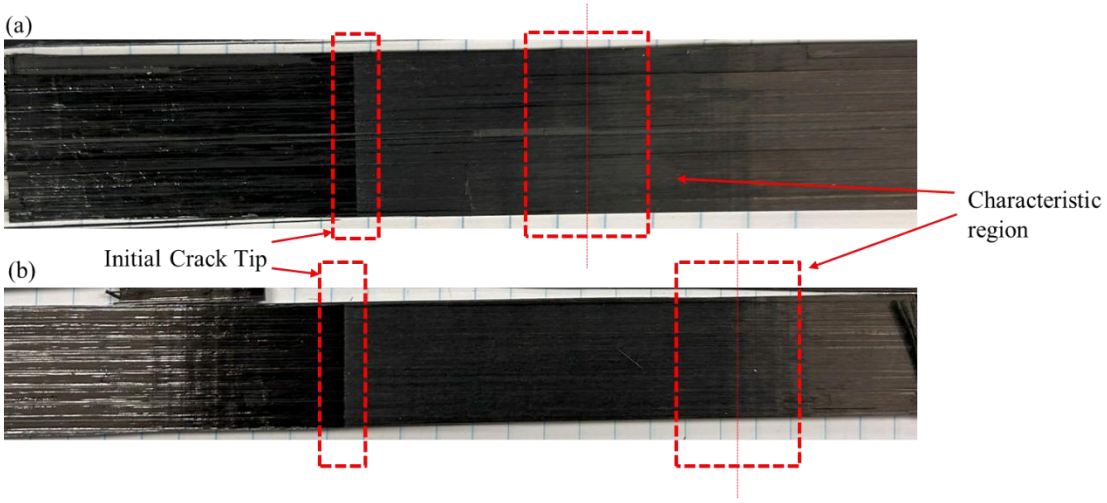

Figure 4.7 The fracture surfaces of the Half Open I test for laminate C for the cases of (a) 2.4 mm tab thickness (b) and 4.55 mm thickness. It can be seen in the characteristic region; there is change in contrast on fracture surface.

Two types of lines were identified on the fracture surfaces. The first corresponds to the crack tip: on the right side of the initial crack tip line, a distinct boundary separates a clean, shinier region representing the FEP film-inserted area, from the crack-propagated region. This line indicates the location of the crack tip during propagation. The second line, referred to as the characteristic line, appears at varying positions depending on the final failure location. It marks the point where the specimen reached the ultimate failure load, and the fracture surface exhibits brittle behavior with sudden crack jumps. Both lines together provide a clear mapping of the crack progression and the interaction between stable and unstable propagation zones under the applied bending and axial stresses.

The plots of measured crack propagation lengths for each test specimen across all laminates are shown in Figures 4.8 and 4.9. As discussed earlier, specimens with smaller thickness tabs exhibit an initial period of unstable crack propagation of approximately 0.1–1 mm, followed by a jump and subsequent stable crack growth. As the tab thickness increases, this initial unstable period shortens and eventually disappears for the larger thickness tabs, resulting in an extended period of stable crack propagation. Additionally, it is evident that increasing tab thickness also increases the rate of crack propagation, highlighting the influence of the higher bending moment induced by

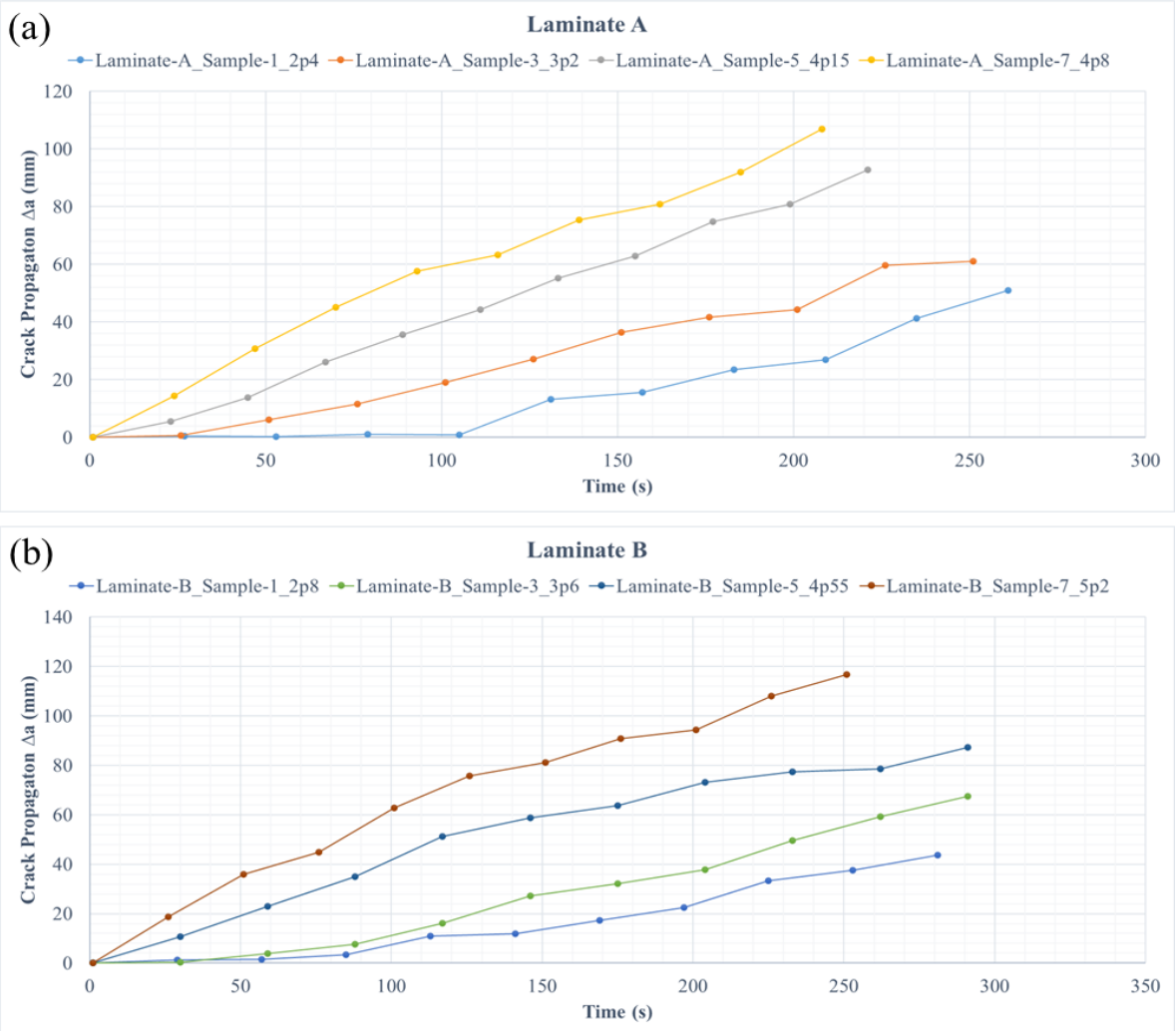

Figure 4.8 Measured crack propagated lengths with time (s) in (a) Laminate A, (b) Laminate B.

thicker tabs. These trends clearly demonstrate the relationship between tab thickness, initial bending moment, and the resulting crack propagation behavior.

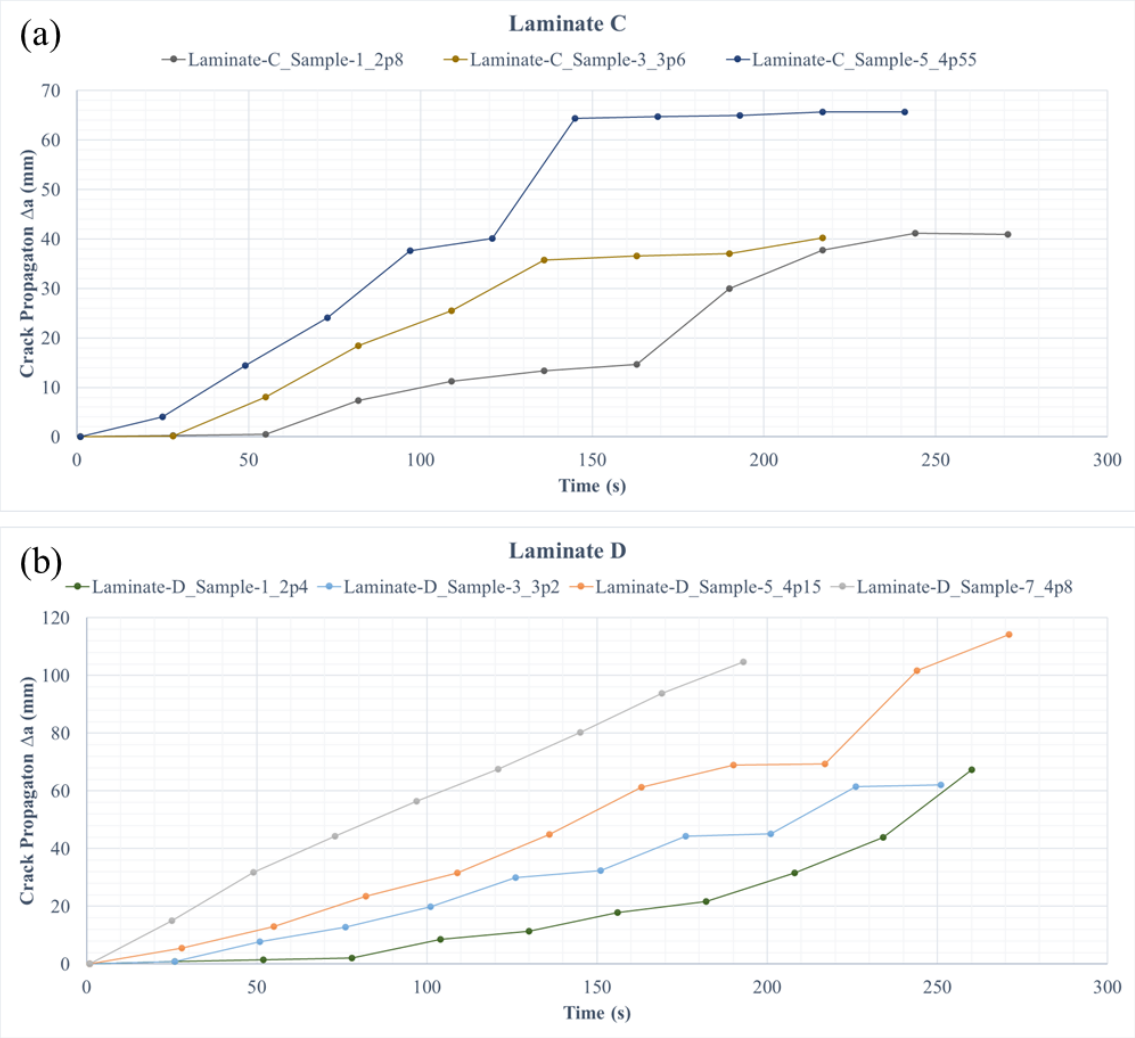

Figure 4.9 Measured crack propagated lengths with time (s) in (a) Laminate C, (b) Laminate D.

To evaluate the energy release rate (J/mm) at each measured crack propagation length, Equation (1.6) for the J-Integral is employed using finite element analysis in Abaqus. The J-Integral directly provides the energy release rate for the corresponding crack lengths and applied loads. The Abaqus model is constructed based on the Half-Open I specimen design and dimensions presented in

Figure 2.11 and Table 2.3. Material properties for IM7/977-3, as listed in Table 3.1, are assigned following the stacking sequence described in Section 3.2. The model uses CPE8 elements, and the simulation consists of two steps. The first step simulates tab insertion, wherein the two crack-front beams are displaced in opposite directions by half the thickness of the inserted tab. The second step applies pressure at the other end corresponding to the respective load measured at the given crack propagation length, divided by the specimen's cross-sectional area. The boundary conditions, crack tip assembly and the mesh applied are shown Figure 4.10.

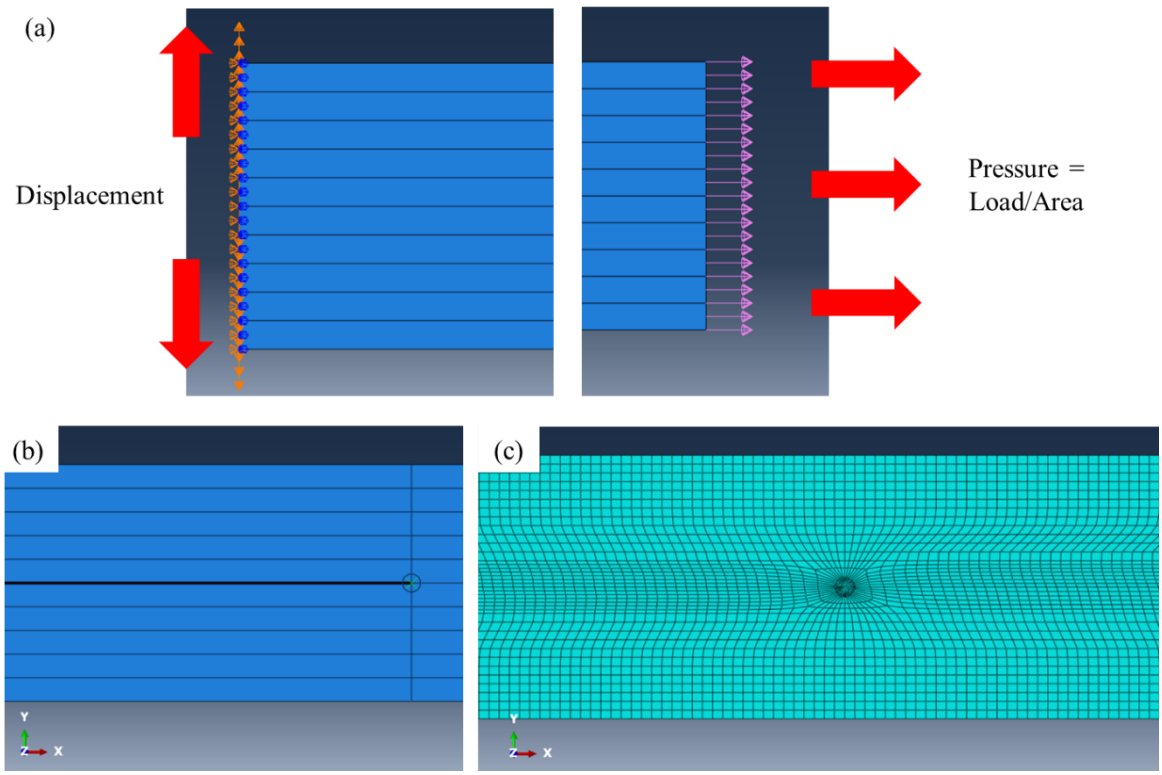

Figure 4.10 (a) Boundary Conditions (b) Crack seam and tip (c) Meshing.

The evaluated energy release rate increases with crack propagation length and eventually reaches a plateau, as shown in Figure 1.6. This trend forms the R-curve for the specimen. For all specimens tested, the R-curves converge toward a steady value, representing the fracture energy, in the range of 0.16–0.20 J/mm. This value is very close to the Mode I interlaminar fracture energy

of 0.167 J/mm reported by Chen et al [37]. Minor discrepancies and measurement noise were observed at certain points, likely due to measurement discrepancy due to image resolution limits or load measurement fluctuations, but the overall trend remains consistent, reflecting stable fracture behavior. The evaluated R-curves for each of the Laminates are shown in Figure 4.11 and Figure 4.12.

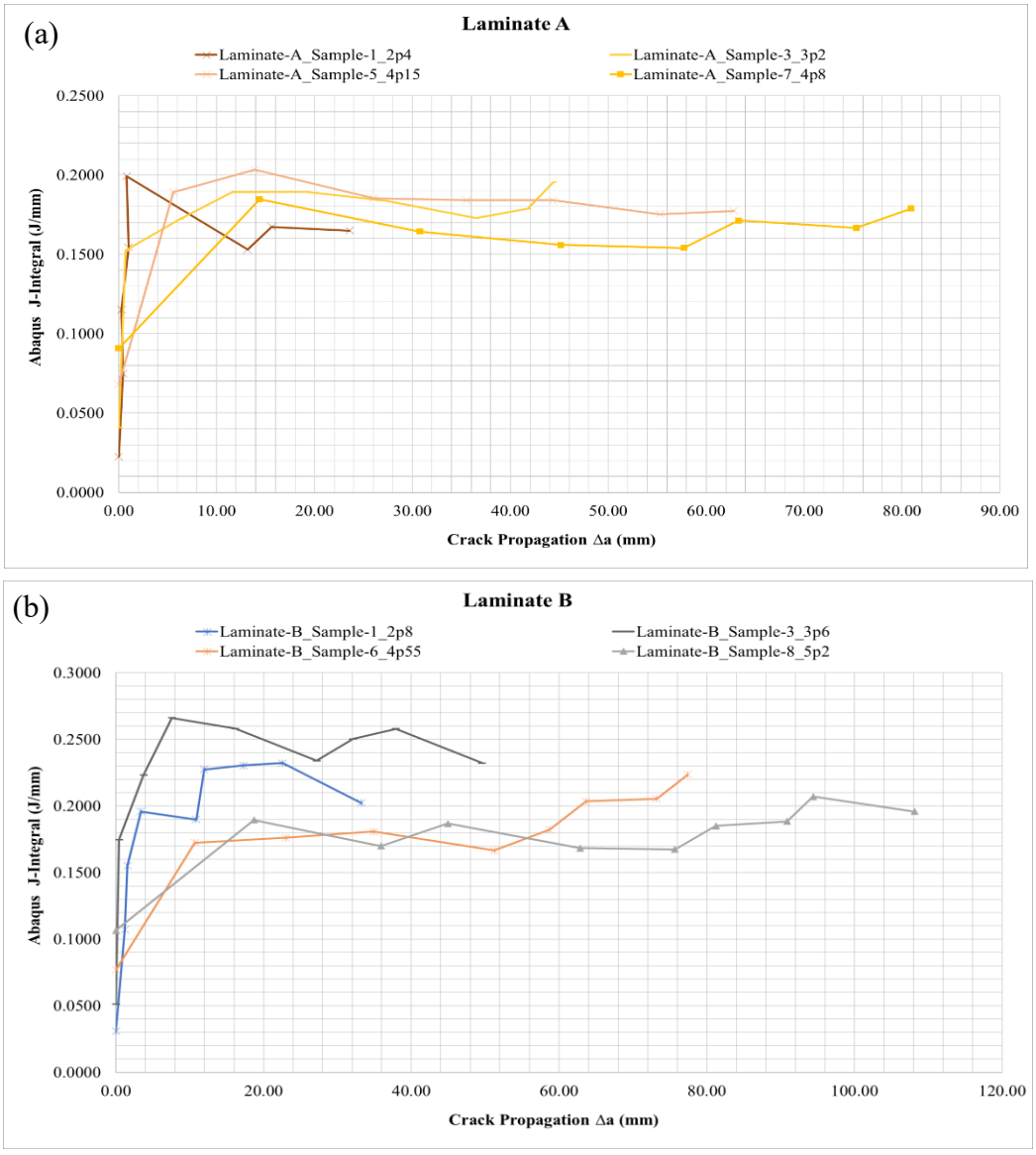

Figure 4.11 R-Curve of (a) Laminate A (b) Laminate B.

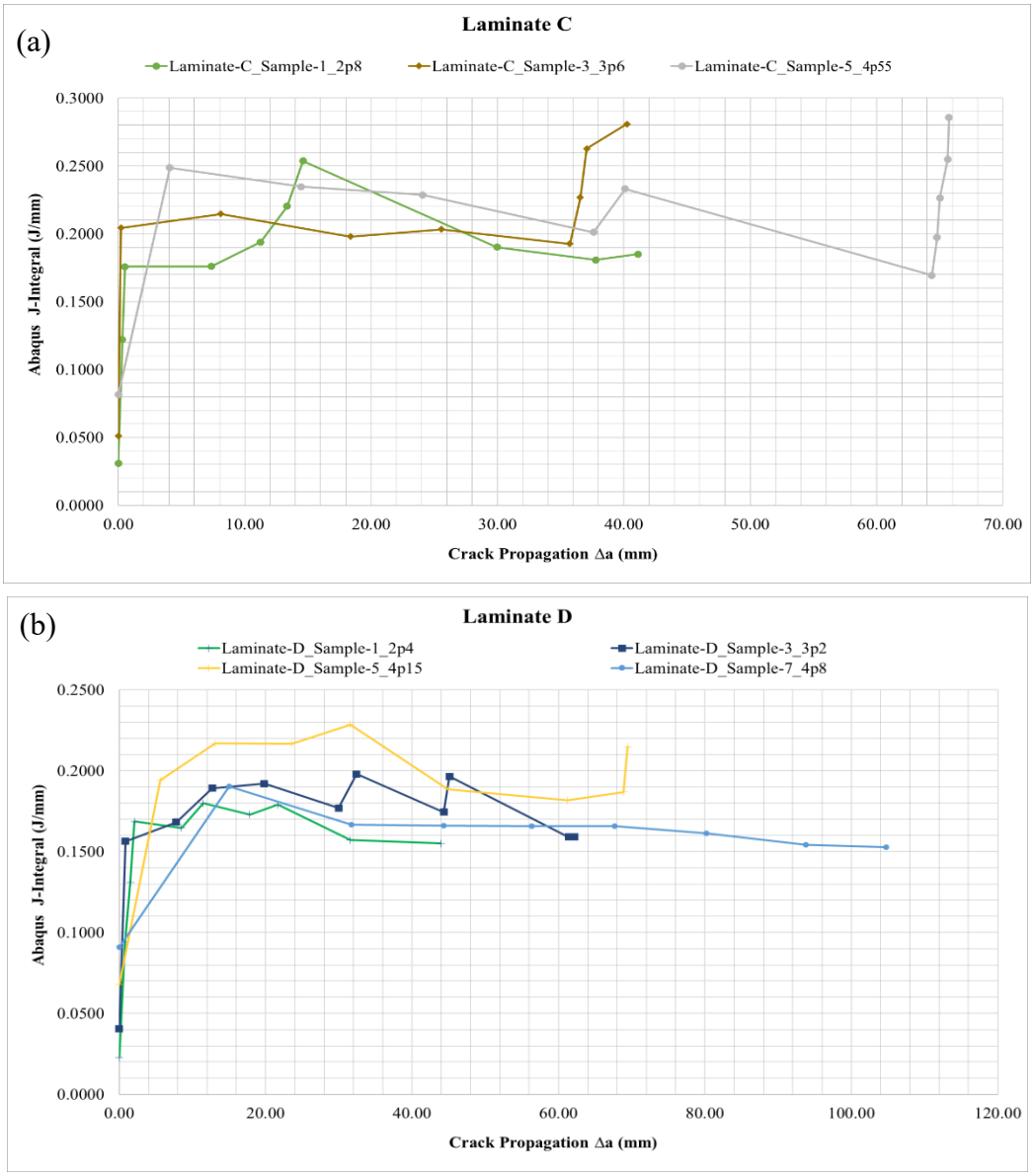

Figure 4.12 R-Curve of (a) Laminate C (b) Laminate D.

The R-curves for ξ = 10%, 20%, and 30% were reconstructed by identifying the common stress points across the different specimen, as illustrated in Figure 4.13 and Figure 4.14. This process was repeated for each laminate configuration, except for Laminate A at ξ = 30%, where usable data was unavailable. Despite the considerable noise present, the reconstructed R-curves show a consistent upward shift with increasing ξ, expected in negative geometry. Additionally, the

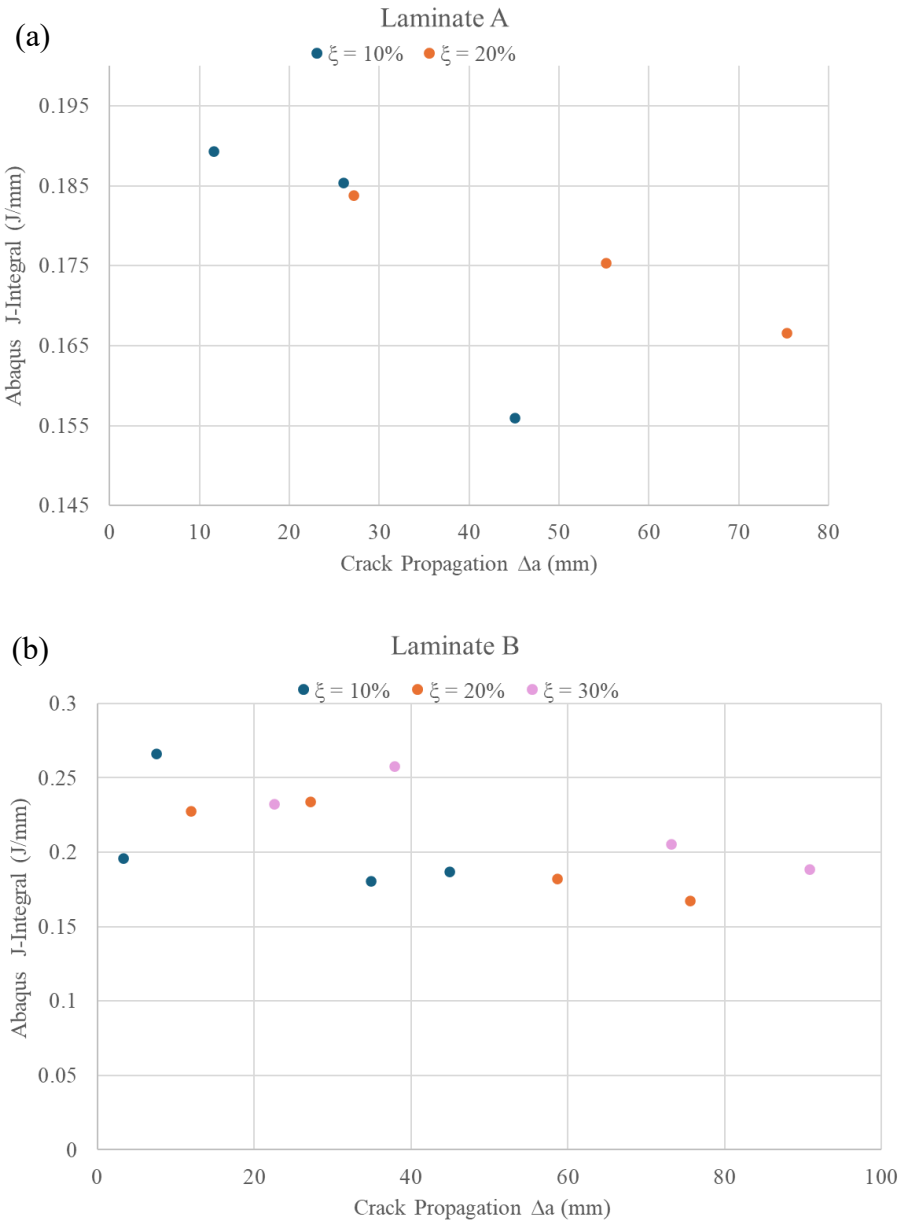

Figure 4.13 Reconstructed R-Curve for constant ξ of (a) Laminate A (b) Laminate B.

curves suggest a possible rightward shift, indicating that data at higher ξ values correspond to greater crack propagation lengths for the same energy release rate. The rightward shift reflects the increase in the crack propagated length for the same energy release rate value, indicating possibly that fracture energy increases with ξ, even though localized up-and-down fluctuations remain common across all laminates.

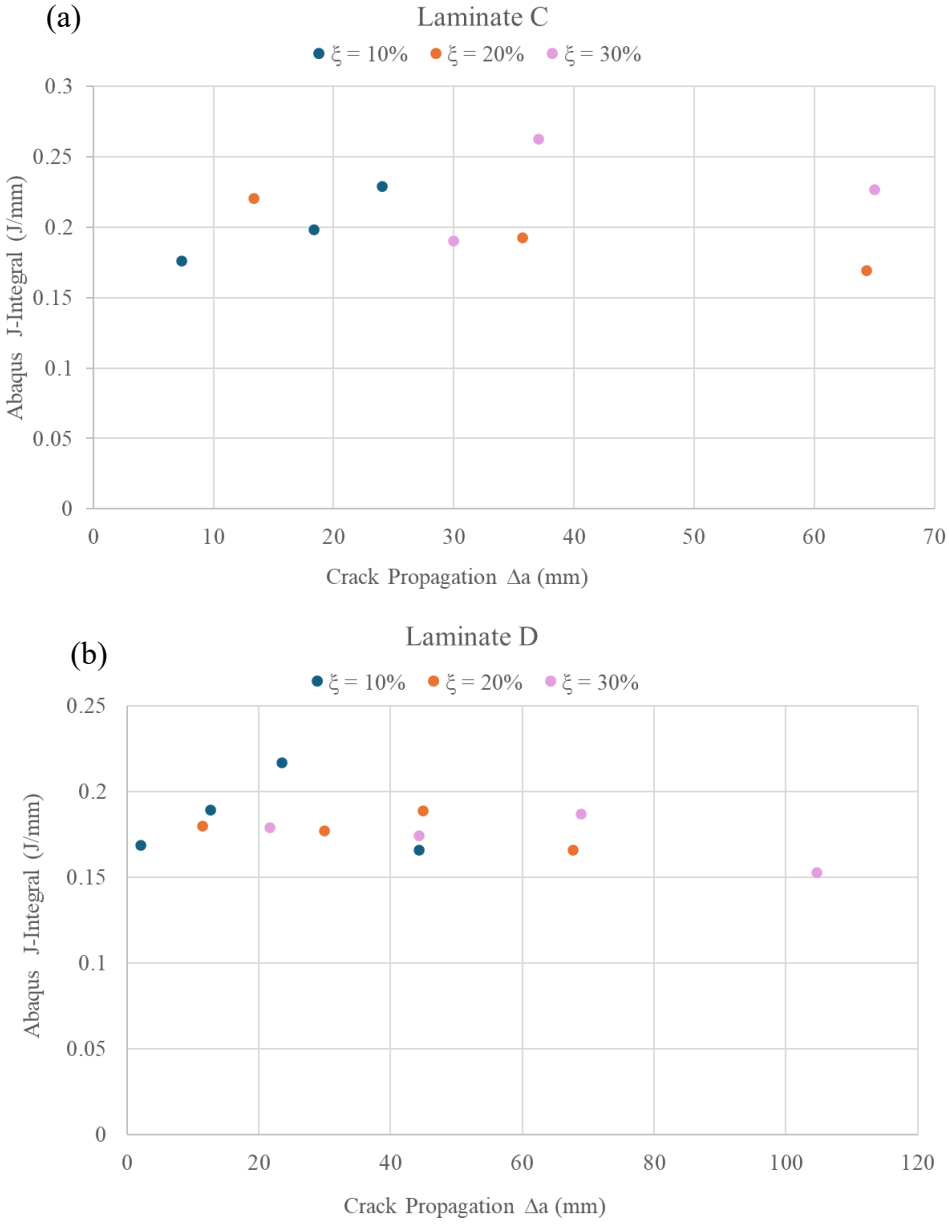

Figure 4.13 Reconstructed R-Curve for constant ξ of (a) Laminate C (b) Laminate D.

Since the reconstructed R-curves contained only three data points, they were insufficient to conclude any reliable trend. To obtain longer curves, the data points from Laminates A and B were combined, and those from Laminates C and D were combined, as these laminate sets were

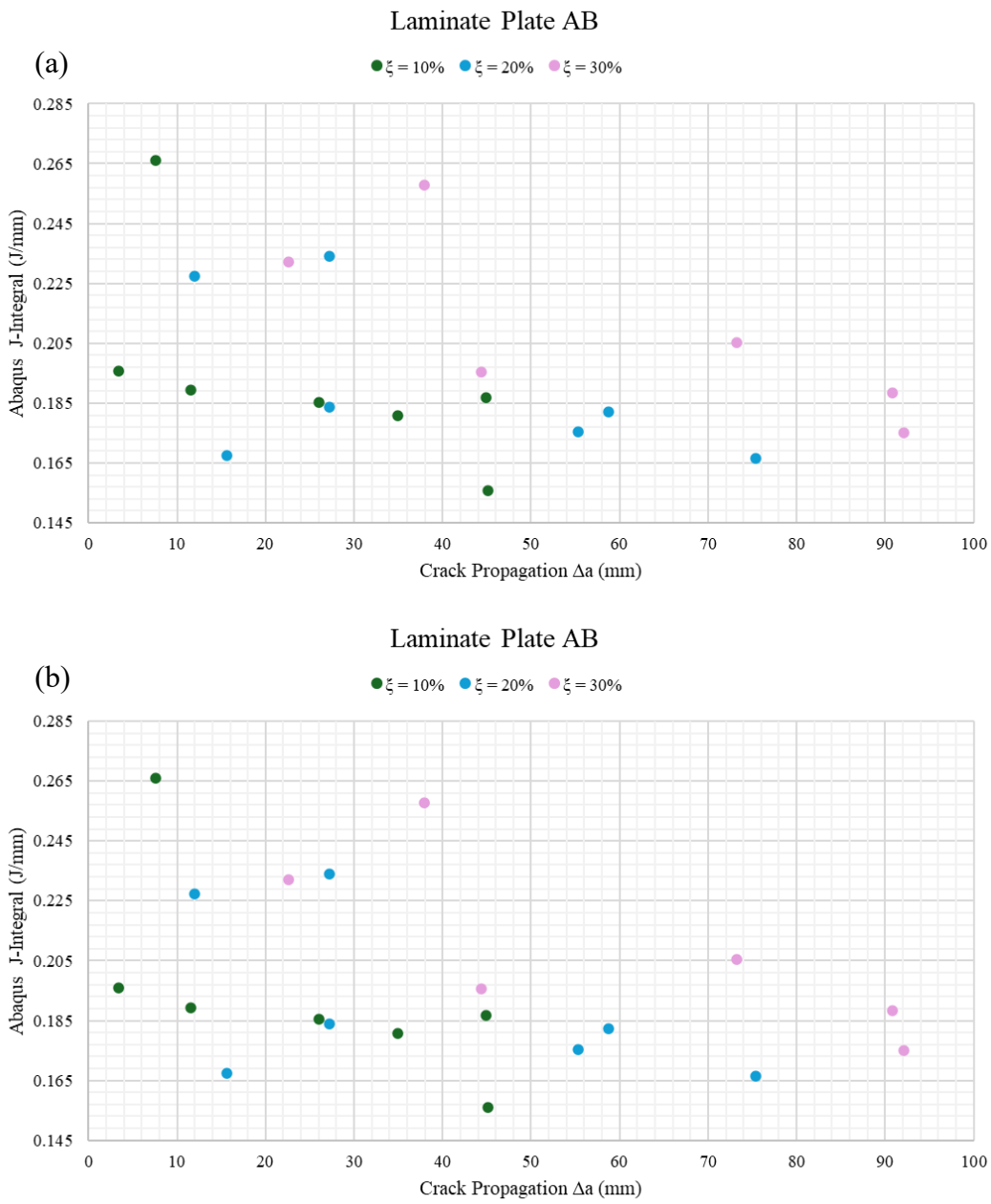

Figure 4.14 Reconstructed R-Curve for constant ξ of (a) Laminate AB (b) Laminate CD.

laid up and cured together. The reconstructed R-curves for these combined laminates provided extended datasets; however, the noise level increased, with more fluctuations visible along the curves. Despite this scatter, a noticeable rightward shift in the curves was observed as ξ increased

from 10% to 30% for both laminate combinations. This shift suggests a potential increase in fracture energy, although this remains speculative due to the high degree of scatter and the absence of a $\xi = 0\%$ baseline for direct comparison.

Chapter – 5 Conclusion

This thesis investigated the effect of crack-parallel tension on the global Mode I interlaminar fracture behavior of a carbon fiber polymer matrix composite, an area previously unexplored in composite structures, though a prior work on crack-parallel compression, the Gap test is present. To address this gap, an innovative experimental method, the Half-Open I test, was conceived, developed, and its procedures thoroughly documented for potential application to composites. The present study focused on a negative geometry configuration, where increasing crack length leads to a decrease in the stress intensity factor, promoting stable crack growth. However, due to the specific characteristics of the negative geometry and the limitations of the available data, direct estimation of fracture energy under crack-parallel tension could not be achieved. Based on these endeavors the following conclusions are made:

1. For cross-ply composites, the presence of crack-parallel tension appears to lead to a possible increase in fracture resistance. Specifically, as the crack-parallel tension is increased from ξ = 10% to 30%, the fracture energy shows an increase, as indicated by the rightward shift of the R-curves. However, due to insufficient data for ξ values between 30% and 100%, it cannot be concluded that there is a monotonic increase in fracture energy. Furthermore, the presence of considerable noise in the data means this trend should be interpreted only as an indication for the evaluated ξ range. More stable, noise-free data points are required to draw firm conclusions.
2. This apparent strengthening effect, reflected by the upward shift of the R-curve, can be explained by two interconnected factors:
    a. The Half-Open I test is a negative geometry test, which can remain in a stable crack growth regime for longer. This allows more energy to dissipate through micro-mechanisms rather than being released abruptly, leading to an apparent increase in fracture energy.
    b. At lower levels, the presence of crack-parallel tension may alter the fracture process zone (FPZ) by increasing fiber bridging, matrix deformation, or delamination roughness. These effects can raise the resistance to crack propagation, resulting in higher fracture energy

3. The apparent increase in fracture energy at lower levels of crack-parallel tension challenges the long-standing hypothesis that fracture energy is a constant material property. This observation complicates the use of fracture energy as a single-parameter descriptor of fracture behavior.
4. Though a clear trend could not be established, it was concluded that the presence of crack-parallel tension does influence the fracture energy and, in turn, the fracture process zone in composites. Composites exhibit a non-negligible FPZ that significantly affects their structural behavior in the presence of a crack or defect. This behavior is highly dependent on the stress state, meaning that the idealized line-crack assumptions underlying Linear Elastic Fracture Mechanics are unsuitable for composites. Instead, Quasi-Brittle Fracture Mechanics are required to predict the response of cracked composites or other similar quasi brittle materials.
5. Building upon the gap test on composites, the observation that crack-parallel tension can potentially increase structural strength suggests that cracks in composites may open in a non-traditional fracture mode not strictly defined by the classical Mode I, II, or III loading conditions. This behavior can only be explained by the presence of non-negligible FPZ.
6. The detailed study and experimental procedure presented here are directly applicable to composite materials. Throughout this work, the author has identified two important lessons worth sharing:
7. (1) The development process from the Open I to the Half-Open I test required approximately 2–3 weeks. This delay was primarily due to delamination limitations encountered during the Open I testing. Incorporating damage analysis in Abaqus prior to experimental testing could have highlighted potential issues with the Open I specimens, thereby saving time and resources by preventing the fabrication and testing of specimens that would have yielded unreliable results
8. (2) It is critical that cracks in the specimens do not propagate under unloaded conditions, as this leads to inaccurate experimental data. In the Half-Open I test, the initial crack seam must be sufficiently long to ensure that tab insertion does not induce pre-loading crack propagation. Maintaining an appropriate crack length guarantees that the subsequent fracture and R-curve measurements reflect the intended experimental conditions

Remarks

The experiments conducted highlight the significance of crack-parallel tension, particularly due to the observed potential strengthening effect, which could either enhance performance or pose serious risks if ignored in practical applications. However, the results are too limited to draw definitive conclusions or justify immediate revisions to composite fracture theory or engineering practices. Further investigation is needed, including different layup sequences, additional ξ values, alternative material systems, and varied geometries. Moreover, the individual effects of in-plane and out-of-planes crack shear, as well as behavior under fatigue and mixed-mode loading, must be systematically studied. Comprehensive understanding of these phenomena will require substantial resources, dedicated research efforts, and careful experimental design to fully characterize the behaviors observed in this study.

Bibliography

[1] M. E. Tuttle, *Structural Analysis of Polymeric Composite Materials*. Boca Raton: CRC Press, 2003. doi: 10.1201/9780203913314.

[2] S. Rana and R. Fangueiro, "1 - Advanced composites in aerospace engineering," in *Advanced Composite Materials for Aerospace Engineering*, S. Rana and R. Fangueiro, Eds., Woodhead Publishing, 2016, pp. 1–15. doi: 10.1016/B978-0-08-100037-3.00001-8.

[3] A. Elmarakbi, *Advanced Composite Materials for Automotive Applications: Structural Integrity and Crashworthiness*, 1st ed. in Automotive series. Chichester, West Sussex: John Wiley & Sons Ltd, 2013. doi: 10.1002/9781118535288.

[4] D. I. Chortis, "Structural Analysis of Composite Wind Turbine Blades," in *Structural Analysis of Composite Wind Turbine Blades: Nonlinear Mechanics and Finite Element Models with Material Damping*, D. I. Chortis, Ed., Heidelberg: Springer International Publishing, 2013, pp. 1–8. doi: 10.1007/978-3-319-00864-6_1.

[5] C. Ceccato, M. Salviato, C. Pellegrino, and G. Cusatis, "Simulation of concrete failure and fiber reinforced polymer fracture in confined columns with different cross sectional shape," *Int. J. Solids Struct.*, vol. 108, pp. 216–229, Mar. 2017, doi: 10.1016/j.ijsolstr.2016.12.017.

[6] S. G. Team, "Advanced Composites Advance U.S. Air Force Aviation," SAMPE Global. Accessed: Aug. 14, 2025. [Online]. Available: https://www.sampe.org/advanced-composites-advance-u-s-air-force-aviation/

[7] "Composite made commercial airplane: innovation and risks," 1001crash.com. Accessed: Aug. 10, 2025. [Online]. Available: https://www.1001crash.com/index-page-composite-lg-2.html

[8] A. A. Griffith and G. I. Taylor, "VI. The phenomena of rupture and flow in solids," *Philos. Trans. R. Soc. Lond. Ser. Contain. Pap. Math. Phys. Character*, vol. 221, no. 582–593, pp. 163–198, Jan. 1997, doi: 10.1098/rsta.1921.0006.

[9] A. Wells, "The Condition of Fast Fracture in Aluminum Alloys with Particular Reference to Comet," British Welding Research Association, 1955.

[10] M. E. Shank, "A CRITICAL SURVEY OF BRITTLE FRACTURE IN CARBON PLATE STEEL STRUCTURES, OTHER THAN SHIPS," Art. no. SSC-65, Dec. 1953, Accessed: Aug. 14, 2025. [Online]. Available: https://trid.trb.org/View/504

[11] M. Williams and G. ellinger, "Investigation of structural failures of welded ships," *Weld. Jounral*, vol. 32, pp. 498–528.

[12] M. D. Harris *et al.*, “Revisiting (Some of) the Lasting Impacts of the Liberty Ships via a Metallurgical Analysis of Rivets from the SS ‘John W. Brown,’” *JOM*, vol. 67, no. 12, pp. 2965–2975, Dec. 2015, doi: 10.1007/s11837-015-1668-1.

[13] T. L. Anderson and T. L. Anderson, *Fracture Mechanics: Fundamentals and Applications, Third Edition*, 3rd ed. Boca Raton: CRC Press, 2005. doi: 10.1201/9781420058215.

[14] H. Westergaard, “Bearing Pressures and Cracks: Bearing Pressures Through a Slightly Waved Surface or Through a Nearly Flat Part of a Cylinder, and Related Problems of Cracks,” *J. Appl. Mech.*, vol. 6, no. 2, Jun. 1939, doi: 10.1115/1.4008919.

[15] Z. P. Bazant and J. Planas, *Fracture and Size Effect in Concrete and Other Quasibrittle Materials*. New York: Routledge, 2019. doi: 10.1201/9780203756799.

[16] Z. P. Bazˇant, I. M. Daniel, and Z. Li, “Size Effect and Fracture Characteristics of Composite Laminates,” *J. Eng. Mater. Technol.*, vol. 118, no. 3, pp. 317–324, Jul. 1996, doi: 10.1115/1.2806812.

[17] Y. Qiao, A. A. Deleo, and M. Salviato, “A study on the multi-axial fatigue failure behavior of notched composite laminates,” *Compos. Part Appl. Sci. Manuf.*, vol. 127, p. 105640, Dec. 2019, doi: 10.1016/j.compositesa.2019.105640.

[18] M. Salviato, K. Kirane, Z. P. Bažant, and G. Cusatis, “Mode I and II Interlaminar Fracture in Laminated Composites: A Size Effect Study,” *J. Appl. Mech.*, vol. 86, no. 091008, Jun. 2019, doi: 10.1115/1.4043889.

[19] M. Salviato, K. Kirane, S. Esna Ashari, Z. P. Bažant, and G. Cusatis, “Experimental and numerical investigation of intra-laminar energy dissipation and size effect in two-dimensional textile composites,” *Compos. Sci. Technol.*, vol. 135, pp. 67–75, Oct. 2016, doi: 10.1016/j.compscitech.2016.08.021.

[20] S. Ko, J. Davey, S. Douglass, J. Yang, M. E. Tuttle, and M. Salviato, “Effect of the thickness on the fracturing behavior of discontinuous fiber composite structures,” *Compos. Part Appl. Sci. Manuf.*, vol. 125, p. 105520, Oct. 2019, doi: 10.1016/j.compositesa.2019.105520.

[21] S. Ko, J. Yang, M. E. Tuttle, and M. Salviato, “Effect of the platelet size on the fracturing behavior and size effect of discontinuous fiber composite structures,” *Compos. Struct.*, vol. 227, p. 111245, Nov. 2019, doi: 10.1016/j.compstruct.2019.111245.

[22] Y. Kumagai, S. Onodera, M. Salviato, and T. Okabe, “Multiscale analysis and experimental validation of crack initiation in quasi-isotropic laminates,” *Int. J. Solids Struct.*, vol. 193–194, pp. 172–191, Jun. 2020, doi: 10.1016/j.ijsolstr.2020.02.010.

[23] Z. P. Bažant, J.-L. Le, and and M. Salviato, *Quasibrittle Fracture Mechanics and Size Effect: A First Course*. Oxford, New York: Oxford University Press, 2022.

[24] J. Brockmann, “Experimental and Computational Exploration of the Fracture Energy in Fiber Composites When Subject to Crack Parallel Compression,” Jul. 2022, Accessed: Aug. 11, 2025. [Online]. Available: http://hdl.handle.net/1773/48797

[25] “Loading Modes I, II, III.” Accessed: Aug. 11, 2025. [Online]. Available: https://www.fracturemechanics.org/modes123.html

[26] J. R. Rice, “A Path Independent Integral and the Approximate Analysis of Strain Concentration by Notches and Cracks,” *J. Appl. Mech.*, vol. 35, no. 2, pp. 379–386, Jun. 1968, doi: 10.1115/1.3601206.

[27] J. Brockmann and M. Salviato, “The Gap test – Effects of crack parallel compression on fracture in carbon fiber composites,” *Compos. Part Appl. Sci. Manuf.*, vol. 164, p. 107252, Jan. 2023, doi: 10.1016/j.compositesa.2022.107252.

[28] H. T. Nguyen, M. Pathirage, G. Cusatis, and Z. P. Bažant, “Gap Test of Crack-Parallel Stress Effect on Quasibrittle Fracture and Its Consequences,” *J. Appl. Mech.*, vol. 87, no. 071012, May 2020, doi: 10.1115/1.4047215.

[29] “Standard Test Method for Measuring the Curved Beam Strength of a Fiber-Reinforced Polymer-Matrix Composite.” Accessed: Aug. 11, 2025. [Online]. Available: https://store.astm.org/d6415_d6415m-22.html

[30] V. B. Sitterle, W. Sun, and M. E. Levenston, “A modified lap test to more accurately estimate interfacial shear strength for bonded tissues,” *J. Biomech.*, vol. 41, no. 15, pp. 3260–3264, Nov. 2008, doi: 10.1016/j.jbiomech.2008.09.006.

[31] “ASTM D3039 | Instron.” Accessed: Aug. 14, 2025. [Online]. Available: https://www.instron.com/en/testing-solutions/astm-standards/astm-d3039/

[32] “Standard Test Method for Mode I Interlaminar Fracture Toughness of Unidirectional Fiber-Reinforced Polymer Matrix Composites.” Accessed: Aug. 14, 2025. [Online]. Available: https://store.astm.org/d5528_d5528m-21.html

[33] S. B. Clay and P. M. Knoth, “Experimental results of quasi-static testing for calibration and validation of composite progressive damage analysis methods,” *J. Compos. Mater.*, vol. 51, no. 10, pp. 1333–1353, May 2017, doi: 10.1177/0021998316658539.

[34] “Composite Materials Handbook Volume 3 - Revision G.” Accessed: Aug. 13, 2025. [Online]. Available: https://www.sae.org/publications/books/content/r-424/

[35] Z. S. AG, “G3 digital cutter | Flatbed CNC Cutter | Zünd,” Zünd Systemtechnik AG. Accessed: Aug. 13, 2025. [Online]. Available: https://www.zund.com/en/cutting-systems/digital-cutting-systems/g3-cutter

[36] “University of Washington, Advanced Composites Center,” Advanced Composites Center. Accessed: Aug. 13, 2025. [Online]. Available: https://www.uwacc.uw.edu/

[37] J. Chen, “Comprehensive Investigation of Quasibrittle Fracture of IM7/977-3 Laminates via Size Effect Analysis,” Aug. 2023, Accessed: Aug. 11, 2025. [Online]. Available: http://hdl.handle.net/1773/50202

[38] R. Geerts, “Vacuum Bagging Basics,” Epoxyworks. Accessed: Aug. 13, 2025. [Online]. Available: https://www.epoxyworks.com/vacuum-bagging-basics/

[39] *Vacuum Bagging Basics*. 2019. [Online]. Available: https://www.epoxyworks.com/index.php/vacuum-bagging-basics/

[40] “CYCOM® 977-3,” Syensqo. Accessed: Aug. 13, 2025. [Online]. Available: https://www.syensqo.com/en/product/cycom-977-3

[41] “CYCOM® 977-3 Epoxy Resin System Technical Datasheet.” Accessed: Aug. 13, 2025. [Online]. Available: https://www.e-aircraftsupply.com/MSDS/10520CYCOM%20977-3%20tds.pdf?srsltid=AfmBOooJjpZ4pk-Lopm7kVRS6-qe6vZ6YGp0pCS1A4tXB2e69AaEdgpH

[42] M. Xu and K. Wille, “Fracture energy of UHP-FRC under direct tensile loading applied at low strain rates,” *Compos. Part B Eng.*, vol. 80, pp. 116–125, Oct. 2015, doi: 10.1016/j.compositesb.2015.05.031.